

See discussions, stats, and author profiles for this publication at:
<https://www.researchgate.net/publication/237201787>

Nonlinear electron dynamics in metal clusters

ARTICLE *in* PHYSICS REPORTS · OCTOBER 2000

Impact Factor: 20.03 · DOI: 10.1016/S0370-1573(00)00043-0

CITATIONS

316

READS

41

4 AUTHORS, INCLUDING:



Florent Calvayrac

Université du Maine

63 PUBLICATIONS 935 CITATIONS

SEE PROFILE



Eric Suraud

Paul Sabatier University - Toulous...

267 PUBLICATIONS 3,680 CITATIONS

SEE PROFILE

NONLINEAR ELECTRON DYNAMICS IN METAL CLUSTERS

F. CALVAYRAC^a, P.-G. REINHARD^b, E. SURAUD^a, C.A. ULLRICH^c

*^aLaboratoire de Physique Quantique, Université Paul Sabatier, 118 route de Narbonne,
F-31062 Toulouse Cedex, France*

^bInstitut für Theoretische Physik, Universität Erlangen, Staudtstr. 7, D-91058 Erlangen, Germany

^cInstitute for Theoretical Physics, University of California, Santa Barbara, CA 93106-4030, USA



ELSEVIER

AMSTERDAM – LAUSANNE – NEW YORK – OXFORD – SHANNON – TOKYO



ELSEVIER

Physics Reports 337 (2000) 493–578

PHYSICS REPORTS

www.elsevier.com/locate/physrep

Nonlinear electron dynamics in metal clusters

F. Calvayrac^{a,1}, P.-G. Reinhard^b, E. Suraud^{a,*}, C.A. Ullrich^c

^a*Laboratoire de Physique Quantique, Université Paul Sabatier, 118 route de Narbonne, F-31062 Toulouse Cedex, France*

^b*Institut für Theoretische Physik, Universität Erlangen, Staudtstr. 7, D-91058 Erlangen, Germany*

^c*Institute for Theoretical Physics, University of California, Santa Barbara, CA 93106-4030, USA*

Received December 1999; editor: J. Eichler

Contents

1. Introduction	496	4.2. Observables	527
1.1. Electron dynamics in metal clusters	497	5. Spectral properties in the linear regime	530
1.2. Basic mechanisms and associated time scales	497	5.1. Typical spectra	530
2. Mean field models far from equilibrium	500	5.2. Trends	536
2.1. Survey of theoretical methods	500	6. Energetic ion collisions	541
2.2. Basic features of time-dependent density functional theory	503	6.1. The excitation process as such	541
2.3. Time-dependent local density approximation and beyond	505	6.2. Basic properties of collisional excitation	542
2.4. Description of the positive ionic background	508	6.3. Trends with collision parameters	544
2.5. The actual procedure	511	6.4. Effects of electronic two-body collisions	549
2.6. Semiclassical approximations	512	7. Irradiation with intense laser beams	551
3. Numerical aspects	515	7.1. Basic mechanisms: a detailed case study	551
3.1. Choice of the numerical representation	516	7.2. Trends with laser parameters	554
3.2. Solving TDLDA on a grid	516	7.3. Self-interaction effects	560
3.3. Handling of the ionic background	521	7.4. Kinetic energy spectra of emitted electrons	561
3.4. Vlasov and VUU simulations	522	7.5. VUU	563
4. Relation to measurements	523	7.6. The search for anharmonic effects	565
4.1. Excitation mechanisms in the nonlinear regime	523	7.7. Coupling to ionic motion	567
		8. Conclusions and perspectives	571
		Acknowledgements	573
		References	574

¹ Present address: LPEC, Université du Maine, F-72085 Le Mans.

* Corresponding author. Tel: + 33-5-61-55-60-67; fax: + 33-5-61-55-60-65.

E-mail address: suraud@irsamc2.ups-tlse.fr (E. Suraud).

Abstract

Recent experimental developments give more and more access to cluster excitations beyond the regime of linear response. Most theoretical descriptions of the induced nonlinear electron dynamics are based on the time-dependent local density approximation (TDLDA) and related schemes. We review the present status of TDLDA calculations for metal clusters, considering formal aspects of the theory, recipes for its numerical implementation as well as a variety of applications. These applications are presented by first summarizing basic linear spectral properties of the systems under study and then introducing two mechanisms for strong excitations: collision with highly charged and fast ions, and irradiation with strong femtosecond laser pulses. We present results for observables that are relevant for experiments, including ionization, energy balance, second-harmonic generation, electron emission spectra and, last but not least, we discuss the effects of ionic motion during the electronic dynamics. On the theoretical side, we also discuss semiclassical approaches and extensions beyond TDLDA, such as self-interaction corrections and the influence of electron–electron collisions. © 2000 Elsevier Science B.V. All rights reserved.

PACS: 36.40. – c

1. Introduction

Clusters fall in between many categories of historically established areas of research. Cluster physics unifies concepts and techniques from atomic and molecular physics as well as from solid-state physics. Naturally, there is also a strong link to chemistry, experimentally as well as theoretically. Cluster physics thus constitutes sort of a melting pot of all these various branches of science, and the interplay between them is what makes this field so interesting. Looking back over somewhat more than two decades, cluster physics has now become a mature field of research with its own standing and a rich variety of subfields. There is, for example, the research on carbon clusters which constitutes a widely pursued subject of its own. Clusters also serve as interesting probes in surface chemistry, in particular as potential catalysts. Very recently, nanostructures made from arrays of clusters have also drawn much attention. One can hardly summarize in a few words all the current fundamental aspects and applications of cluster physics, and we shall thus close this superficial (and surely incomplete) list of examples.

Among the various types of clusters (usually classified according to the nature of the elementary bonding: covalent, van der Waals, ionic, metallic, etc.), metal clusters constitute a category that has received considerable attention. A variety of impressive and detailed experimental results have been obtained over the years. At the same time, sizable efforts have been made to develop a proper theoretical description of these objects. In metal clusters, as in bulk metal, valence electrons are, to a large extent, delocalized. Beyond this common feature, metal clusters offer a wide variety of choices. One may encounter various degrees of complexity for different materials, depending on the nature of the valence electrons. Alkaline elements (Na, K, Cs, etc.) provide here the simplest textbook-like situation in which a single-valence *s*-electron per atom is fully delocalized over the whole system. In turn, noble metals are examples for a situation in which the semi-localized *d*-electrons play a key role, which considerably increases the complexity of the description.

Simple metal clusters made out of alkaline atoms thus serve as a prototype for generic studies. These simple cases are indeed important in many respects – they obviously constitute the first and simplest step towards more complex materials, and for this reason they need to be understood in depth. Furthermore, they allow one to focus the efforts of the investigations on physical, rather than technical, key issues because the relevant electronic degrees of freedom are well defined (delocalized *s*-electrons) and easily described. A typical example for the successful interplay of the theory of simple metal clusters and experimental findings is the role of cluster size, in terms of geometry as well as in terms of quantum effects. It is thus fair to say that simple metal clusters allow for “clean” studies of the dynamics of finite fermion systems. We also mention in this context the kinship between simple metal clusters and atomic nuclei, a link which has been pointed out since long, and which has been thoroughly investigated.

In the following, we shall thus focus on simple metal clusters, and more specifically on their dynamical properties. We shall pay peculiar attention to situations far beyond the simple adiabatic excitations, which belong to the realm of linear response theory. This actually implies a requirement for new theoretical methods as well as experimental techniques to explore these regions of nonlinear excitations in simple metal clusters. As is obvious because of the huge mass difference between ions and electrons, the response of the cluster will in the first place show up at the level of electronic degrees of freedom. We shall thus largely focus on electron dynamics in the following,

although, as we shall see, it turns out that in strongly out of equilibrium situations, ionic degrees of freedom may very soon play an important role.

1.1. *Electron dynamics in metal clusters*

The electronic dynamics in metal clusters has been in the focus of investigations since the early days of this field [1,2]. A key role was played by optical response properties, which helped to elucidate the underlying cluster structures. Most of the accompanying theoretical analysis was done using linearized time-dependent local density approximation (Linearized TDLDA), which was brought into the field by [3,4] and has been intensely used since then. An enormous amount of information has thus been gathered during that phase of cluster research and is summarized in several books and review articles [5–11]. Steady progress of experimental techniques has meanwhile given access to the domain of truly nonlinear excitations. Examples are provided by the beams of highly charged ions which are designed to ionize the metal cluster into high charge states [12]. And there are, of course, the nowadays very fashionable femtosecond (fs) lasers, which can be used either as high-intensity light sources [13] or as subtle and precise instruments in pump–probe experiments [14,15]. The theoretical description of these processes is still developing, alongside of experimental progress. But a large body of material has already accumulated, and an up-to-date summary of theoretical methods and calculations in the regime of highly excited metal clusters seems timely. It is the aim of this article to provide such an overview.

The preferred theoretical tool in the nonlinear regime is still the TDLDA, but now in its full extent without linear restrictions. Full TDLDA calculations for metal clusters have been initiated in [16–18] and often been used since then. On the one hand, they provide a conceptually simple means to compute optical response in fully three-dimensional problems [17]. And they are, on the other hand, the most practicable tool to explore the nonlinear regime, as done, e.g., in [16,18,19]. Most of the results reviewed here will thus be concerned with TDLDA. Simplifications may be achieved using semiclassical approximations such as the Vlasov-TDLDA [20–22], which becomes valid for high excitations and/or large systems. In addition, the Vlasov approach opens a route towards a manageable method for including dynamical electronic correlation effects beyond TDLDA, by means of the Vlasov–Ühling–Uhlenbeck (VUU) scheme [23]. Therefore, in addition to a detailed presentation of the TDLDA formalism, we will also give a brief account of the Vlasov and VUU methods and results.

1.2. *Basic mechanisms and associated time scales*

After this general introduction, we now give an overview of the typical processes and associated time scales in Na clusters, as sketched in Fig. 1. Three excitation mechanisms are indicated: nanosecond (ns) lasers, fs lasers, and collisions with a fast highly charged projectile. They differ dramatically in their duration, from ns down to sub-fs. But all three excitations have in common that they couple to the cluster via the Coulomb interaction, so that the entrance channel can be viewed in each case as a mere dipole excitation caused by an external time-dependent electric field. From then on, the energy spreads successively over the various degrees of freedom within the cluster. We first discuss the time scales associated with a very fast excitation, which serves to set a sharply defined clock. The initial Coulomb pulse (of a passing ion) first induces a dipole excitation

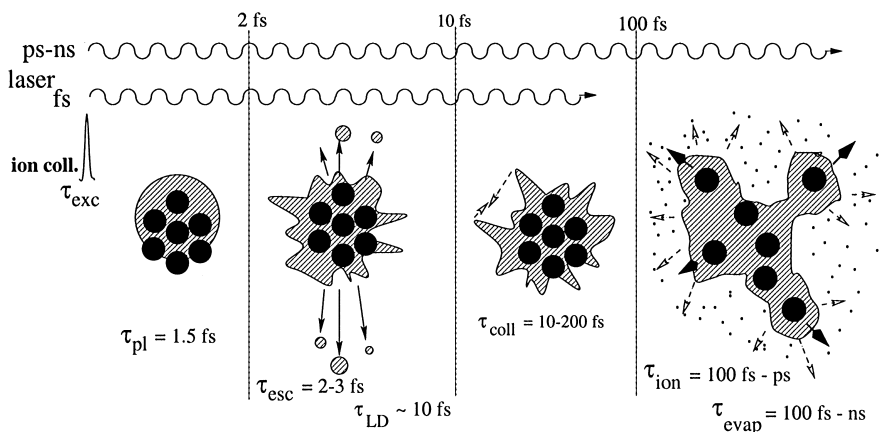


Fig. 1. Schematic view of dynamical mechanisms involved in the processes described in this review: collisions with rapid highly charged ions and irradiation with intense femtosecond laser pulses. The various associated times scales are indicated with typical values (see text for details). The picture is split into four panels corresponding to various stages of the cluster's response: the first panel corresponds to immediate (electronic) response; the second one, still in the electronic domain, describes the electronic relaxation following the excitation phase; the third panel describes the long time electronic relaxation and the gradual coupling to ionic degrees of freedom, while the fourth panel shows the coulomb explosion due to high ionization.

which causes the center of mass of the valence electron cloud to oscillate about the still fixed ionic background. This is indicated in the leftmost graph of Fig. 1. The oscillations are dominated by the Mie surface plasmon whose period for Na clusters is about 1.5 fs [24,8]. Very soon, however, the (initially collective) charge-density oscillations get perturbed by direct electron emission and by fragmentation of the plasmon into nearby one-particle–one-hole (1ph) states, as schematized in the second snapshot of Fig. 1. The latter process is analogous to Landau damping, i.e. the attenuation of the plasmon in an electron gas [25,26], but a more appropriate terminology for this effect in finite systems is Landau fragmentation. Direct electron emission may, in fact, also be viewed as part of the Landau fragmentation: it is caused by coupling to that part of the spectrum which belongs to the continuum. Direct electron emission also provides the fastest damping mechanism of the dipole oscillations, with the electrons being kicked out within the first 2–5 fs. The time scale for Landau fragmentation, on the other hand, depends sensitively on the actual level density of the considered cluster and thus on the particular system. It is rather long in small clusters where the distribution of 1ph states near the plasmon frequency is very dilute, it has a maximum at around $N = 1000$ atoms, and it shrinks again $\propto N^{-1/3}$ for even larger N , because the coupling between plasmon and 1ph states decreases, for a detailed discussion see Section 5.2.2. A typical relaxation time due to Landau fragmentation is 10 fs, roughly valid for N in the range 50–1000. Direct electron emission and Landau fragmentation both serve to bring the oscillations of the various single-electron states out of phase, thus inducing temporal and spatial fluctuations of the mean field, as shown in the second graph of Fig. 1.

The electrons now move occasionally in opposite directions, which gives rise to electron–electron collisions, as sketched in the third snapshot of Fig. 1. These collisions provide a further damping mechanism which eventually drives the electron cloud towards thermal equilibrium. The

relaxation time for this collisional damping depends sensitively on the internal excitation energy (measured by the temperature T) of the system. It was recently estimated in a semiclassical approximation (VUU, as explained and applied in Sections 2.6.2, 6.4, 7.5) in metal clusters described with a jellium ionic background and it was shown to follow the trend [23]

$$\tau_{\text{coll}} = 2.5 \text{ fs eV}^2/T^2 = 3.3 \text{ fs eV}/E^*/N, \quad (1)$$

given equivalently in terms of temperature T or internal excitation energy per particle E^*/N . These numbers are in accordance with estimates for bulk matter [26]. Collisional damping plays a minor role in the regime of weak perturbations, but its importance grows rapidly with the violence of the excitation process. This relaxation time can thus take on almost any value, depending on the situation. But note that within our scenario collisions become effective only after the initially collective motion has been sufficiently distorted through the accumulated influence of Landau fragmentation and direct electron emission. In order to make the discussion more quantitative, let us give a few typical collisional relaxation times: the small Na_9^+ cluster with about one plasmon excitation energy ($E^* \sim 3 \text{ eV}$) has $\tau_{\text{coll}} \approx 10 \text{ fs}$, whereas the larger Na_{93}^+ under the same conditions has $\tau_{\text{coll}} \approx 100 \text{ fs}$, and times shrink with increasing excitation energies.

The electron dynamics dominates the first phases of the response of the cluster, but does not entirely exhaust it. Indeed, somewhat later than the various above discussed electronic times, the ions will come into play. In fact, they very soon feel after the initial excitation that the electron cloud is different from its initial state and they react accordingly. However, the large ionic mass leaves a longer time span until effects of the ionic response can be felt. We have found in several simulations that it is typically after around 100 fs that first effects from ionic motion can be felt (see Section 7.7). The whole ionic evolution, of course, extends over longer periods and eventually leads to monomer emission, or fragmentation in the more violent scenarios. This is the situation sketched in the rightmost snapshot of Fig. 1.

There is still one more process going on over long time scales, namely thermal electron evaporation, as hinted by the faint arrows and dust in the rightmost part of Fig. 1. Its time scale can be estimated with the Weisskopf rule as [27]

$$\tau_{\text{evap}} = (2\sigma_{\text{cap}}/\hbar^3\pi^2)mT^2 \exp(-E_{\text{B}}/T), \quad \sigma_{\text{cap}} \sim \pi R^2, \quad (2)$$

where E_{B} denotes the electronic binding energy. The evaporation time very strongly depends on temperature. Usually, it is the latest process in the sequence, but it can easily reach down into the 10 fs range for very high temperatures around 0.5–1 eV.

The same estimate (2) applies also to monomer emission if monomer mass and removal energy are properly inserted. One has to keep in mind, however, that this rule for monomers can only be applied if the ionic system is sufficiently thermalized, which in itself takes several ionic vibrational cycles, i.e. more than about 500 fs.

The artist's view of Fig. 1 is complemented by a more quantitative summary in Fig. 2 where we show the time scales discussed above as a function of temperature. Those processes that depend weakly on T are represented by straight horizontal lines. Note how dramatically the temperature-dependent times (collisional relaxation and evaporation) change with the internal excitation of the system. This emphasizes the importance of gaining control over the amount of thermal energy deposited in the cluster by choosing the excitation mechanism in a suitable way. It is also interesting to note the versatility of the typical excitation mechanisms (fast ions, fs lasers) that we

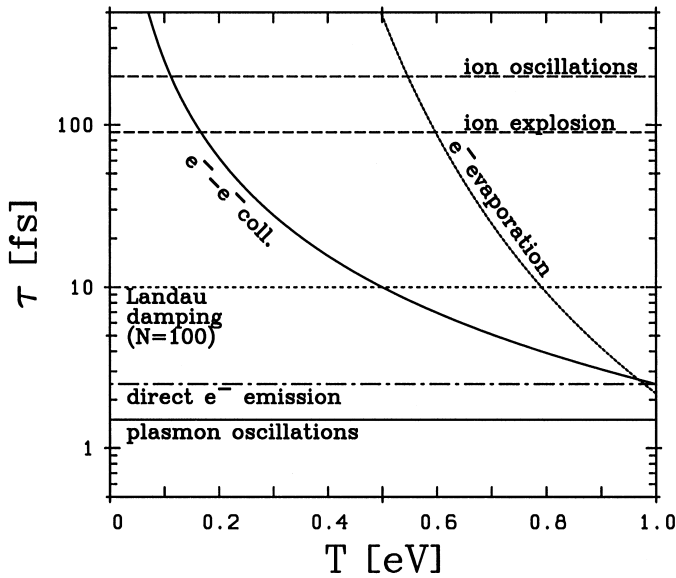


Fig. 2. Illustration of the various time scales in sodium cluster dynamics. Times have been drawn as a function of the temperature T to accommodate the two processes which depend strongly on temperature. The processes depending little on temperature are shown as constant lines.

aim at discussing here. Depending on the parameters of the probe (velocity of the projectile ion, duration of the laser pulse) they can be varied between about 1 fs (and below) and a few hundreds of fs. The time scales of excitation can hence overlap with most of the discussed electronic (and even sometimes ionic) time scales, which shows both the complexity and the richness of the phenomena reviewed here.

2. Mean field models far from equilibrium

2.1. Survey of theoretical methods

The task of describing clusters theoretically can be grossly divided into two steps. First, one needs to determine the electronic and ionic structure of the ground state, and second, one wants to explore the dynamical features of the system under the influence of an external perturbation. We will now discuss briefly the hierarchy of approximations which is nowadays used in both of these steps. In fact, most of the tools described below are common to molecular and solid-state physics. This is no surprise because clusters are just in between these two extremes. Nonetheless, we will concentrate the survey on the cluster applications with only occasional (and thus certainly incomplete) references to other fields.

2.1.1. Theories for the ground state

The hierarchy of approximations for ground-state structure calculations is nowadays well understood. The full N -body Schrödinger equation can only be solved for very small systems [28]

or the homogeneous electron gas [29]. The highly developed quantum chemical methods basically rely on the Hartree–Fock approximation, refined at various degrees of complexity through configuration interactions (CI). These methods have been extensively used for computing the structure of small clusters up to about 10 ions, for a review see [7]. Larger systems require more efficient approaches, and here density-functional theory (DFT) is now established as the most widely used and efficient tool for self-consistent calculations of electronic structure [30,31]. By far most applications have been done at the level of the local-density approximation (LDA). To describe an arbitrary inhomogeneous system, the LDA uses as input exact results for the homogeneous electron gas, such as from [29], evaluated at local densities $n(\mathbf{r})$. Thus, most of the results to be discussed (and cited) later on will also rely on LDA (see Sections 2.2 and 2.3.1 for practical aspects). The LDA is the simplest approach within DFT and it has, of course, some deficiencies. But there are several attempts to improve on LDA. For instance, one can take a better account of inhomogeneities by using gradient corrected functionals [32–34]. One can also correct the self-interaction error [35], see Section 2.3.2 and references therein. On the other hand, further simplification of the LDA is achieved in shell-model approaches which start directly with an educated guess of the effective Kohn–Sham mean field. These latter descriptions have been employed for first investigations of the shell structure of metal clusters [36,5,6] and are still useful, for example for explorations of huge clusters [37–39]. A different path of reduction is followed in the class of tight-binding (or Hückel) approaches [40] where electronic structure is eliminated in favor of an effective atom–atom interaction.

The handling of ionic structure adds further facets to the above hierarchy of electronic models. The most elaborate approach is a fully quantum mechanical handling of ions and electrons [41] which, however, can only be used in very small systems, as, e.g. the H_2 molecule. The standard approach is thus to treat the ions as classical particles. Moreover, one restricts the active electrons to the few valence electrons of the atom, treating the deeper bound electrons together with the nucleus as one inert ionic core. To that end, one employs pseudopotentials for a proper description of the interaction between the ionic core and the remaining active electrons [42,43]. This is the standard approach in many DFT calculations with detailed ionic structure, see for example [44–46] for such early structure calculations of metal clusters. The associated fully three-dimensional electronic calculations are very demanding and quickly reach the limits of manageable system sizes. Therefore, approximations with full ionic structure but enforced electronic symmetries have been developed in several groups. The spherically averaged pseudopotential scheme (SAPS), for example, gives an easy access even to very large clusters, provided the underlying geometry is close to sphericity [47,48]. A wider class of clusters is covered with the cylindrically averaged pseudopotential scheme (CAPS) where axial symmetry is imposed on the electrons. This scheme can be applied to all cluster with approximately axially symmetric structure [49–51].

One can even simplify the problem one step further if one is predominantly interested in the impact of electronic shell effects. This leads to the jellium model for the ionic background, which was first employed for metal clusters in [3,4] and has been used heavily since then, for reviews see e.g. [5,6]. In the simple jellium approach the total energy is far off realistic binding values because one is missing the structure energy, i.e. the contribution from ionic structure plus local electronic polarization. This deficiency is successfully cured in the stabilized jellium [52] or in the structure-averaged jellium approach [49]. The final step down the ladder are the shell or liquid drop model

approaches [53], as mentioned above, where the ionic background enters only very indirectly by stabilizing the overall extension of the system.

An opposite line of development with a stronger bias toward ionic structure is followed in the tight-binding-like approaches mentioned above. Jellium-like approaches are more natural for metal clusters where the valence electrons possess a long mean free path. The tight-binding-like approaches have their stronghold in systems with preferably localized electrons and van der Waals binding. But the borderlines are diffuse and one can show that many of the different approaches produce very similar results in common regimes of validity [54].

The optimization of ionic structure is most time-consuming part in determining the ground state. The Car–Parinello technique uses ionic pseudodynamics to cool down the system to its ground state [55]. This has been used in cluster physics, e.g., in [44,45]. Alternatively, one can use simulated annealing with Monte-Carlo techniques, as outlined below, see Sections 2.5. Monte-Carlo approaches have been used e.g., in [51,56–58]. Both these techniques (Car–Parinello and Monte-Carlo) are very expensive to use. Thus, one often uses for very large systems just a fragment of the bulk crystal [17,59]. Detailed optimization of ionic structure is also a goal in the tight-binding approaches and here it is usually done with Monte-Carlo techniques [40]. The jellium model also requires an optimization of the jellium shape. But this is much simpler than any approach involving explicit ionic positions since one has to optimize only with respect to a few deformation parameters, and that is usually done by explicit minimization in the multi-dimensional landscape of these deformation parameters. An example for an extensive search is given in [60], where the structure-averaged jellium is employed in order to have a meaningful total energy in the search.

2.1.2. *Handling of the dynamical evolution*

The computation of a proper ground-state structure is only the preparatory work in the dynamical studies we aim at. There is a similar, even richer, hierarchy of approaches for treating the dynamics of clusters. In fact, the main features of this hierarchy can simply be copied over from the static case and need only a few additions where new aspects arise from the dynamical treatment. Again, we find at the highest level a few calculations involving the full time-dependent Schrödinger equation for very small systems, e.g. [61]. There also exist quantum-chemical *ab initio* calculations of (small) excitations in small clusters [7]. But the bulk of the investigations relies on time-dependent density-functional theory (TDDFT), which is a nontrivial extension of stationary DFT [62–65]. And again it is a local approximation which is the most commonly used tool: the time-dependent local-density approximation (TDLDA), which now is local in space as well as local in time (i.e. instantaneous). By far most dynamical studies are performed at the level of TDLDA. But we ought to mention here a subtle distinction between the various versions of TDLDA found in the literature. Early applications aimed at small-amplitude excitations and simplified expense by employing a linearized version of TDLDA (sometimes, not quite correctly, called RPA) [3,4,6]. Nowadays one is interested in violent dynamics and/or detailed ionic structure effects for which one applies the full TDLDA in real time, either on a grid, see e.g. [16–18], or projected on a basis of atomic orbitals [66]. A detailed outline of full TDLDA on a grid is given in the subsequent sections.

The TDLDA is often called adiabatic TDLDA or simply ALDA, to emphasize that correlations are assumed to form at a much faster time scale than the processes actually studied, which permits the assumption that correlations are instantaneous. But that notion should not be mixed with an

adiabatic (Born–Oppenheimer) approach of the ionic plus electronic dynamics. The remaining defects of TDLDA can again be cured in many ways. Gradient corrections and self-energy effects can be dealt with in analogy with the static regime. But in addition to this, there are more genuinely dynamical corrections. This is still an area of active research. A first attempt has been to include a dependence on local currents [67].

Concerning the ions, one recurs to the same pseudopotential approaches as already used in the static case (implying the approximation of dynamically inert cores). The ionic dynamics as such is the easiest part in the whole setup. Short time dynamics (up to about 100 fs) can deal with ions frozen at their ground-state positions. Longer time spans should involve the simultaneous propagation of ions as classical particles, see e.g. [68,66] and Section 2.4.2. It is to be noted that the simultaneous propagation of ionic dynamics, although technically simple, is very time consuming due to the large time spans needed to accumulate sufficient ionic amplitudes. Thus, one often recurs to an adiabatic molecular dynamics along the Born–Oppenheimer surface where electrons are stepping from ground state to ground state while the ions are propagating at their slower pace. This has been done in connection with full LDA e.g. in [69] and at the level of Thomas–Fermi-LDA in [70]. The advantage is that one can use much larger time steps because only the ionic time scale needs to be respected. But such models apply only to situations in which the electron cloud stays close to a Born–Oppenheimer surface. Violent excitations leave that regime quickly and one is forced to use the full-blown ionic plus electronic dynamics.

Nearly all early studies of electronic excitations (within linearized TDLDA) and still many recent exploratory studies of electron dynamics are done with the simple jellium model for the ionic background. This gives a bias on electronic shell effects in the dynamical response which is very often a valid perspective in the realm of metal clusters. The jellium background is usually kept frozen in its ground-state shape because there is not yet a well-tested model for jellium dynamics available. It is to be noted, though, that meanwhile there exist first attempts towards using a jellium with its own dynamics [71].

It should also be noted that in some cases of violent electron dynamics one is allowed to neglect quantum effects and to treat the TDLDA in semiclassical approximations. The full phase space dynamics is still carried forth in the Vlasov-LDA [20,21,72]. This approach also permits a manageable treatment of dynamical electron–electron correlations by adding an Ühling–Uhlenbeck collision term [23]. A simpler approach for many purposes is the dynamical variant of the Thomas–Fermi approximation [73]. For details on these various semiclassical approaches see Section 2.6.

Finally, there are also several dynamical calculations based on the shell model potential, see e.g. [74,75]. These are, however, all restricted to the linear regime of small excitations because one cannot trust the predictive power of the (static) shell model when extrapolating to large amplitude dynamics.

2.2. Basic features of time-dependent density functional theory

A complete description of the dynamics of an interacting N -electron system in a time-dependent external scalar potential requires solution of the N -body Schrödinger equation

$$i(\partial/\partial t)\Psi(x_1, \dots, x_N, t) = \hat{H}(t)\Psi(x_1, \dots, x_N, t), \quad (3)$$

where the coordinates $x_i \equiv (\mathbf{r}_i, \sigma_i)$ denote the spatial and spin degrees of freedom of the electrons. The Hamiltonian is given (in atomic units) by

$$\hat{H}(t) = \sum_{i=1}^N \left(-\frac{\nabla_i^2}{2} + v_0(\mathbf{r}_i, t) \right) + \frac{1}{2} \sum_{\substack{i,j=1 \\ i \neq j}}^N \frac{1}{|\mathbf{r}_i - \mathbf{r}_j|} . \quad (4)$$

In general, the potential $v_0(\mathbf{r}, t)$ is the sum of the Coulomb potential $v_{\text{ion}}(\mathbf{r}, t)$ of the atomic nuclei (whose positions can vary with time) plus the scalar potential $v_{\text{ext}}(\mathbf{r}, t)$ associated with an external source, such as a laser pulse or a charged projectile passing by. As an aside, we mention that a complete and general description of time-dependent processes involves scalar as well as vector potentials. For the systems considered in the following, however, it is always possible to either ignore the presence of vector potentials or to transform them into corresponding scalar potentials, as done for instance in the dipole approximation for the laser field (see Section 4.1.3 below).

In many cases of practical interest, $v_0(\mathbf{r}, t)$ is static for $t < t_0$, and its explicitly time-dependent part is switched on at t_0 . One then takes the system to be in a fixed stationary state Ψ_0 (usually the ground state) for $t < t_0$, and seeks to determine its time evolution for $t > t_0$ via solution of Eq. (3) with the initial condition $\Psi(t_0) = \Psi_0$.

In practice, a numerical solution of the full time-dependent N -body Schrödinger equation (3) is of course hopelessly complicated. It has so far only been accomplished for systems with at most two electrons [61]. Since we are interested in the dynamics of metal clusters with valence electron numbers N ranging from below 10 up to around a 100, there is an obvious need for a more economic approach.

In time-dependent density functional theory (TDDFT), the time-dependent electron density,

$$n(\mathbf{r}, t) = N \sum_{\sigma=\uparrow\downarrow} \int d\mathbf{x}_2 \dots \int d\mathbf{x}_N |\Psi(\mathbf{x}, \mathbf{x}_2, \dots, \mathbf{x}_N, t)|^2 , \quad (5)$$

replaces the N -body wavefunction $\Psi(x_1, \dots, x_N, t)$ as basic variable. Clearly, this concept means an enormous simplification, since it allows one to describe the system in terms of a four dimensional, rather than a $(3N + 1)$ -dimensional quantity.

The formal framework of TDDFT was established by Runge and Gross in 1984 [62]. The key concept can be summarized in the following statement, which can be viewed as the time-dependent version of the famous Hohenberg–Kohn theorem of stationary DFT [76,77]: *Given a fixed initial state Ψ_0 , every observable quantity can be calculated, at least in principle, from the time-dependent density alone, i.e. each quantum mechanical observable can be written as a functional of $n(\mathbf{r}, t)$.* Several review articles on TDDFT are available [63–65] which contain the proof of the above statement as well as a more detailed account of the formalism and its implications.

The density of the interacting system of interest can be obtained as the density of an auxiliary system of non-interacting particles moving in an effective *local* single-particle potential, the so-called Kohn–Sham potential. In the following, it is convenient to formulate the theory in terms of the spin densities $n_\sigma(\mathbf{r}, t)$, given by

$$n(\mathbf{r}, t) = \sum_{\sigma=\uparrow\downarrow} n_\sigma(\mathbf{r}, t) = \sum_{\sigma=\uparrow\downarrow} \sum_{j=1}^{N_\sigma} |\varphi_{j\sigma}(\mathbf{r}, t)|^2 , \quad (6)$$

where the particle number is $N = \sum_{\sigma} N_{\sigma}$ and the single-particle orbitals $\varphi_{j\sigma}(\mathbf{r}, t)$, labeled with the quantum numbers of their respective initial state, satisfy the time-dependent Kohn–Sham equation (in atomic units)

$$i(\partial/\partial t)\varphi_{j\sigma}(\mathbf{r}, t) = (-\nabla^2/2 + v_{\sigma}[n_{\uparrow}, n_{\downarrow}](\mathbf{r}, t))\varphi_{j\sigma}(\mathbf{r}, t) . \quad (7)$$

The Kohn–Sham effective potential v_{σ} is usually decomposed into the external potential $v_0(\mathbf{r}, t) = v_{\text{ion}}(\mathbf{r}, t) + v_{\text{ext}}(\mathbf{r}, t)$, a time-dependent Hartree part and the exchange-correlation (xc) potential:

$$v_{\sigma}[n_{\uparrow}, n_{\downarrow}](\mathbf{r}, t) = v_0(\mathbf{r}, t) + v_{\text{H}}[n](\mathbf{r}, t) + v_{\text{xc}\sigma}[n_{\uparrow}, n_{\downarrow}](\mathbf{r}, t) , \quad (8)$$

where v_{H} is the Hartree potential, defined as

$$v_{\text{H}}[n](\mathbf{r}, t) = \int d^3r' \frac{n(\mathbf{r}', t)}{|\mathbf{r} - \mathbf{r}'|} . \quad (9)$$

The xc potential $v_{\text{xc}\sigma}[n_{\uparrow}, n_{\downarrow}](\mathbf{r}, t)$ is a functional of the time-dependent spin densities $(n_{\uparrow}(\mathbf{r}, t), n_{\downarrow}(\mathbf{r}, t))$. Its crucial feature is that it is local in space and in time (i.e., it is a multiplicative operator), which leads to an enormous computational simplification as compared to other approaches featuring nonlocal potentials (such as time-dependent Hartree–Fock, which not even includes correlation). On the other hand, $v_{\text{xc}\sigma}$ itself is of course a tremendously complicated object, since it has to contain all dynamical many-body correlations and memory effects of the system. The essence of TDDFT is thus to find good approximations for the xc potential that are accurate, yet simple enough, to be employed in practice. In searching for those expressions, one follows a slightly different philosophy than in static DFT, where the standard procedure is to first construct an approximate xc *energy* functional E_{xc} and then obtain the associated v_{xc} via functional derivative. In the time-dependent case, the approximations are done on the level of the xc potential itself, since the physical meaning of the time-dependent xc energy (or, rather, the xc *action* [63]) is less clearly defined than for its static counterpart.

2.3. Time-dependent local density approximation and beyond

2.3.1. The local-density approximation

The exchange-correlation potential $v_{\text{xc}\sigma}$ in TDDFT is generally much more involved than its static cousin and there is currently an intense search for manageable forms. For the time being, the simplest choice for the xc potential consists in the time-dependent local density approximation (TDLDA), also known as adiabatic LDA, which assumes that the time-dependent xc potential has the functional form of the *static* LDA, only with a time-dependent density:

$$v_{\text{xc}\sigma}^{\text{TDLDA}}[n_{\uparrow}, n_{\downarrow}](\mathbf{r}, t) = \text{de}_{\text{xc}}^{\text{hom}}[\bar{n}_{\uparrow}, \bar{n}_{\downarrow}]/\text{d}\bar{n}_{\sigma}|_{\bar{n}_{\sigma}=n_{\sigma}(\mathbf{r}, t)} , \quad (10)$$

where $\text{e}_{\text{xc}}^{\text{hom}}(\bar{n}_{\uparrow}, \bar{n}_{\downarrow})$ is the xc energy density of a homogeneous electron gas of spin densities $(\bar{n}_{\uparrow}, \bar{n}_{\downarrow})$, so that the static LDA xc energy is given by

$$E_{\text{xc}}^{\text{LDA}}[n_{\uparrow}, n_{\downarrow}] = \int d^3r \text{e}_{\text{xc}}^{\text{hom}}(n_{\uparrow}(\mathbf{r}), n_{\downarrow}(\mathbf{r})) . \quad (11)$$

Explicit expressions for $\text{e}_{\text{xc}}^{\text{hom}}$ can be found in the literature [31]. We mainly use the parameterization of [78] and the more recent one from [79].

One might expect the TDLDA to be good only for systems where the n_{\uparrow} and n_{\downarrow} are sufficiently slowly varying in space as well as in time. However, contrary to this expectation, it is a well-established fact [31] that in the static limit the LDA performs quite well even for strongly inhomogeneous systems such as atoms, molecules and solids. Correspondingly, the TDLDA in practice gives quite good results even for cases of rather rapid time dependence [80,81]. Very recently, attempts have been made to go beyond the adiabatic approximation of the TDLDA and construct an xc potential whose dependence on the density is still local in space but nonlocal in time [67]. Research in that direction is still going on and will hopefully lead to a practicable scheme for a successful treatment of electron dynamics beyond the TDLDA. In the static regime, by contrast, effects beyond LDA are meanwhile well explored, and they will also play a role in dynamical applications. In static DFT, LDA can be improved in two respects:

(i) Nonlocalities are completely neglected in E_{xc}^{LDA} , i.e., the xc potential at point \mathbf{r} is entirely determined by the density at the very same point \mathbf{r} . This deficiency is partly remedied by constructing functionals that also depend on the gradients of the density, which leads to the concept of the generalized gradient approximation (GGA) [32–34]. In comparison with LDA, the GGAs tend to improve total energies, atomization energies, energy barriers and structural differences in atoms and molecules [34]. However, the situation is less pressing for metal clusters due to their softer shapes. We thus ignore gradient corrections in the following.

(ii) The LDA total-energy functional contains a self-interaction error. We comment on that aspect in more detail in the following subsection.

2.3.2. Self-interaction correction

The self-interaction error arises from the fact that the self-Coulomb energy contained in the Hartree potential (9) is not canceled exactly by the LDA exchange term, as it is naturally the case in Hartree–Fock. As a consequence, $v_{xc\sigma}^{LDA}$ falls off exponentially for large r , while the exact xc potential should fall off as $-1/r$ for neutral systems.

Various approaches to derive self-interaction corrected functionals have been proposed. So far, most calculations have been performed with the SIC functional of Perdew and Zunger [35], which consists in modifying the Kohn–Sham potential as

$$v_{j\sigma}^{SIC}(\mathbf{r}) = v_0(\mathbf{r}) + v_H[n](\mathbf{r}) + u_{xcj\sigma}^{SIC}(\mathbf{r}) . \quad (12)$$

Here, $v_{ext}(\mathbf{r})$ and $v_H[n](\mathbf{r})$ are the same as in the standard Kohn–Sham potential. The xc potential within SIC, e.g. for a spin-up particle in state j , is given by

$$u_{xcj\uparrow}^{SIC}(\mathbf{r}) = v_{xc\uparrow}^{app}[n_{\uparrow}, n_{\downarrow}] - v_H[n_{j\uparrow}](\mathbf{r}) - v_{xc\uparrow}^{app}[n_{j\uparrow}, 0] , \quad (13)$$

where $v_{xc\sigma}^{app}$ stands for an approximate (not self-interaction corrected) xc potential such as $v_{xc\sigma}^{LDA}$, and $n_{j\sigma} = |\varphi_{j\sigma}|^2$. The self-interaction error is thus explicitly subtracted for each orbital from the standard Kohn–Sham xc potential. But the SIC prescription suffers from the formal difficulty that it leads to state-dependent Kohn–Sham potentials and thereby complicates the self-consistent calculations considerably. The single-particle orbitals are no longer orthogonal and must, at least in principle, be reorthogonalized. It can be imagined that an attempt to generalize this procedure to the time-dependent case would introduce additional intricacies. In the following, we present a method which allows one to eliminate the self-interaction error without running into these problems.

The method of the optimized effective potential (OEP) [82–84] has recently been applied with great success to the description of atomic and molecular ground-state properties [85,86]. The static OEP scheme is based on the following idea. Given an expression of the total energy E of a system, written as a functional of a set of single-particle orbitals $\{\varphi_{j\sigma}\}$, one wants to find those orbitals that minimize $E[\{\varphi_{j\sigma}\}]$ under the constraint that they satisfy a Schrödinger equation with a *common local* potential. If one were to use this prescription with an xc energy expression that is a functional of the density (such as the LDA xc energy), the OEP method would lead back to the ordinary Kohn–Sham scheme of DFT, with the xc potential defined as usual as functional derivative of E_{xc} with respect to the density. In the general case where E_{xc} is assumed to depend explicitly on the orbitals, however, the local xc potential $v_{xc\sigma}^{\text{OEP}}(\mathbf{r})$ is determined in a more complicated way by solving an integral equation. So far, this has been only possible for simple cases such as isolated spherical atoms.

The OEP scheme has furthermore been generalized to the time-dependent case [64,65,87]. Again, the time-dependent xc potential is determined by an integral equation which now has to be solved at each time step, making it a computationally extremely demanding procedure.

Fortunately, there exists a simplified scheme, originally proposed by Krieger et al. for the static case [84] (widely known as KLI scheme) and later extended into the time-dependent domain [87], which yields approximations to $v_{xc\sigma}^{\text{OEP}}$ as *explicit* functionals of the orbitals. In the static KLI scheme, the xc potential is given by

$$v_{xc\sigma}^{\text{KLI}}(\mathbf{r}) = \sum_j^{N_\sigma} \frac{n_{j\sigma}(\mathbf{r})}{n_\sigma(\mathbf{r})} \left\{ u_{xcj\sigma}(\mathbf{r}) + \int d^3r' n_{j\sigma}(\mathbf{r}') [v_{xc\sigma}^{\text{KLI}}(\mathbf{r}') - u_{xcj\sigma}(\mathbf{r}')] \right\} \quad (14)$$

with $u_{xcj\sigma}(\mathbf{r}) = \delta E_{xc}[\{\varphi_{j\sigma}\}]/\delta n_{j\sigma}(\mathbf{r})$. Eq. (14) still has to be solved for $v_{xc\sigma}^{\text{KLI}}$, which is easily accomplished [84], the solution only involving the inversion of an $(N_\sigma - 1) \times (N_\sigma - 1)$ matrix. Note also that, even in this simplified form, the KLI method still requires evaluation of one Coulomb integral per orbital, which may represent a rather time-consuming part of the numerical scheme.

A very common choice for $E_{xc}[\{\varphi_{j\sigma}\}]$, which defines the exchange-only limit of DFT, is the Fock exchange energy. Another popular choice (that we shall adopt in the following) is the SIC xc energy [83,88]. In the corresponding KLI-SIC scheme one then uses the form (13) for $u_{xcj\sigma}$. It has been demonstrated for the case of atoms in [88] that the KLI-SIC method provides an excellent approximation to the full OEP-SIC scheme. Both are practically equivalent to (though conceptually and computationally simpler than) the conventional SIC approach à la Perdew and Zunger [35]. In particular, they yield atomic xc potentials with the correct large- r behavior, leading to very accurate ionization potentials and electron affinities.

The time-dependent version of scheme (14), to be called (TD) KLI-SIC or TDSIC, has only been explored in its adiabatic version yet ($n_{j\sigma}(\mathbf{r}) \rightarrow n_{j\sigma}(\mathbf{r}, t)$). Such applications of the (TD)KLI-SIC scheme to atomic ground state and dynamic properties, performed independently from the present work, have recently been reported in [89]. The TDSIC approach has furthermore been applied to the case of metal clusters irradiated by intense laser beams in [90].

The KLI scheme can be even further simplified. By neglecting the orbital-dependent constants in Eq. (14), one arrives at the so-called Slater potential

$$v_{xc\sigma}^{\text{Slater}}(\mathbf{r}) = \sum_j^{N_\sigma} \frac{n_{j\sigma}(\mathbf{r})}{n_\sigma(\mathbf{r})} u_{xcj\sigma}(\mathbf{r}) . \quad (15)$$

But in spite of its simple form, the Slater-SIC approximation still requires some effort to compute the Hartree potential $v_{\text{H}}[n_{j\sigma}]$ for each of the N_{σ} orbitals. There exists an even simpler approach which replaces the local averaging in Eq. (15) by a global one [91]. Within this global averaging method (GAM), the xc potential is determined by

$$v_{\text{xc}\sigma}^{\text{GAM}}(\mathbf{r}) = \frac{1}{N_{\sigma}} \sum_j^{N_{\sigma}} f_{j\sigma} u_{\text{xc}j\sigma}(\mathbf{r}), \quad (16)$$

where the $f_{j\sigma} = \int d^3r n_{j\sigma}$ are occupation numbers for the single-particle orbitals. In case of SIC the single-particle Hartree potentials just add up, and we finally obtain the simple approximation

$$v_{\text{xc}\uparrow}^{\text{GAM-SIC}}(\mathbf{r}) = v_{\text{xc}\uparrow}[n_{\uparrow}, n_{\downarrow}](\mathbf{r}) - \frac{1}{N_{\uparrow}} v_{\text{H}}[n_{\uparrow}](\mathbf{r}) - \frac{1}{N_{\uparrow}} \sum_j^{N_{\uparrow}} f_{j\uparrow} v_{\text{xc}\uparrow}[n_{j\uparrow}, 0](\mathbf{r}) \quad (17)$$

and likewise for spin-down. Note again that the time-dependent versions of the KLI, Slater and GAM xc potentials are obtained by simply replacing the static orbitals and densities with the time-dependent ones.

All three explicit schemes presented here, KLI, Slater and GAM, remove the self-interaction error in the sense that they are exact for systems with a single electron only. For systems with N electrons, they all have the same correct $-1/r$ behavior for large r . However, some differences occur in the small- r regime: generally speaking, the Slater xc potential is slightly too deep in the core region of atoms and clusters, and the GAM potential even more, so that the associated total energies tend to become too negative. It turns out, however, that GAM provides a good description of single-particle energies [91] and the gross properties of dynamical observables as, e.g., optical response and separation energies [92].

2.4. Description of the positive ionic background

2.4.1. Pseudopotentials

When an explicit account of the ionic structure is necessary, we describe the interaction between ions and valence electrons in the standard manner by pseudopotentials. There is a huge variety of them available in the literature. They often possess a very elaborate structure involving projection operators, which are somewhat cumbersome to handle [43]. In practice, one would prefer to work with local pseudopotentials [48]. Fortunately, most simple metals (e.g. Na, K, Cs) can be treated fairly well in this way. Other materials, however, require the fully fledged forms including projectors, for example the pseudopotentials of [93,94] which give access to a wide variety of materials and have been used in cluster physics, e.g., for carbon systems [95] or ferromagnetic clusters [96]. Other choices are the pseudopotentials from [97] that have been used for treating clusters with Li, Ag and C [17,98]. All these pseudopotentials are parametrized using a soft Gaussian shape, which is very efficient in connection with coordinate-grid techniques. In any case, one has to be aware of the fact that available pseudopotentials are designed to optimize *static* structural properties. A predictive value for *dynamical* features (as e.g. plasmon frequency) is not guaranteed and needs to be checked for each pseudopotential anew. The more elaborate pseudopotentials seem to perform immediately fairly well, while local pseudopotentials can cause more problems. One thus often recurs to a slight readjustment of given forms to reproduce plasmon

properties, as e.g. in [68]. On the other hand, new parameterizations have been developed only recently that are particularly designed for dynamical properties [99,58].

As pointed out above, Na clusters allow one to use local pseudopotentials, which will be our choice in most of our calculations. In practice, we employ a soft shape in terms of error functions (in atomic units)

$$v_{\text{ps}}(\mathbf{r} - \mathbf{R}_I) = \sum_{i=1,2} c_i \frac{\text{erf}(|(\mathbf{r} - \mathbf{R}_I)|/\sqrt{2}\sigma_i)}{|\vec{r} - \vec{R}|}, \quad (18)$$

where $\text{erf}(r) = \int_0^r dr' \exp(-r'^2/2\sigma_i^2)$, so that the total ionic contribution to the external potential reads

$$v_{\text{ion}}(\mathbf{r}, t) = \sum_I v_{\text{ps}}(\mathbf{r} - \mathbf{R}_I). \quad (19)$$

In earlier applications [68], we employed parameters taken over from the local part of the pseudopotentials of [100]. But recently, the parameters entering Eq. (18) have been optimized with respect to the properties of the Na atom as well as to key features of the bulk, since finite clusters constitute an interpolation between these two limits. Indeed, it turns out that the so defined pseudopotential provides both appropriate binding energies and the correct plasmon position [99,58]. Our calculations then yield results comparable to the ones attained in quantum chemistry [7]. The actual parameters are [58]

$$\sigma_1 = 0.881a_0, \quad \sigma_2 = 1.163a_0, \quad c_1 = -2.292, \quad c_2 = 3.292. \quad (20)$$

This is the set of parameters which we have used in most of the calculations presented below in sodium with explicit ionic background (although in a few cases we recur to earlier parameterizations). In the case of covalent clusters, such as carbon chains, we use the nonlocal pseudopotentials of [93].

2.4.2. Ionic propagation

A proper treatment of the ions is essential in the static as well as in the dynamic part of the calculations. The optimization of ion positions in the stationary ground state is done with Monte-Carlo techniques as explained in Section 2.5. Concerning the dynamics, it is well known that ionic motion proceeds at a much slower pace than electronic dynamics. Still, when one aims at following the dynamics over more than a few hundred fs (e.g., to explore Coulomb explosion of laser-irradiated clusters [68]), one needs to explicitly account for ionic motion. We then treat the ions as classical particles described within standard (although nonadiabatic) molecular dynamics. The force acting on the ions originates from the electrons (through the above described pseudopotential), from ion–ion interactions (treated here as point charges) and from the external field (laser, projectile). For ion number I , the equations of motion read

$$\frac{d}{dt} \mathbf{P}_I = -\nabla_{\mathbf{R}_I} \left[v_{\text{ext}}(\mathbf{R}_I, t) - \int d\mathbf{r} n(\mathbf{r}, t) v_{\text{ps}}(|\mathbf{R}_I - \mathbf{r}|) + \sum_{J \neq I} \frac{1}{|\mathbf{R}_I - \mathbf{R}_J|} \right], \quad (21)$$

$$\frac{d}{dt} \mathbf{R}_I = \mathbf{P}_I / M_{\text{ion}}. \quad (22)$$

The above molecular dynamics equations are then solved using the standard and robust leap-frog algorithm [101].

2.4.3. The cylindrically averaged pseudopotential scheme

Fully three-dimensional calculations are of course very expensive. However, most Na clusters have an ionic structure which comes close to axial symmetry (because this is energetically favored). This suggests to simplify the electronic TDLDA calculations by imposing axial symmetry of the electronic mean field. In practice, this means that we employ an axially averaged electronic Kohn–Sham potential v_σ ,

$$v_\sigma^{\text{CAPS}}(r, z; t) = \frac{1}{2\pi} \int_0^{2\pi} d\varphi v_\sigma(x(r, \varphi), y(r, \varphi), z; t) , \quad (23)$$

while the ion–ion interactions are still handled in full three dimensions. The approach is called the cylindrically averaged pseudopotential scheme (CAPS) and was introduced in [50,51]. It has been tested successfully against several more complex calculations [51,54]. The gain in computational efficiency is enormous. CAPS is thus an ideal tool for exploratory studies with systematic variations of parameters and external conditions. Fine details, of course, will be washed out by CAPS and require the more elaborate fully three-dimensional TDLDA to be recovered. Note finally that the CAPS scheme is not restricted to static problems [102]. Inserting the time-dependent CAPS potential into electronic Kohn–Sham equations and ionic molecular dynamics lead to a time-dependent CAPS model (TDCAPS), which again turns out to provide a fair approximation to the full 3D nonadiabatic TDLDA with ionic molecular dynamics [102].

2.4.4. Jellium approximation

In the violent cluster excitations which we want to describe, the time scale of excitation is so short that, to a very good approximation, the ions can be considered frozen, at least during the excitation process and quite often even during an early stage of the electronic relaxation (typically up to $t \lesssim 100$ fs). One can then further simplify the treatment of the ionic background by switching to a jellium description. It has for example been shown that the gross properties of the plasmon response are little affected by details of the ionic structure, the impact of the latter actually becoming less and less, the stronger the excitation [18]. The ionic background of the cluster (nuclei plus core electrons) can then be described within the so-called “soft” version of the jellium model, in which the (originally) sharp ionic distribution is folded with an Ashcroft pseudopotential [103]. We use here a (possibly deformed) Woods–Saxon profile for the jellium density $\rho_{\text{jel}}(\mathbf{r})$:

$$\rho_{\text{jel}}(\mathbf{r}) = \frac{3}{4\pi r_s^3} \left[1 + \exp\left(\frac{|\mathbf{r}| - R}{r_c \sqrt{3}}\right) \right]^{-1} , \quad (24)$$

where R accounts for the deformation and is defined as

$$R = R(\theta) = R_0 / (1 + \beta_2 Y_{20}(\theta) + \beta_3 Y_{30}(\theta) + \beta_4 Y_{40}(\theta)) . \quad (25)$$

In the above form, the deformation is characterized in terms of spherical harmonics Y_{l0} , while its amplitude is given by the dimensionless coefficients β_l . The radius R_0 is very close to the spherical

sharp radius $R_0 \simeq r_s N^{1/3}$, where r_s is the Wigner–Seitz radius (it is only slightly renormalized to ensure proper normalization of the number of ions). The soft jellium surface, whose width is related to the core radius of the local pseudopotential [104,105,48] (taken to be proportional to the core radius $r_c = 1.73a_0$ of an Ashcroft empty-core pseudopotential [103]), plays a crucial role here, as it provides within $\pm 2\%$ the appropriate position of the Mie plasmon resonance [106,107].

2.5. The actual procedure

In the preceding sections, we have presented a general account of the theoretical background on which our approach to describe the nonlinear dynamics of clusters is based. The material is distributed over several sections. We now want to briefly summarize the basic steps to illustrate the procedure followed in practice.

The electronic structure is governed by the Kohn–Sham Hamiltonian

$$\hat{h}(t) = -(\hbar^2 \nabla^2 / 2m) + v_{\text{ion}}(\mathbf{r}, t) + v_{\text{H}}(\mathbf{r}, t) + v_{\text{xc}\sigma}(\mathbf{r}, t) + v_{\text{ext}}(\mathbf{r}, t) . \quad (26)$$

There are various choices in detail. The potential of the ionic background is usually composed of the individual pseudopotentials as

$$v_{\text{ion}}(\mathbf{r}, t) = \sum_I v_{\text{ps}}(\mathbf{r} - \mathbf{R}_I(t)) \quad (27)$$

(see also Section 2.4.3 for a symmetry-restricted case, on the side of the electrons). Sometimes we recur to the even simpler jellium approach where v_{ion} is replaced by the Coulomb potential of the jellium density (24). A selection of choices also exists for the xc potential $v_{\text{xc}\sigma}$. Usually we work with the LDA form. Critical observables may require, however, some SIC for which we employ the approximations as outlined in Section 2.3.2, mainly the GAM or KLI method.

The behavior of the ions is derived from the total energy $E(\{\mathbf{R}_I\})$. It contains the total electronic energy, the electron–ion interaction energy, and the Coulomb energy of the ionic point charges. The total energy is interpreted as a classical Hamiltonian for ionic molecular dynamics, leading to the equations of motion (21), (22). In the jellium approximation, the detailed ionic positions are averaged out. The ionic distribution (24) is then parametrized in terms of the deformation parameters, and we deal with a total energy of the form $E(\{\beta_{lm}\})$.

The processes we want to investigate always follow the same pattern: initially, the system is in its static ground state and is then strongly perturbed with a perturbation that is switched on at a time $t = t_0$. We monitor the (nonlinear) time evolution of the system and calculate the observables of interest.

The first step is thus to calculate the ground state of the system. This problem in itself can be of considerable complexity, depending on the size of the cluster and on the way of describing its ionic background, see Section 2.4. In each case, we have to calculate the N -electron ground state in a given external potential, which is done using the static density-functional approach. To this end, we solve the standard static Kohn–Sham equation [31]

$$\hat{h}(t_0)\varphi_{j\sigma}(\mathbf{r}) = \varepsilon_{j\sigma}\varphi_{j\sigma}(\mathbf{r}) , \quad (28)$$

\hat{h} being given in Eq. (26), where the external potential v_{ext} is set to zero because no excitation mechanism should be active in that stage. Since the Hamiltonian depends on the density

$n(\mathbf{r}) = \sum_{j\sigma} |\varphi_{j\sigma}(\mathbf{r})|^2$, the Kohn–Sham equation has to be solved self-consistently (numerical details will be given in Section 3). The optimization of the ionic configuration $\{R_I\}$ is done by simulated annealing using Monte-Carlo techniques which are interlaced with the solution of the electronic Kohn–Sham equations (see again Section 3). The case of jellium background is simpler because there are only few ionic “coordinates” β_{lm} . The optimal coordinates are usually determined by computing the energy landscape $E(\{\beta_{lm}\})$ and searching for the minimum with standard techniques.

Once the ionic structure and the electronic ground state have been found, we are ready for the second step, namely the calculation of the time evolution of the system under the influence of external perturbations. These are modeled as local and time-dependent external potential v_{ext} , and there are various choices, see Section 4.1. Again, we can distinguish two situations: either, the ionic background is kept fixed, or the ionic positions are allowed to change in time. The physical significance and range of validity of these two possibilities have been discussed in the introduction and will be further investigated later on.

The dynamics of the occupied Kohn–Sham orbitals is determined by the time-dependent Kohn–Sham equation

$$i\partial_t \varphi_{j\sigma}(\mathbf{r}, t) = \hat{h}(t) \varphi_{j\sigma}(\mathbf{r}, t) \quad (29)$$

under the initial conditions $\{\varphi_{j\sigma}(\mathbf{r}, t_0), R_I(t_0)\}$. Eq. (29) is solved using the Crank–Nicolson scheme (in cylindrical symmetry) or the time-splitting method (in full 3D calculations). We shall present the numerical procedure for time propagation of the electrons in Section 3. Ionic motion is treated simultaneously according to Eqs. (21), (22), using the leap-frog algorithm. If only short time spans (≤ 100 fs) are considered, one is allowed to freeze the ions at their initial positions and one only needs to propagate the electrons. The same holds if the jellium model is used.

2.6. Semiclassical approximations

2.6.1. The Vlasov equation

The high-energy situations we aim at describing here may not always require the use of a fully fledged quantum formalism. Indeed, semiclassical methods have been developed and used in cluster physics for a few years now [20,21,72]. In particular, the treatment of collisions between highly charged ions and metal clusters has met some success [21,20] (see also Section 6). The advantage of semiclassical approaches is that they permit the treatment of large clusters [72], although quantum calculations are catching up [108]. More interesting is the fact that, to the extent that they become justified at high excitation energy, the semiclassical approximation of TDLDA constitutes a well-established basis for the construction of more elaborate versions of the theory which go beyond the mere TDLDA mean field, by including explicit electron–electron collisions. This “beyond the mean field” path has been attacked only very recently [23,109] but promises to constitute a useful, and sometimes indispensable, tool for investigating the dynamics of clusters in the domain strongly out of equilibrium.

The simplest semiclassical approximation can be derived directly from TDLDA. It is convenient to reformulate the latter approach in terms of the one-body density operator $\hat{\rho}$:

$$\dot{\hat{\rho}} = (1/i\hbar)[\hat{h}(\hat{\rho}), \hat{\rho}] , \quad (30)$$

where \hat{h} denotes the single-particle KS Hamiltonian. The operator form (30) of the Kohn–Sham equations is well suited to formal manipulations, e.g. for going “beyond” mean field in the realm of kinetic equations, or for deducing semiclassical approximations [110]. The Vlasov equation naturally emerges as the semiclassical limit of Eq. (30). Following the usual rule of thumb, it can be formally obtained from the quantal equation (30) via replacing the density operator $\hat{\rho}$ with a one-body phase space distribution $f(\mathbf{r}, \mathbf{p}, t)$ and the commutator with Poisson brackets [110]:

$$\begin{aligned}\hat{\rho}(\mathbf{r}, \mathbf{r}') &\rightarrow f(\mathbf{r}, \mathbf{p}, t) , \\ [\cdot, \cdot] &\rightarrow \{\cdot, \cdot\} .\end{aligned}\tag{31}$$

This then leads to the Vlasov equation

$$\partial f(\mathbf{r}, \mathbf{p}, t) / \partial t + \{f, h\} = 0 ,\tag{32}$$

where h is now the classical mean field Hamiltonian depending on the (semiclassical) electron density $\varrho(\mathbf{r}, t)$, which is now computed as the integral of $f(\mathbf{r}, \mathbf{p}, t)$ over momentum space:

$$\varrho(\mathbf{r}, t) = \int d^3p f(\mathbf{r}, \mathbf{p}, t) .\tag{33}$$

The semiclassical approximation step leading from Eqs. (30) to (32) still has to be performed with due caution. The problem lies at the formal level, in terms of the related expansion in \hbar . A thorough discussion of this problem can be found in [111–113]. Another difficulty with Eq. (32) concerns the capability of numerical simulations to preserve Fermi statistics on long times [114]. This disease can be cured at the Vlasov level by adding an artificial collision term tailored to restore the fermionic condition $f(\mathbf{r}, \mathbf{p}, t) \leq 1$ [115,116]. The inclusion of two-electron collisions (see Section 2.6.2) also helps (and usually suffices) to restore fermionic features.

Up to now, most Vlasov (and VUU, Section 2.6.2) calculations have been performed using a jellium model for the ionic background [20,21,72]. This is fully compatible with the short time scales that have so far been investigated with such models. However, a proper account of ionic structure with pseudopotentials is desirable as it would allow us to consider situations in which the coupling to ionic degrees of freedom becomes very rapid [117]. As already stressed, such strongly out of equilibrium situations typically belong to the realm of semiclassical methods. Although appealing experimental results (in particular with intense lasers) have started to pile up [13], this issue is still only little explored by theory. A first attempt to treat ions with pseudopotentials and electrons at Vlasov or VUU levels was published very recently [117], confirming the feasibility of such calculations, as hinted in earlier Thomas–Fermi calculations [118,119].

2.6.2. Beyond mean field – the VUU equation

The Vlasov equation represents the basic level of the hierarchy of many-body dynamical equations [120]. It is justified in dynamical situations where dissipative effects are not too large, just as its quantal cousin TDLDA. But dynamical correlations, not accounted for at mean field level, are known to play a key role in the dynamics of highly dissipative systems. They first show up at the level of two-body effects and usually at a faster time scale than the mean field motion, so that they can be approximated by instantaneous two-body collisions (leading to a Markovian collision

term). This yields the Vlasov–Boltzmann equation for classical systems. For dense fermion systems, such as metal clusters, atomic nuclei or liquid helium, the appropriate statistics has to be built in. This then leads to the so-called Vlasov–Uehling–Uhlenbeck (VUU) scheme, which has been intensely studied during the last two decades in nuclear physics [121–123]. The resulting VUU equation reads

$$\partial f / \partial t + \{f, h\} = I_{\text{VUU}}[f(\mathbf{r}, \mathbf{p}, t)] \quad (34)$$

with

$$I_{\text{VUU}} = \int d\mathbf{p}_2 d\mathbf{p}_3 d\mathbf{p}_4 W(12, 34)(f_{12}^{\text{in}} f_{34}^{\text{out}} - f_{12}^{\text{out}} f_{34}^{\text{in}}), \quad (35)$$

where $W(12, 34)$ is the collision rate

$$W(12, 34) = (d\sigma/d\omega)\delta(\mathbf{p}_1 + \mathbf{p}_2 - \mathbf{p}_3 - \mathbf{p}_4)\delta((p_1^2/2m) + (p_2^2/2m) - (p_3^2/2m) - (p_4^2/2m)). \quad (36)$$

The collision rate is expressed in terms of the elementary cross section $d\sigma/d\omega$ which constitutes a key ingredient of the approach. In Eq. (35), “in” and “out” label the distribution of particles entering or exiting a two body collision ($12 \leftrightarrow 34$), such that $f_{ij}^{\text{in}} = f_i f_j$, $f_{kl}^{\text{out}} = (1 - f_k)(1 - f_l)$, with the short-hand notation $f_i = f(\mathbf{r}, \mathbf{p}_i, t)$. Note that the Pauli principle explicitly shows up in the blocking terms f_{kl}^{out} , imposing that f has to be less than 1, which implies that not more than 1 particle, or 2 with opposite spins, can occupy a phase space cell of volume $(2\pi\hbar)^3$. This blocking factor plays a dramatic role for electronic systems [26]. At $T = 0$ K, all the collisions are Pauli blocked and the mean-free path of the electrons becomes infinite. When the system is hot or sufficiently excited, phase space opens up and two-body collisions start to play a (possibly leading) role.

One should insist here upon the fact that this VUU scheme only represents a first exploratory step in the direction of accounting for dynamical correlations. There is indeed the key question of a possible double counting of interactions between the mean field term and the collision term, which has not yet been fully explored in the case of clusters. However, one can exploit results obtained in related fields of physics, in which a similar question has been addressed in full detail. One can thus rely here on the experience gathered in nuclear dynamics [124] and in the physics of plasmas [125], or liquid helium [126]. It turns out that there is no problem as long as collisions are treated in Markovian approximation (i.e. as instantaneous) [124]. The rule is then to use the LDA for the mean field and a screened Coulomb cross section in the collision integral. In the cluster case an explicit reevaluation of the cross section [23] actually leads to values in agreement with the bulk values obtained from condensed matter calculations [127]. Once the model has been established, the impact of dynamical correlations on cluster dynamics can be tested systematically in schematic calculations [23] or even in realistic cases [109]. We shall come back to these results at some places below.

2.6.3. Time-dependent Thomas–Fermi approximation

Both Vlasov and VUU approaches provide a phase space description of electron dynamics, which allows one to treat a wide range of electronic excitations. A full phase space description can indeed accommodate possibly large distortions of the local Fermi sphere, a feature typical of strongly out of equilibrium dynamics (see for example the case of violent nuclear collisions).

However, it turns out that in the case of metal clusters two effects tend to suppress these local distortions. On the one hand, there is always the dominating presence of the Mie plasmon mode which carries little momentum space anisotropy. Electron–electron collisions, on the other hand, act on very short time scales of order a few fs and tend to remove remaining momentum sphere anisotropies very quickly. Altogether, it thus turns out that, to a very good approximation, the local momentum distribution of electrons becomes basically spherical, very soon after the excitation itself [73]. This constitutes a strong justification for going one step further in the semiclassical approximation by integrating the dynamics over momentum space, which leads to the so-called time-dependent Thomas–Fermi (TDTF) approximation. This TDTF picture is nothing but a hydrodynamical reformulation of the original problem, assuming a Thomas–Fermi kinetic energy for the electrons. Note that the TDTF approximation can be formally derived either from the Vlasov equation by integration over momentum space, or directly from TDLDA by a proper choice of a model wavefunction [128,73]. In both cases one ends up with coupled equations for the local density $\varrho(\mathbf{r})$ and local velocity field $\mathbf{u}(\mathbf{r}) = \nabla\chi$:

$$\partial\rho/\partial t + \nabla\cdot(\rho\mathbf{u}) = 0 , \quad (37)$$

$$m(\partial\chi/\partial t) + (m/2)(\nabla\chi)^2 + (\delta U/\delta\rho) + (\delta T/\delta\rho) = 0 . \quad (38)$$

Dissipative versions of the theory can also be worked out, although no applications to clusters have yet been published, to the best of our knowledge. It should also be noted that TDTF represents a genuine density-functional method (see Ref. [31] for more details about the static Thomas–Fermi approach). The theory does not involve any orbitals like in the Kohn–Sham scheme, but focuses on the density and current only. The approximation lies here in the treatment of the kinetic energy functional.

In the case of cluster dynamics, the full 3D TDTF approximation has been explored in [73,119] and has been shown to provide a fairly good replacement for TDLDA, even for moderate excitations. Simpler versions of TDTF imposing a restriction to 1D (which is appropriate for dimers) have also been investigated recently, in direct relation to irradiation by intense lasers [129–131]. An explicit account of the ionic background by means of pseudopotentials has even shed some light on the local behavior of collective currents during Mie plasmon oscillations. The TDTF picture provides here an ideal tool to disentangle collective from particle–hole excitations in the optical response [119]. The coupling to ion dynamics also promises to be an interesting application, since TDTF by construction allows one to explore nonadiabatic effects. This would complement the Thomas–Fermi molecular dynamics calculations of [70] in which electrons are restricted to the ground-state Born–Oppenheimer surface of the ionic configuration at any instant.

3. Numerical aspects

In this part we outline the numerical techniques to solve the equations for electronic dynamics in metal clusters. We focus in particular on the grid techniques for the quantal TDLDA equations. We also say a few words about the numerical methods used in Vlasov and VUU simulations.

3.1. *Choice of the numerical representation*

It is customary in atomic or molecular physics to project the electronic wavefunctions on various well-suited bases. A typical example is the use of Gaussian basis sets. However, these popular basis sets, although very convenient when adapted to the shape and symmetries of the wavefunctions, turn their advantages into drawbacks when one needs to consider arbitrary excitations of the electronic wavefunctions. Similar difficulties occur when computing the simultaneous evolution of the nuclear positions and of the electronic wavefunctions. The results of [132], where the collisional cross section of Cs against sodium clusters is computed with nonadiabatic molecular dynamics, are illustrative in this respect. The choice of a linear combination of atomic orbitals (LCAO) to represent the electronic wavefunctions leads in this case to a very fast numerical scheme, but makes it nearly impossible to correctly model the emission of electrons from sodium clusters. Solid state physicists normally use plane waves basis sets, which is the appropriate starting point to describe systems with periodic boundary conditions. Metal clusters, however, are finite and localized in real space. These considerations suggest to use a coordinate-space grid representation of the electronic wavefunctions. This turns out to provide a most efficient and flexible method for many purposes, in particular in the computationally demanding field of nonadiabatic cluster dynamics.

Grid techniques have lately been used by several groups for describing cluster dynamics. Fission of small multicharged sodium clusters was described with Born–Oppenheimer molecular dynamics in [69], representing the electronic wavefunctions on a three-dimensional real-space grid. More recently, Yabana and Bertsch [17] have applied full TDLDA to several molecules and clusters, even containing the numerically demanding lithium and carbon elements. They use a real-space full 3D grid representation of the electronic wavefunctions, following techniques very similar to the ones we shall discuss here [16,18,57,133]. Although in a slightly different theoretical framework, which is not directly discussed here, Blaise et al. have also used regular direct space grids [70] in their investigations of the fragmentation of small sodium clusters. They use an adiabatic Thomas–Fermi description of the electronic cloud, thus generating a Thomas–Fermi approximation to the standard Car–Parinello technique [55]. Along similar lines, vibrational spectra in molecules have been obtained using a combination of molecular dynamics and DFT where the electronic wavefunctions are also represented on regular real-space grids [134].

Grid techniques have taken advantage of the numerical developments in nuclear physics for solving the time-dependent Hartree–Fock (TDHF) equation, which is nothing but the nuclear cousin of TDLDA [135]. In most of the nuclear calculations the wavefunctions of the nucleons were also represented on real-space regular grids. These methods actually turned out to be quite powerful [136]. The main reason for their success is that nuclear matter is a Fermion system with a well-defined saturation point, i.e. a system which tries to stay close to its equilibrium density. The same holds for the valence electrons of simple metals. It is thus quite natural to apply to metallic clusters the techniques that were used with success in nuclear physics and thus to use real-space grids. It comes as no surprise that the today’s best working codes for nonlinear TDLDA have indeed been developed from nuclear TDHF codes.

3.2. *Solving TDLDA on a grid*

We aim at solving the TDLDA problem for a system of several initial wavefunctions excited by an arbitrary operator. The two steps of the numerical procedure for the electrons are:

- (i) computation of the initial condition (usually the ground state of a cluster) by the solution of the static Kohn–Sham equations (28);
 - (ii) solution of the time-dependent Kohn–Sham equations for the desired time interval.
- All these calculations (ground-state and dynamical) imply the solution of a Poisson equation, and the computation of observables such as multipole moments or the total energy.

We solve the quantal TDLDA equation either in 2D cylindrical or in full 3D geometry (without symmetry restriction). The 2D calculations allow for systematic exploratory calculations, while the 3D computations provide the more realistic approach. The 2D geometry permits the treatment of possibly large clusters (up to 100 atoms and more). The 3D simulations are limited to small or intermediate size clusters (10–40 atoms) but provide the most sophisticated treatment.

3.2.1. Initial condition

The first step is to compute the cluster ground state via solution of static Kohn–Sham equations (28) for a given ionic configuration. The computation of the ground state is complicated by the self-consistent nature of the equations. An iterative method is thus the natural way to solve this set of equations. We use either the imaginary time step method or the damped gradient method [136,133]. In both cases a given set $\varphi_i^{(n)}$ of approximate single-particle wavefunctions is improved by a step

$$\varphi_i^{(n+1)} = \mathcal{O}\{\varphi_i^{(n)} - \mathcal{D}(\hat{h}^{(n)} - \langle \hat{h}^{(n)} \rangle) \varphi_i^{(n)}\}, \quad (39)$$

where \mathcal{O} stands for orthonormalization of the φ_i 's. The damping operator \mathcal{D} needs to be chosen such that the iteration converges. In the imaginary time method one just takes a sufficiently small number $\mathcal{D} = \delta$ such that $\delta < 2\varepsilon_{\max}^{-1}$, where ε_{\max} is the largest possible single-particle energy in the given numerical representation. The damped gradient method instead employs the damping operator

$$\mathcal{D} = \delta/(\hat{T} + E_0), \quad (40)$$

where \hat{T} is the operator of the kinetic energy, δ is a numerical parameter setting the size of the step, and E_0 is a numerical parameter stabilizing the inversion (because the kinetic energy has eigenvalues close to zero). The orthonormalization of the wavefunctions at each step is done by Schmidt orthogonalization.

Any iterative method needs a reasonable initial guess. For sodium clusters, we take the eigenfunctions of a deformed harmonic oscillator, the deformation parameters describing the global shape of the ionic or jellium background. For clusters closer to covalent binding, such as carbon chains, it is preferable to initialize the wavefunctions as a linear combination of atomic orbitals respecting the overall symmetry of the cluster.

A pertinent choice for the symmetry of the initial wavefunctions or their spin is not obvious at the beginning. We solve that problem by a variant of simulated annealing. To this end, we consider a thermalized ensemble of wavefunctions, with correspondingly fractional occupation numbers. With a sufficiently large number of wavefunctions in the iterative process all the possibilities in terms of wavefunction symmetries or spin are then explored. During this process, one must progressively reduce the temperature and at the end one finds the wavefunctions with the lowest energy with occupation numbers properly set to one.

3.2.2. The Poisson equation

The Poisson equation is a central ingredient for determining both the initial condition and the dynamics. The task is to find the Hartree potential v_H . It turns out that a direct numerical solution of the integral in Eq. (9) is computationally too demanding. Instead, it is more efficient to calculate v_H via the Poisson equation (in atomic units)

$$\nabla^2 v_H(\mathbf{r}, t) = -4\pi n(\mathbf{r}, t) . \quad (41)$$

Eq. (41) can be solved iteratively, starting with some approximation and applying accelerated iterations of the equation, with fixed boundary conditions. This is the essence of methods such as the successive over-relaxation (SOR) method, which was the method of choice in our 2D calculations [18]. Although this method is relatively slow, and lacks high precision due to the need to estimate the Laplacian by a 3 or 5 points finite difference method, it is extremely robust and efficient in 2D calculations.

In our 3D simulations the Laplacian in the Poisson equation is evaluated using fast Fourier transform (FFT). The long-range part of the Coulomb field is handled separately to avoid problems with periodic copies of the fields. This is the essence of the so-called FALR (Fourier Analysis with Long Range Forces) method [137]. This method is fast and accurate, and, as many numerical schemes based on FFT, very robust. One can also benefit from the carefully optimized single or multidimensional FFTs available on many types of workstations or supercomputers. This FALR Poisson solver has also been used with success in our semiclassical calculations, see Section 3.4.

3.2.3. Wavefunction propagation

We now turn to the problem of solving the time-dependent Kohn–Sham equations (29) on a long enough time interval. The starting point for the development of propagation schemes over a time interval Δt is the formally exact solution

$$\varphi_i(t + \Delta t) = \mathcal{T} \exp\left(-i \int_t^{t+\Delta t} dt' \hat{h}[n(t')]\right) \varphi_i(t) , \quad (42)$$

where \mathcal{T} is the time ordering operator and $\hat{h} = \hat{T} + V[n(\mathbf{r}, t), t]$ the one-body Hamiltonian (with obvious notations).

In 2D calculations we have used the Peaceman–Rachford step, which is a separable approach to the Crank–Nicolson method [138,139]. The Crank–Nicolson step replaces the exponential in Eq. (42) by the lowest order rational approximant:

$$\varphi_i(t + \Delta t) \approx [1 + (i/2)\hat{h}\Delta t]^{-1} [1 - (i/2)\hat{h}\Delta t] \varphi_i(t) . \quad (43)$$

This propagation scheme is correct up to second order in Δt and strictly unitary. The inversion, however, can become very expensive in two or three dimensions. Therefore, the single-particle Hamiltonian operator \hat{h} is split in so-called “horizontal” and “vertical” parts, $\hat{h} = \hat{h}_h + \hat{h}_v$, corresponding to the action along the radial (r) and azimuthal (z) axis, respectively. With three-point finite-differences formulas for the derivatives, \hat{h}_h and \hat{h}_v are reduced to tridiagonal matrices that are easy to invert. This yields the so-called Peaceman–Rachford step:

$$\varphi_i(t + \Delta t) \approx [1 + (i/2)\hat{h}_v\Delta t]^{-1} [1 + (i/2)\hat{h}_h\Delta t]^{-1} [1 - (i/2)\hat{h}_h\Delta t] [1 - (i/2)\hat{h}_v\Delta t] \varphi_i(t) . \quad (44)$$

This step is numerically much faster than Crank–Nicolson and exact in $\mathcal{O}(\Delta t)^2$, too. However, it does not guarantee anymore strict unitarity because \hat{h}_v and \hat{h}_h do not necessarily commute. But in practice, the orthonormalization remains sufficiently well conserved. The Peaceman–Rachford method has been successfully applied in various nuclear TDHF calculations, see [135] and references therein. The self-consistent nature of the mean field Hamiltonian still raises the question of the instant at which to evaluate \hat{h} . The most symmetric choice is $\hat{h} = \hat{h}(t + \Delta t/2)$, which makes the step of order $(\Delta t)^2$ and provides sufficient energy conservation. In practice, we first take half a time-step from t to $t + \Delta t/2$, using $\hat{h}(t)$ in Eq. (44). The resulting $\varphi_i(t + \Delta t/2)$ then determine $\hat{h}(t + \Delta t/2)$, which in turn is used in (44) to propagate the full step $t \rightarrow t + \Delta t$.

The Peaceman–Rachford method is particularly well suited for discretization schemes where the kinetic energy is represented by low-order finite differences, as is the case in our 2D CAPS code [18]. For the 3D calculations, we use fast Fourier techniques, and here the so-called time-splitting technique is more efficient [140]. The central idea consists in splitting the propagation between kinetic and potential terms, which both will be expressed by exact exponentials. The time step thus employs an interlaced local and kinetic propagation with complex exponentials, i.e.

$$\varphi_i(t + \Delta t) \approx \exp(-i\Delta t \hat{V}(t + \Delta t)/2) \exp(-i\Delta t \hat{T}) \exp(-i\Delta t \hat{V}(t)/2) \varphi_i(t), \quad (45)$$

where the new Kohn–Sham potential \hat{V} is recomputed at each full time step [57,133]. This looks at first glance like an implicit dependence because $\hat{V}(t + \Delta t)$ appears at the right-hand side as well. But the local density is not changed by the term $\exp(-i\Delta t \hat{V}(t + \Delta t)/2)$. Therefore one can evaluate the new density $n(t + \Delta t)$ already after the kinetic step, deduce the new Kohn–Sham potential from that and use it for the final half-potential step. The kinetic step is evaluated by Fourier transforming the wavefunction into momentum space, applying the (then diagonal) kinetic propagator, and transforming back to coordinate space. This time-splitting technique is again accurate up to second order in Δt and requires only one evaluation of the potential per time step, which makes it very similar to the leap-frog method for a system of interacting classical particles [101,141]. Moreover, it is unitary and hence unconditionally stable. This is a great advantage compared to methods where the exponential of the operators is computed by a truncated expansion, although the latter can also be quite accurate when used in conjunction with a predictor–corrector like algorithm [17].

The time-splitting method is numerically particularly advantageous if the potential operator is local in direct space and the kinetic energy operator local in reciprocal (Fourier) space. However, the method has to be modified when nonlocal operators are contained in the Hamiltonian, which occurs for nonlocal pseudopotentials. In that case, we have dealt with the nonlocal part in an additional propagator and treated it with a third-order Taylor expansion of the exponential [95,133]. This is sufficient for this well-localized contribution as one can see from norm conservation during propagation.

3.2.4. Boundary conditions

We have mainly considered two types of boundary conditions: reflecting and absorbing ones. In case of reflecting boundary conditions, the single-particle wavefunctions are simply set to zero at boundary (this is implicit in a Crank–Nicolson-like scheme), which makes them bounce back from the edge of the grid. The advantage of these reflecting boundary conditions is that charge, orthonormalization, and energy are conserved over time. The drawback lies in the fact that electrons should realistically be allowed to fly away freely from the cluster. This latter feature can

be better simulated by using absorbing boundary conditions: a mask function [142] acts on the wavefunctions, at the border of the computational box, to absorb them gradually with (almost) no reflection. The actual implementation is done as follows. First one propagates the single-electron wavefunctions by one time step in the usual manner, $\varphi_j(\mathbf{r}, t) \rightarrow \tilde{\varphi}_j(\mathbf{r}, t + \Delta t)$. Then one attenuates those parts of the wavefunctions located in the boundary zone (a shell of width b_{abs} next to the border of the numerical box) by applying the mask functions as

$$\varphi_j(\mathbf{r}, t + \Delta t) = \mathcal{B}_x(x)\mathcal{B}_y(y)\mathcal{B}_z(z)\tilde{\varphi}_j(\mathbf{r}, t + \Delta t) , \quad (46)$$

where

$$\mathcal{B}_z(z) = \begin{cases} \cos^{1/4}\left(\frac{|z_{\text{max}} - z|\pi}{b_{\text{abs}}}\right) & \text{for } |z_{\text{max}} - z| \leq b_{\text{abs}} , \\ 1 & \text{else} \end{cases} \quad (47)$$

and similarly in x - and y -direction, or r -direction in case of a 2D axial grid. The absorbing boundary conditions look intuitively appealing from a physical point of view. But one has to keep in mind that one thus neglects polarization of the residual cluster by electrons outside the numerical box. One therefore needs to use sufficiently large boxes to curb down errors from this approximation.

3.2.5. Numerical parameters

In any grid-based method, it is obvious that one has to choose a sufficiently large computational box in order to minimize the effects of confinement. This is especially crucial in Coulomb dominated systems with net charges. We have hence chosen very large computational boxes in order to remain on the safe side in this respect; and we have checked that for such large computational boxes any size effects on the observables under consideration are vanishingly small [18]. The number of grid points to use of course depends on the size of the cluster, but also on the nature of the boundary conditions. Indeed, if reflecting boundaries conditions are used, the part of the electronic cloud which is emitted during the initial excitation process hits the walls of the numerical box after a given time and perturbs the dynamics on its way back. If absorbing boundaries conditions are used, or at least periodic ones (the return time is then doubled), a smaller grid size can be used. In 2D calculations our typical computational boxes contain 30–70 (radial direction) \times 100–300 (z direction) grid points, with mesh spacings of order $0.8a_0$. The time step is typically taken as $\Delta t = 0.01$ fs. In 3D we typically use $48 \times 48 \times 48$ grid points with a spacing of $0.8a_0$, and a time step $\Delta t = 0.0048$ fs. Larger clusters $N \approx 20$ or strongly deformed systems require more. We have often used 64 grid points in each direction and occasionally up to 72.

As a final remark we would like to mention a few more technical aspects concerning the performances of our calculations. Large-scale applications in 3D can quickly outgrow present days workstations. We therefore adapted the 3D methods for parallel computers. The most demanding part of the computations is the time propagation of the wavefunctions. Two main guidelines can be considered in order to share the work between the processors. The first possibility is to share the three-dimensional grid between the processors, each of them propagating all the wavefunctions in its restricted domain. Alternatively, each processor can propagate some of the wavefunctions on the whole grid; a mix of these solutions is also feasible. As a first step we have chosen to parallelize one wavefunction “per processor”. This scheme is made extremely easy by the fact that the TDLDA

equations use the same single-particle Hamiltonian for all the wavefunctions with identical spin. Therefore, once the density is known, the action of \hat{h} on the wavefunctions can be directly applied in parallel. The performances of the parallelization are quite satisfying, and indeed allow the treatment of moderate size clusters in an acceptable time. Details on these performances can be found in [143].

3.3. Handling of the ionic background

Several computations were performed for sodium clusters in which the ionic background was adiabatically or nonadiabatically coupled to electrons [143,68], assuming classical dynamics for the ions. This requires additional treatment of the ionic degrees of freedom on top of the electron dynamics.

Before starting the dynamical evolution, one has to compute the ground-state ionic configuration of the cluster. This was done by an unconstrained structural search, fully minimizing the total energy with respect to electronic and ionic degrees of freedom. To find the ground state and stable isomers, the ionic positions were optimized by Monte-Carlo sampling applying the technique of simulated annealing. One Monte-Carlo step looks as follows. Given the actual configuration $\{R_I^{(n)}, \varphi_j^{(n)}\}$, we perform trial steps for single ions. For $I = 1, \dots, N_{\text{ion}}$ we change the position and protocol the energetic consequences,

$$R_I \rightarrow R_I + \delta R_I \Rightarrow E \rightarrow E + \delta E_I, \quad \delta E_I \approx \int d^3r n_{\text{el}}(v_{\text{ion}, R_I} - v_{\text{ion}, R_I + \delta R_I}). \quad (48)$$

Note that the energy change is computed approximately in first-order perturbation theory. The given energy change allows one to compute the weights

$$W = \min(1, e^{-\delta E_I/T}). \quad (49)$$

The new configuration $R_I + \delta R_I$ is accepted with probability W , which then yields the next position $R_I^{(n+1)}$. These trial steps are performed in a sequence through all ions. After this, so many changes have accumulated in the ionic background that one needs a complete update of the electronic state. To this end, one solves the stationary Kohn–Sham equations for the newly given $\{R_I^{(n+1)}\}$, which complements the set as starting point for the next iteration. The temperature T in that step is a numerical parameter. It should be chosen sufficiently large at the beginning to avoid being kept in a local minimum (typically one starts with $T = 1000\text{--}2000$ K). The temperature can then be gradually lowered during the process until it comes close enough to zero. The actual strategy for lowering T depends very much on the particular case under consideration. Good choices require lots of experience. For details see [50,144,51,145].

The dynamical propagation of the ions was carried out with the standard leap-frog (or Verlet) algorithm [101] where the forces and propagation of momenta P_I are computed at the full ionic time steps. The ions move much more slowly than the electrons, so that one has to perform only one ionic step per 10–50 electronic steps. This altogether provides a very fast scheme.

3.4. Vlasov and VUU simulations

In a few applications we have used the Vlasov equation (see Section 2.6.1) or its VUU extension (see Section 2.6.2). We briefly discuss here the numerical methods used to solve both equations. Numerical solution of the Vlasov equation (32) is performed in full 3D (without symmetry restriction) using the test-particle method [141]. The one-body distribution $f(\mathbf{r}, \mathbf{p}, t)$ representing N electrons is projected onto a swarm of ν numerical test particles as

$$f(\mathbf{r}, \mathbf{p}, t) \simeq \frac{N}{\nu} \sum_{i=1}^{\nu} g_r(\mathbf{r} - \mathbf{r}_i(t)) g_p(\mathbf{p} - \mathbf{p}_i(t)) , \quad (50)$$

where g_r and g_p are normalized Gaussian functions with widths σ_r and σ_p . The Vlasov time propagation for f then follows from classical equations of motion for the ν test particles, derived from the Hamiltonian [146]

$$h_\nu(\mathbf{r}_i, \mathbf{p}_i) = \mathbf{p}_i^2/2m + v[\rho](\mathbf{r}, t) \star g_r(\mathbf{r} - \mathbf{r}_i(t)) \quad (51)$$

(the symbol ‘ \star ’ stands here for the folding operation in coordinate space). It has recently been pointed out [146,22] that the finite resolution of this numerical method introduces spurious dissipation into the dynamics. This eventually causes the system to evolve towards a Boltzmann equilibrium regardless of the fermionic nature of the system under consideration. Nevertheless, on the short time scales we restrict ourselves when using the Vlasov equation, fermionic stability can be guaranteed by choosing a large enough number ν of test particles and not too small folding widths σ_r [22,72]. A reasonable compromise for Na systems is $\sigma_r = 1a_0$ and $\nu/N = 1500$, where N is the number of electrons.

The algorithm used to evaluate the VUU collision term is inherited from nuclear physics [121,147]. The test particle representation simplifies the horrible five-fold phase space integration by replacing it with a loop over pairs of test particles 1 and 2. The collision rate is governed by the total cross section $\sigma = \int d\omega d\sigma/d\omega$. The cross section is translated into a scattering distance $d_\sigma^{\text{phys}} = \sqrt{\sigma/\pi}$ that needs to be rescaled to scattering of test particles, yielding an effective distance $d_\sigma^{\text{eff}} = d_\sigma^{\text{phys}} \sqrt{N/\nu}$. The actual sampling of the collision integral then proceeds as follows. Starting from two particles 1 and 2, one evaluates the distance of closest approach d_{\min} of these two particles along their respective trajectories. One first checks whether the particles will actually pass through d_{\min} during the coming time step. One then selects those cases which stay within the effective scattering disk, i.e. for which $d_{\min} \leq d_\sigma^{\text{eff}}$. If both criteria are fulfilled, then we let the two particles collide: $(\mathbf{p}_1, \mathbf{p}_2) \rightarrow (\mathbf{p}'_1, \mathbf{p}'_2)$ in accordance with conservation of energy and total momentum. The remaining freedom in the scattering angle is evaluated stochastically. Finally, Pauli blocking is checked by considering target phase space cells for particles 1 and 2. The decision for a successful event is again sampled stochastically, proportional to the amount of open phase space.

It should finally be noted that the VUU collision integral leads to a fair stabilization of fermion statistics, as compared to Vlasov alone. This was expected from the experience in the nuclear case [146]. However, the effect is here more pronounced so that, at least on the time scales we are interested in, the question of loss of statistics can be assumed to be practically solved in the VUU case.

4. Relation to measurements

After the detailed description of both the underlying formalism and numerical techniques in the preceding Sections 2 and 3 we now turn towards the relation between calculations and measurements. As a first step we discuss how to model the actual excitations of clusters, in particular by ionic projectiles and laser radiation. We next discuss the observables which can be extracted from the simulations, in relation to the quantities actually accessed in experiments (photoabsorption cross sections, ionization, etc.).

4.1. Excitation mechanisms in the nonlinear regime

4.1.1. Collision with highly charged ions

Energetic ions have recently been propounded as an efficient means of producing highly charged but cold clusters [148]. Until relatively recently [149], the standard way to attain high cluster charge states was through low-fluence ns lasers which, while stripping off electrons, sizably heated the cluster. Indeed, the laser pulse length was long enough to allow for thermalization of the ionic degrees of freedom, thus mixing up purely electronic and temperature effects. This has been a source of difficulties in the study of fission [148] or fragmentation [150–153]. By contrast, energetic highly charged ions, as delivered by ECR sources [154], offer an interesting alternative since the interaction time is so short that no heat is directly deposited in the cluster (although, as we shall see, thermalization develops later). Ionization thus essentially takes place in a cold cluster, and one can expect to attain more highly ionized states than with low-fluence lasers. However, as discussed in Section 4.1.3, efficient ionization can also be reached by using powerful fs laser systems. Both laser and ionic excitations are therefore complementary and should be studied in parallel. This poses little conceptual difficulties on the theoretical side, and we present in the following pages both aspects as direct applications of our formalism.

As a first step let us briefly discuss how excitation proceeds in a collision between a cluster and a fast highly charged ion. In connection with the experiments performed in Grenoble [12], we shall focus on the case of medium-size sodium clusters bombarded with projectiles such as protons or highly charged ions (Ar^{8+} or Xe^{25+}). The energy of the ions depends on their mass and charge, but their velocities v_i are all comparable. They are of the order of the Fermi velocity v_F of the electrons inside the cluster, where $v_F \approx 20a_0/\text{fs}$. The value of v_F turns out to be a crucial parameter that determines the time scale of the excitation process. Indeed, the excitation proceeds here at a pace comparable to a typical electronic (hence microscopic) time scale in the cluster. To be a bit more specific, one can define an “interaction time” following standard theory of collisions [155] as $\Delta T_{\text{inter}} \sim 2R/v_i$, where R is the cluster radius. Taking a cluster radius of order 10–20 a_0 leads to $\Delta T_{\text{inter}} \sim 0.5\text{--}1\text{ fs}$ for $v_i = v_F$ (recall that the collective Mie plasmon has a period of order 1.5 fs in sodium clusters). The excitation is thus indeed an extremely short one and, as long as v_i remains of order or larger than v_F , can almost be considered as instantaneous [156]. In the case of smaller ionic velocities (typically $v_i \sim 0.1v_F$), the interaction time is about 5–10 fs and starts to be long enough to interfere with other electronic processes (emission, Landau damping), see Section 6.4.

Because the ionic projectile is both fast and massive, its trajectory is only little affected by its interaction with the cluster. To a very good approximation its motion will proceed on a straight line with constant velocity. The entire reaction takes place in a plane that is defined by the path of

the ion (taken here along the x -direction) and the line connecting the center of the cluster and the point of closest approach. The length of this line, taken along the z -axis, defines the impact parameter b . We restrict our discussion to cases for which b is sizably larger than the cluster radius, so that the ion can be viewed as a truly external source of excitation, delivering a quickly changing Coulomb field which excites predominantly the collective dipole oscillations [21]. One can then write the external potential for an ion with charge Q as

$$v_{\text{ext}}(\mathbf{r}, t) = -Qe^2 / \sqrt{(x - v_1 t)^2 + y^2 + (z - b)^2} . \quad (52)$$

When working in 2D with a CAPS ionic background, we average out the (time and space) odd contribution $v_1 t x$ and use the following approximate form for v_{ext} :

$$v_{\text{ext}}(\mathbf{r}, t) \simeq -Qe^2 / \sqrt{r^2 + (z - \sqrt{b^2 + (v_1 t)^2})^2} . \quad (53)$$

Note that the origin of the coordinate system is at the center of mass of the cluster. The clock is set to $t = 0$ at the time of closest approach ($x = b$, $z = 0$). The electromagnetic pulse (52) is essentially of dipolar nature because we consider small clusters with respect to the curvature of the ionic electric field. Note finally that the whole excitation process is comparable with Coulomb excitation as used very often in nuclear physics for probing the collective response of nuclei [157].

4.1.2. Instantaneous mechanisms

The interaction time of fast collisions ($v_1 \geq v_F$) stays below any other ionic or electronic time scale in a metal cluster. In a simplified but generic picture, this type of excitation can then be regarded as instantaneous. An efficient way of simulating such instantaneous excitations is to simply incorporate them into the initial condition and then propagate electrons freely in time. For instance, one can prepare the initial state by performing a rigid displacement of the ground-state orbitals $\varphi_j^{(\text{stat})}(\mathbf{r})$ with respect to the ionic background:

$$\varphi_j(\mathbf{r}, t_0) \equiv e^{i\mathbf{r}_{\text{shift}} \cdot \hat{\mathbf{p}}} \varphi_j^{(\text{stat})}(\mathbf{r}) = \varphi_j^{(\text{stat})}(\mathbf{r} + \mathbf{r}_{\text{shift}}) . \quad (54)$$

Analogously, one may first go over to momentum space, perform a translation by $\mathbf{p}_{\text{boost}}$ (which means that the electron cloud gets a finite initial velocity) and then transform back. This is equivalent to multiplication with a phase factor

$$\varphi_j(\mathbf{r}, t_0) \equiv e^{i\mathbf{p}_{\text{boost}} \cdot \mathbf{r}} \varphi_j^{(\text{stat})}(\mathbf{r}) . \quad (55)$$

Note that $\mathbf{p}_{\text{boost}}$ or $\mathbf{r}_{\text{shift}}$ have to be the same for all states φ_j to provide a proper collective excitation of the electron cloud. These mechanisms are not only easy to use; they also supply well defined initial conditions from which spectral properties can be directly deduced, see [18] and Section 4.2.1. Instantaneous excitation serves also for exploratory purposes in the regime of nonlinear excitations.

4.1.3. Lasers

Lasers are a universal tool and represent the most widely used experimental probe for clusters. Today, there exists a large variety of lasers operating in a wide range of wavelengths and intensities.

The “old” standard, one may say, has been set by continuous-wave or very long-pulse micro- (μs) or nanosecond (ns) lasers with low intensity and high spectral selectivity. These μs or ns lasers have been and still are the spectroscopist’s work horses for exploring the linear domain. Their main parameter of interest is their frequency ω_{laser} , and they have been widely used to study optical response [11]. But these lasers have also been applied to trigger steady electron emission for reaching high charge states as doorways for fission [149], for a review see [148] and references therein.

Over the last two decades, powerful femtosecond (fs) laser systems have become routinely available, and nowadays they are the method of choice for exploring ultrafast processes and the nonlinear regime in atomic, molecular and condensed matter physics as well as in chemistry. A particularly active field of research deals with multiphoton processes of atoms and small molecules irradiated with strong laser pulses (for reviews see [158–160]). In this context, “strong” refers to peak intensities I of the order 10^{13} – 10^{16} W/cm², which corresponds to electric field amplitudes E_0 of about 0.5 – $15V/a_0$. These numbers are comparable to the static electric fields experienced by an electron in its own atomic or molecular orbital, and obviously cannot be treated as small external perturbations.

While the theoretical and experimental investigation of multiphoton processes in atoms and small molecules has reached its maturity, the exploration of strong-field phenomena in clusters is still in a juvenile stage. Considering the wealth of new and surprising phenomena in atoms and molecules that have been uncovered by the use of strong femtosecond laser pulses, one can only imagine the huge variety of possibilities in the field of cluster science which are yet to be explored.

In dealing with these nonperturbative phenomena, the frequency ω_{laser} remains of course a key parameter. However, the peak intensity I , pulse length T_{pulse} , and temporal pulse profile become equally important characteristics of the actual excitation process. In general, the wavelength of the laser fields (near-ultraviolet to near-infrared) is much larger than typical cluster dimensions. We are thus allowed to work in the dipole approximation and parametrize the laser field as

$$v_{\text{ext}}(\mathbf{r}, t) = E_0 \hat{D}_i \cos(\omega_{\text{laser}} t) f(t), \quad (56)$$

where \hat{D}_i is the dipole operator in x -, y -, or z -direction, E_0 is the field strength, and $f(t)$ the temporal profile of the laser pulse. As a general rule, sharp profiles as, e.g., rectangular pulse shapes, are to be avoided, since a too abrupt switching on and off will induce unphysically large transient effects and subsequent spectral diffuseness. In the present investigations we limit ourselves to a few simple profiles, such as trapezoidal pulses that are turned on and off with a short linear ramp (during the first and final 5% of the total duration of the pulse) and held constant in between. Another example is the \cos^2 envelope which reads

$$f(t) = \begin{cases} \cos^2\left(\frac{t - T_{\text{pulse}}}{T_{\text{pulse}}} \frac{\pi}{2}\right) & \text{if } t \in [0, T_{\text{pulse}}], \\ 0 & \text{else.} \end{cases} \quad (57)$$

This signal is precisely zero at both ends and its full-width at half-maximum (FWHM) is T_{pulse} . The \cos^2 pulse can be considered a very good approximation to experimental pulse shapes, and it provides a good spectral selectivity. However, the whole process takes $2T_{\text{pulse}}$ for complete switching on and off, and the intensity is low during half of the time. On the other hand, the

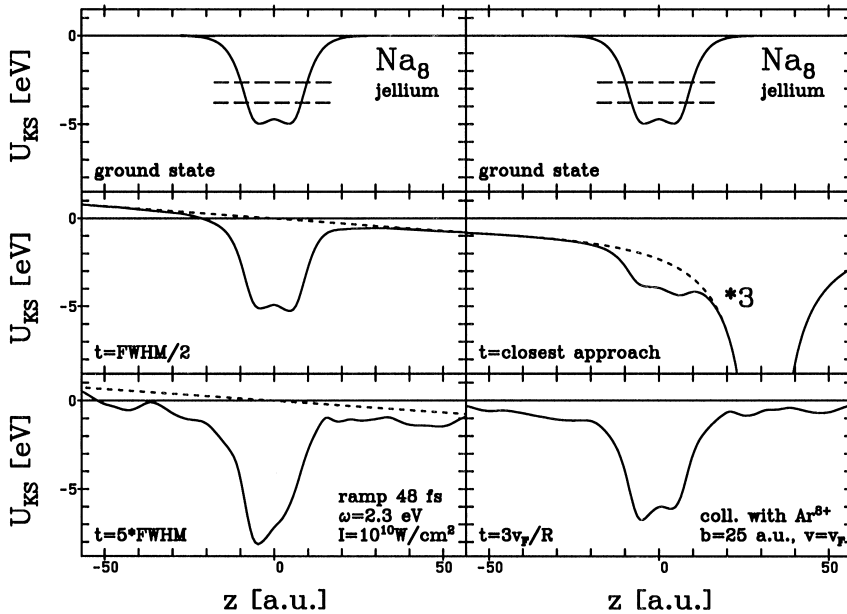


Fig. 3. The external potential (dashed lines) and the total (Kohn–Sham + external) potential (full lines) in Na_8 with soft jellium background for two different excitation processes, laser on resonance (left part) and collision with an Ar^{8+} ion passing by at impact parameter $b = 25a_0$ with velocity $v_1 = v_F$ (right part). Three typical times are shown in each case: the ground state before external fields become active (uppermost panels), an early stage for the laser case and the time of closest approach for the collision (middle panels), and a late stage where plasmon response of the system has shaken up the mean field (lower panels). The dashed lines in the uppermost panels indicate the energies of the occupied single electrons states. The note “*3” in the middle right panel indicates that this potential is to be rescaled by factor 3. The rescaling was needed to fit the enormous Coulomb well into the frame.

trapezoidal profile provides less spectral selectivity due to its more rapid switching, but it makes more efficient use of the pulse time, i.e. the pulse is at its maximum intensity during 90% of its total duration. It is thus more efficient for simple exploratory calculations. Both types are often used in the literature and will appear here in the results. We furthermore mention the Gaussian pulse shape which has also been used in several calculations. But this is a less efficient choice as one needs to allow for a longer switching time at both ends in order to guarantee sufficient suppression of the laser signal. In the end, however, variation of the pulse profile is presently not the most important issue. Our main goal is an overview of dependencies on frequency, intensity, and pulse length.

4.1.4. Schematic view of the processes

The different natures of the excitation processes by laser and ion collision are illustrated in Fig. 3. Each panel contains a snapshot of the instantaneous total Kohn–Sham potential (8) of the system (full line) as well as the external potential associated with the laser and the bypassing ion (dashed). The initial ground state situation is shown in the uppermost panel. This serves to set the scale in order to estimate the amount of perturbation induced by the excitation processes. The violent encounter between the ion and the cluster takes place within a few fs. We see that at the time of closest approach (middle right panel) the Kohn–Sham potential is completely dominated by the

Coulomb potential of the ion. The ion then passes by very quickly, leaving behind a cluster that is shaken up into a state of high excitation (lower right). By contrast, the laser-induced excitation proceeds much more gently (middle left panel), the cluster potential hardly gets distorted during the phase in which the pulse is turned on. After many periods of a steadily oscillating external potential, however, the electron cloud finds itself in a highly excited state as well, as can be seen from the irregularities in the Kohn–Sham potential (lower left). We thus conclude that both mechanisms fulfill the goal of creating a nonperturbative scenario which is suitable for studying nonlinear effects. The main difference lies in the time scales.

4.2. Observables

Let us now define the relevant observables for the phenomena we are interested in, namely electron emission and dipole response. In Section 2.2, we had presented the TDDFT approach to describe the electron dynamics of the system. It was established that all physical quantities of interest can be calculated as functionals of the time-dependent density. In practice it turns out that some observables may be obtained quite straightforwardly in that fashion, whereas others are very hard to express as *explicit* functionals of $n(\mathbf{r}, t)$. In the following, we shall deal with both cases.

4.2.1. Spectral analysis

The most important observable in relation to optical response is the dipole moment. For example, the dipole moment $D_z(t)$ of electrons with respect to ions, along the z -axis, is evaluated as

$$d(t) = \int_{\mathcal{V}} d^3r \, z n(\mathbf{r}, t) , \quad (58)$$

the origin of the frame being at the ionic center of mass. The integration volume \mathcal{V} has to be chosen with care. The outflow of emitted electrons can spoil the signal due to the large weights of large z . A robust and meaningful signal is obtained by confining the integration to an analyzing volume \mathcal{V} [18]. In practice, we add a stripe of $2r_s$ to the cluster radius R , thus considering a sphere of radius $R + 2r_s$, or a box with side length $2(R + 2r_s)$ (the actual geometry does not make much of a difference). The emerging signal then serves as raw material for the further analyzing steps. Spectral properties are related to the Fourier transform $\tilde{D}_z(\omega)$, yielding, e.g., the dipole power spectrum $\mathcal{P}_D(\omega) = |\tilde{D}_z(\omega)|^2$. The dipole strength can be evaluated following an instantaneous shift excitation (54) as $\mathcal{S}_D(\omega) \propto \Re\{\tilde{D}_z(\omega)\}$ or after an initial boost (55) as $\mathcal{S}_D(\omega) \propto \Im\{\tilde{D}_z(\omega)\}$ [18]. The strength function $\mathcal{S}_D(\omega)$ is a well suited observable for analyzing the optical response in the linear regime. It is directly related to the photoabsorption cross section $\sigma(\omega)$ measured in experiments [161,162]. However, the information delivered by $\mathcal{S}_D(\omega)$ loses its impact when one leaves the regime of linear excitations. In the nonlinear domain, the power spectrum $\mathcal{P}_D(\omega)$ becomes the preferred tool of investigation, which allows one to analyze in a robust way spectral patterns and trends [18].

This technique to evaluate the strength function for optical response from full TDLDA has been widely used in recent times, see e.g. [18,163]. It ought to be mentioned that technically less expensive approaches are possible if one is only interested in linear response properties. The most prominent example is the linearized TDLDA, which had been employed already in the first studies

of cluster dynamics [3,4] and in many subsequent investigations. There is, furthermore, a close link between linearized TDLDA and the random-phase approximation (RPA) which had also been widely used in cluster physics, for an overview see e.g. [107]. These explicitly linearized approaches are particularly efficient if symmetries are involved. Thus they have been used mostly in connection with the jellium model. Detailed ionic structures break any symmetry, and then a linearized TDLDA on a 3D grid becomes very cumbersome. In such cases, it is simpler to work with real-time full TDLDA, which provides an efficient, accurate and affordable alternative for detailed spectral analysis.

4.2.2. Ionization

We begin with the evaluation of electron escape, which relies on the basic relation

$$N(t) = \int_{\mathcal{V}} d^3r n(\mathbf{r}, t) , \quad (59)$$

associating the number of electrons remaining in bound states, $N(t)$, with the electronic density within the finite volume \mathcal{V} centered around the ionic background. From $N(t)$ one can then calculate the total number of escaped electrons as $N_{\text{esc}}(t) = N(t=0) - N(t)$. In fact, it turns out that $N(t)$ is not very sensitive to the actual choice of \mathcal{V} , in particular in the limit of large t (for more details see [164,165]).

An important link with experiment may be established by calculating probabilities $P^k(t)$ of finding the cluster at a time t in one of the possible charge states k to which it can ionize. The $P^k(t)$ are an example for the second class of observables mentioned above, which are very hard to write in terms of the total density. Instead, it is much easier to derive explicit approximate expressions for the $P^k(t)$ in terms of bound-state occupation probabilities $N_j(t)$ associated with the single-particle Kohn–Sham densities n_j ,

$$N_j(t) = \int_{\mathcal{V}} d^3r |\varphi_j(\mathbf{r}, t)|^2 = \int_{\mathcal{V}} d^3r n_j(\mathbf{r}, t) . \quad (60)$$

Since the single-particle Kohn–Sham orbitals have no rigorous physical meaning, one must consider the $P^k[\{n_j\}](t)$ obtained that way only as a reasonable approximation to the exact probabilities. To derive the expressions for the P^k 's, we start with the simple example of a system which at $t = 0$ has only one doubly occupied orbital, such as the helium atom [80,166] or a Na_2 cluster in a spherical jellium model. In this simple case, the $P^k(t)$ are, in fact, explicit functionals of the total density. If the bound-state occupation probability (60) for these systems is given by $N_{1s}(t)$, then the probabilities for the possible charge states are

$$P^0(t) = N_{1s}(t)^2 , \quad (61)$$

$$P^{+1}(t) = 2N_{1s}(t)(1 - N_{1s}(t)) , \quad (62)$$

$$P^{+2}(t) = (1 - N_{1s}(t))^2 . \quad (63)$$

These expressions have been constructed to fulfill the requirement that the probabilities must sum up to unity. The square in P^0 and P^{+2} and the factor of 2 in P^{+1} account for the degeneracy, as we work with a spin-unpolarized system.

In the general case, we start with the following relation:

$$1 = \sum_{k=0}^N P^k(t) = \prod_{j=1}^N [N_j(t) + (1 - N_j(t))]^2 \equiv \prod_{j=1}^N [N_j + \bar{N}_j]^2 . \quad (64)$$

We then work out the right-hand side of Eq. (64) and rearrange the resulting terms, collecting terms containing k factors $\bar{N}_j = (1 - N_j)$ and $(N - k)$ factors N_j . These are then identified with the ionization probabilities $P^k(t)$ [81]. A more detailed derivation and a discussion of the range of validity of the $P^k(t)$ is given in [167]. It is interesting to note that this strategy to derive ionization probabilities from a combinatorial identification has been used before in a somewhat different context, namely within stationary scattering theory [168].

The emitted electrons are often analyzed in more detail. This is done extensively in atomic physics in the context of above-threshold ionization [158–160]. There are also several cluster experiments which resolve the kinetic-energy spectrum (KES) of the emitted electrons, e.g. [169,5,170,171]. We will also briefly discuss theoretical results for the KES in multi-photon processes, see Section 7.4. The derivation of the KES from the TDLDA(-SIC) calculations proceeds as follows. We compute the local frequency spectrum of the electronic wavefunctions at a measuring point near the boundaries of the grid. We thus record the single-electron wavefunctions $\varphi_i(\mathbf{r}_{\text{bc}}, t)$ over time at the measuring point \mathbf{r}_{bc} . Then we Fourier transform them into the frequency domain ($\varphi_i(\mathbf{r}_{\text{bc}}, t) \rightarrow \tilde{\varphi}_i(\mathbf{r}_{\text{bc}}, \omega)$). Note that the measuring point \mathbf{r}_{bc} near the (absorbing) boundary is far off the interaction zone. Moreover, the absorbing boundary conditions [18] guarantee that only outgoing waves are passing by \mathbf{r}_{bc} . The frequency spectrum $|\tilde{\varphi}_i(\mathbf{r}_{\text{bc}}, \omega)|^2$ is thus also the KES of electrons emitted from state i . Altogether the total KES of the N electrons becomes

$$n(E_{\text{kin}}) = \sum_{i=1}^N |\tilde{\varphi}_i(\mathbf{r}_{\text{bc}}, E_{\text{kin}})|^2 . \quad (65)$$

From a formal point of view, it is worth noting that: (i) definition (65) is robust under unitary transformations amongst the occupied single-electron states; (ii) the actual spectra will take the energy of the highest occupied electron (HOMO) level as ionization energy. SIC (even in an approximate manner, see Section 2.3.2) delivers here the correct value.

4.2.3. Energies

Having explicit electronic orbitals, densities and currents at hand, it is possible and very informative to analyze the different forms in which energy is deposited, stored or lost during the processes under study. A lot of information about the nature of the excitation processes can be gained by monitoring how the distribution of the total energy into different components changes over time.

The plasmon oscillations are a collective phenomenon closely related to the total electron flow. The energetic aspect of collective electronic flow is essentially summarized in the hydrodynamic collective kinetic energy

$$E_{\text{coll,kin}}(t) = \int d^3r \frac{\mathbf{j}^2(\mathbf{r}, t)}{2n(\mathbf{r}, t)} . \quad (66)$$

The counterpart is the intrinsic (or thermal) excitation energy of the electrons. We define it as

$$E_{\text{int}}(t) = E_{\text{kin}}(t) - E_{\text{TFW}}(t) - E_{\text{coll,kin}}(t) , \quad (67)$$

where $E_{\text{kin}}(t) = \frac{1}{2} \sum_j \int d^3r |\nabla \varphi_j(\mathbf{r}, t)|^2$ is the total Kohn–Sham kinetic energy of the electron cloud. The next term, $E_{\text{TFW}}(t) = \int d^3r \tau_{\text{TFW}}(t)$, subtracts the instantaneous (adiabatic) kinetic energy of the zero-temperature ground state at the given density $n(\mathbf{r}, t)$. It is computed in Thomas–Fermi–Weizsäcker approximation, $\tau_{\text{TFW}} = 0.6(3\pi^2)^{2/3} n^{5/3} + (\nabla n)^2/(18n)$, which provides a very efficient and reliable estimate [31]. The relative intrinsic energy E_{int} is thus measuring the nonadiabatic and non-collective component of the kinetic energy.

The energy pumped into the system by the excitation mechanism and absorbed by the electron cloud can furthermore be determined as

$$E_{\text{abs}}(t) = \int_{t_0}^t dt' \int d^3r n(\mathbf{r}, t') \frac{d}{dt'} v_{\text{ext}}(\mathbf{r}, t') , \quad (68)$$

which provides an estimate of the ionic temperature that may be reached by the excited cluster. Finally, we have the straightforward (classical) kinetic energy of the ions

$$E_{\text{ion,kin}}(t) = \sum_I \frac{M_I}{2} \dot{R}_I^2 . \quad (69)$$

5. Spectral properties in the linear regime

Before proceeding to the appealing regime of nonlinear effects, one first needs some insight into the basic nature of the systems. This is achieved by studying the simpler and well-controlled regime of linear response. We therefore start with a section that summarizes the basic results within the linear regime. The main emphasis is here on spectral properties and their relation to the underlying structures. The spectra show the regions of strong or weak coupling to external perturbations and thus define the doorway for the nonlinear processes studied later on.

TDLDA driven in the regime of small amplitudes constitutes the basic theoretical approach here. The conceptually simplest choice is indeed to use a given TDLDA code for solving the time-dependent Kohn–Sham equations and to apply spectral analysis as described in Section 4.2.1. Small amplitudes, however, allow one to derive formally a linearized TDLDA which requires more laborious coding but is then much more efficient, particularly in cases of restricted symmetries. The first studies in the linear response regime have thus been performed with linearized TDLDA and the jellium model [3,4,172], an approach which has been used very often since then [5,6]. The more demanding present applications (ionic structure, no symmetries) and increasing computer power are now moving the bias towards the conceptually simpler but numerically more demanding full TDLDA calculations. In the following, we will review examples from both methods.

5.1. Typical spectra

5.1.1. Free sodium clusters

A simple and yet sufficiently rich test case is Na_9^+ . Its ground state is well described in CAPS [50,51]. It has a 144 structure: one ion on top, followed by a ring of four ions and another ring of

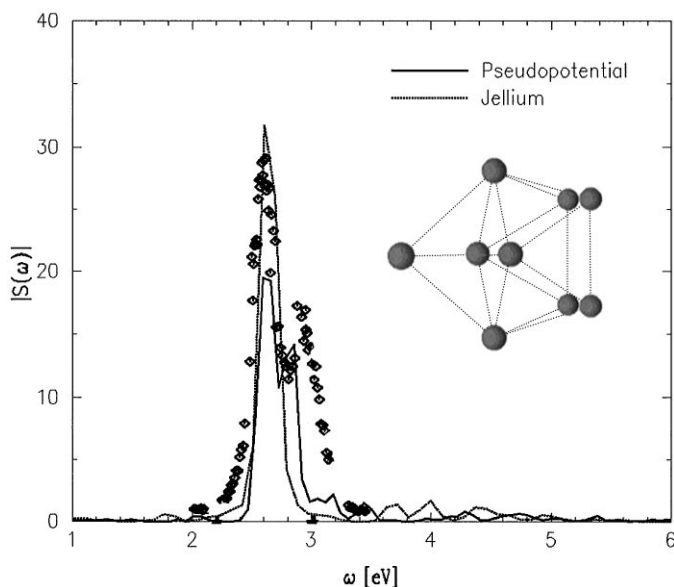


Fig. 4. Full 3D TDLDA calculation of the optical response of Na_9^+ with explicit ionic background (144 configuration, as shown in the inset), compared to experimental data (diamonds) measured at 35 K. Figure from [173], data from courtesy of H. Haberland.

four ions (which is rotated by 45° to minimize the ionic Coulomb energy). The overall shape is close to spherical, but has a small octupole moment due to reflection-symmetry breaking by the top ion. A good zeroth-order description is thus already obtained by the spherical jellium model. Fig. 4 shows the dipole spectra obtained from TDLDA with jellium background and full ionic structure [57] in comparison with experimental results [173]. The spectra coincide very nicely in their main features, namely the pronounced Mie plasmon resonance around $\omega \sim 2.7 \text{ eV}$. The jellium model provides a pertinent description of the overall resonance position. It fails, however, to reproduce the fragmentation of the resonance in two sub-peaks as seen in experiment. The TDLDA calculation with full ionic structure, on the other hand, delivers this splitting, as seen from Fig. 4. Closer inspection shows that the latter is due to an interference of one isolated particle–hole (1ph) state with the resonance. The symmetry breaking through explicit ionic structure induces the coupling to this 1ph state [57], which is not possible in the highly symmetric spherical jellium picture. This example demonstrates that simple approximations such as TDLDA + jellium are very useful to provide a first overview of spectral patterns, and that detailed ionic information is only needed if one aims at finer structures. This latter aspect is in fact meaningful only in the domain of very gentle perturbations. Note for example that experiments are able to resolve spectral details only at very low temperatures of at most a few tens of K [173]. Similarly, ionic effects play a minor role in the details of the electronic response as soon as one leaves the linear regime of faint electronic excitations [16].

Dipole excitation dominates by far in metal clusters. Nonetheless, it is worthwhile to investigate other modes as, e.g., spin excitations [175]. These are particularly interesting for soft Na clusters where a competition between Jahn–Teller deformation and Hund’s rule makes spontaneously

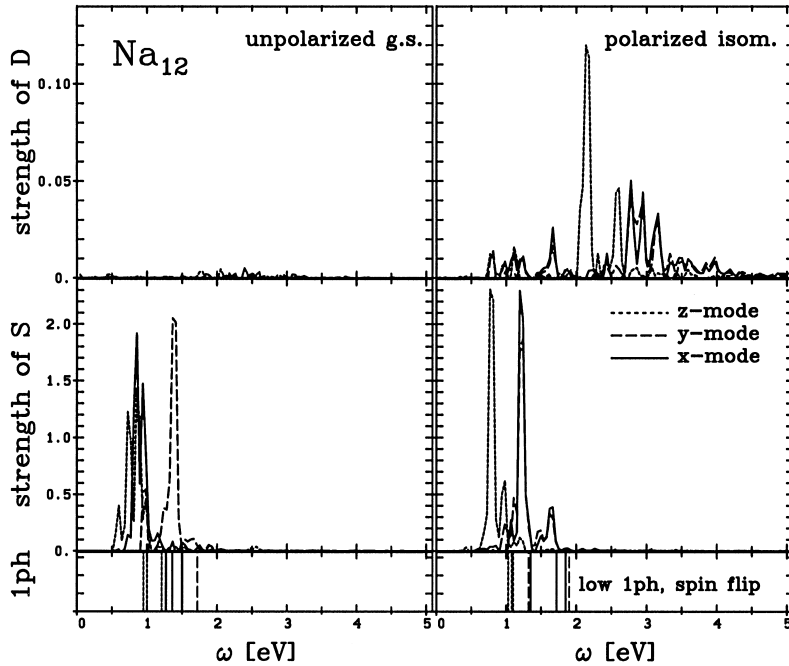


Fig. 5. Spectral strength distributions for the dipole signal (upper panels) and the spin-dipole signal (middle panels) after initialization with a spin-dipole shift. The left part shows results from the triaxial ground state of Na_{12} and the right part from the polarized isomer, both optimized with detailed ionic structure. In the lowest panel the energies of the corresponding 1ph transitions between levels with opposite spins are plotted. The assignment of line types is: x-mode = full line, y-mode = dotted, and z-mode = dashed. From [174].

polarized isomers very likely [176,177]. Fig. 5 shows the spin-dipole and dipole spectra from instantaneous spin-dipole excitations of Na_{12} in the unpolarized, triaxial ground state and in the polarized, axially symmetric first isomer [174]. The spin-dipole excitation of the system is performed by displacing the spin-up electron cloud with respect to the spin-down one at initial time. The amplitude of the shift (here $0.8a_0$) fixes the deposited excitation energy. The response of the system is then measured in terms of the spin dipole $S_z(t) = 1/N_{\uparrow} \sum_{j\uparrow} \langle \varphi_{j\uparrow} | z | \varphi_{j\uparrow} \rangle - 1/N_{\downarrow} \sum_{j\downarrow} \langle \varphi_{j\downarrow} | z | \varphi_{j\downarrow} \rangle$. The spin modes as such are much lower in energy than the dipole resonance. They are found close to the low-lying 1ph states and are somewhat shifted by a weak (exchange) residual interaction. Fig. 5 shows that there is no cross-talk between dipole and spin-dipole modes for an unpolarized state (left panels). The spin-dipole mode looks quite similar for the polarized isomer (right panels), but we now see a strong cross-talk with the dipole mode. The dipole mode is again dominated by the Mie resonance. There are in addition several higher lying 1ph states (highest panel) which gather their share of dipole strength, and there is a visible dipole co-vibration in the low-lying regime of spin-dipole modes. Altogether, a simultaneous measurement of dipole and spin-dipole spectra would thus provide enormously useful extra information. Inelastic light (Raman) scattering is a method to measure spin modes in solids [178] and may be considered for that purpose in clusters too. Virtual photons from electron scattering

Table 1

Principal deformation in Hill–Wheeler coordinates β, γ and normalized moments of inertia I_x, I_y, I_z for planar ground state and 3D isomer of Na_8 deposited on NaCl. The difference in binding energy per particle to the planar ground state (GS) is given in eV

	$\Delta E/N$	β_2	γ	Na_8 I_x	I_y	I_z	β_3
GS	—	0.86	15.28°	0.35	1.15	1.50	0
First isomer	0.007	0.07	0.5°	1.02	0.85	1.13	0.24

experiments are another alternative, and here there exist first attempts for clusters which, however, are still fighting with technical problems [179,180].

5.1.2. The case of deposited clusters

We have seen that the dipole mode remains the best accessible and thus most fruitful excitation in metal clusters. And it even contains much more information than we discussed in our first test case Na_9^+ . Dipole spectra can be viewed as fingerprints of the shape of the underlying ground states. This is best demonstrated with deposited clusters, which naturally exhibit strong deformations. We consider here the case of Na_8 on an insulator (NaCl) substrate. The strong interface potential generated by the surface produces a planar ground state where all Na^+ ions of the cluster are sitting directly on the interface (and close to the Cl^- surface ions). But in the special case of a magic number of electrons, the spherical shape favored for the free cluster is able to compete energetically with the flattening effect of the surface. It thus turns out that a “three-dimensional” (3D) isomer exists, which basically represents free Na_8 deposited on the surface [56]. The planar ground state has strong triaxial quadrupole deformations, whereas the 3D isomer remembers the near spherical shape of the free ground state, although it develops a substantial octupole deformation from the attraction of one side to the interface. The deformation parameters in terms of Hill–Wheeler coordinates [181,56] and the corresponding moments of inertia are given in Table 1 and provide a global account of the shapes of the deposited clusters. A graphical illustration of the ground-state shapes can furthermore be found in the upper panels of Fig. 6. The corresponding dipole strengths are shown in the lower panels of Fig. 6. The strongly quadrupole deformed planar ground state (left panels) produces three different Mie resonances, one for each principal axis in x -, y -, and z -direction. The cluster has its largest extension along the x -axis, and correspondingly the resonance frequency is lowest. By contrast, the extremely short extension in z -direction (one layer) produces the highest frequency. This is the well-known splitting of the Mie resonance through quadrupole deformation which had already been discussed in the earliest stages of cluster research [172]. We shall come back to this point in a more systematic way in Section 5.2.4. Note finally that besides this clear deformation splitting, each resonance shows a well developed concentration of strength (Fig. 6).

The situation is quite different for the 3D isomer. The spectra in all three directions occupy the same frequency region, and each one is strongly fragmented. The small quadrupole deformation explains the lack of collective splitting, while the octupole deformation gives rise to a strong

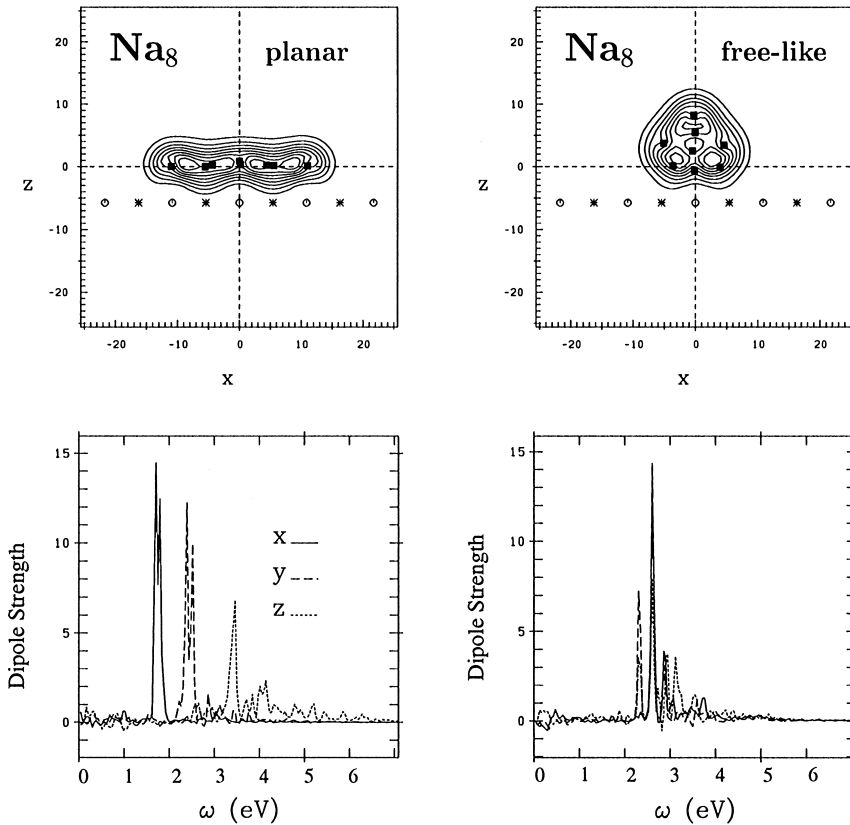


Fig. 6. Upper panels: contour plots of the electronic density in the x - z plane for the planar ground state (left) and the free-like isomer (right) of Na_8 adsorbed on $\text{NaCl}(100)$. The projection of cluster ions are indicated by *squares* and the first monolayer of the $\text{NaCl}(100)$ substrate is labeled by *circles* (Cl^-) and *stars* (Na^+). Lower panels: spectral dipole strength distributions for modes in x -, y -, and z -direction. From [182].

Landau fragmentation of the spectra [183]. The mechanism is a particular feature of small metal clusters. The plasmon resonance for small clusters resides in a spectral gap of 1ph states if the ionic background is symmetric under reflection [107]. Symmetry breaking, however, gives access to a group of 1ph states around the resonance and this, in turn, leads to the strong fragmentation of dipole strength. It is the interface interaction in the example of the 3D isomer which produces the large octupole deformation. A similar symmetry breaking is observed in the case of free clusters due to shape fluctuations caused by thermal ionic motion. The octupole component of these shape fluctuations then induces Landau fragmentation through (thermal) symmetry breaking. This was found to yield the leading contribution to the width of the plasmon resonance in small clusters [183]. It ought to be mentioned, however, that collective level splitting due to the quadrupole part of the shape fluctuations also adds a substantial contribution to the width and was, in fact, first investigated as broadening mechanism in [184,74,185]. The more detailed analysis of [183] finds that about $\frac{1}{3}$ of the linewidth arises from the quadrupole and $\frac{2}{3}$ from the octupole deformations.

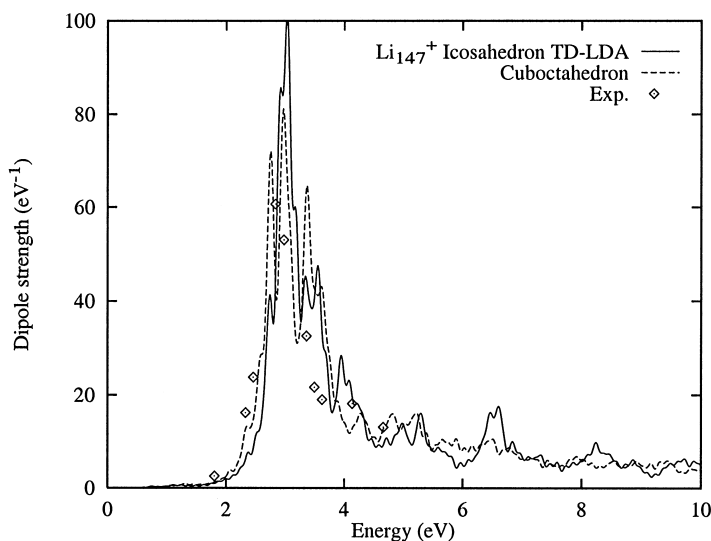


Fig. 7. Dipole strength for Li_{147}^+ . The experimental points are from [189]. The TDLDA has been computed for two different assumptions about the geometry of the ionic background as indicated, taken from [17].

5.1.3. Beyond simple metal clusters

Sodium clusters are particularly friendly systems because they can be treated with local pseudopotentials [186,99,58]. This, in turn, often permits using symmetry restricted approaches such as CAPS or even a simple treatment within the jellium model. Most other metals are less forgiving. They require nonlocal pseudopotentials which make fully fledged three-dimensional TDLDA calculations mandatory [17,187,188]. In spite of this, the enormous success of computational techniques allows one nowadays to attack surprisingly large systems. An example is provided by recent calculations for Li_{147}^+ , see the results shown in Fig. 7. The most costly part, the optimization of ionic structure, has been bypassed here by assuming that the large cluster just consists of a piece of a bulk crystal. Two assumptions for the ionic structure are explored in Fig. 7 and compared with experimental data. Both produce very similar spectra which agree nicely with the experimental strength distribution. There are, of course, differences in detail, but these are in any case beyond the expected precision of the method. We thus see again that the main features of the dipole spectra (position, collective splitting, fragmentation width) are essentially determined by the gross structure of the cluster in terms of radius and deformations. The main effect from a detailed ionic treatment enters through the correct handling of the nonlocality of the pseudopotential, which adjusts the overall resonance position immediately at the right place. The result suggests that simpler approaches may be possible for exploratory purposes. Such methods have indeed been worked out, leading to the concept of a pseudo-Hamiltonian which aims at incorporating the nonlocality of the pseudopotential in an average manner [190].

Once a fully three-dimensional TDLDA technique with nonlocal pseudopotentials is available, the door is open to study any material. As an example, we show in Fig. 8 the TDLDA dipole spectrum for benzene [163]. The agreement with the experimental data is very satisfying. The TDLDA results show somewhat more structure than experiments at high frequencies. But

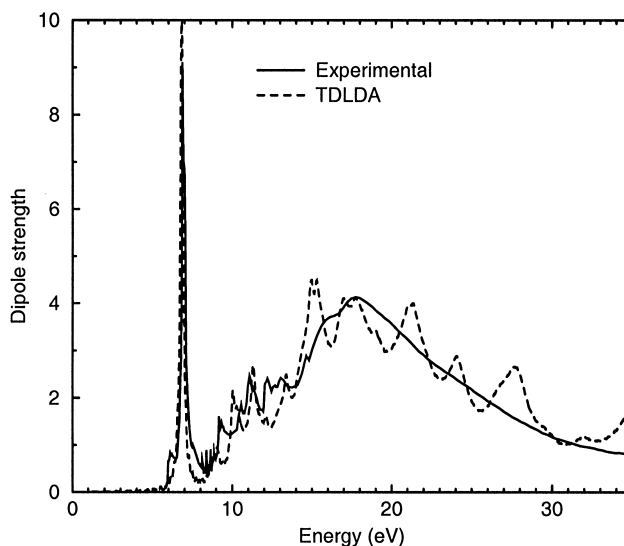


Fig. 8. Dipole strength for the organic molecule C_6H_6 . The experimental curve is from [191] and the TDLDA results, computed with explicit ionic configuration. From [163].

these can be expected to be wiped out by thermal motion and correlation effects. However, the average trends perfectly agree with the data. Carbon molecules are harder to handle because they require at least four electrons per ion. But they are worth the effort as they offer a huge variety of test cases, last not least the famous C_{60} cluster. Full TDLDA calculations for C_{60} are still not quite within reach for present computing capacities. But smaller clusters supply for a while enough unexplored testing ground, as e.g. carbon chains [95,98]. Alternatively, one may recur to less expensive methods as, e.g., time-dependent LCAO [192,193], which even allow one to compute a full ionic dynamics in C_{60} but are restricted to bound electrons only.

An even more involved situation arises for noble metals as, e.g., Ag. Here a d-band comes close to the valence s-band. A detailed treatment thus needs to deal with 11 electrons per ion, 10 in the d-state and the last one in the s-state. Such a treatment with appropriate (nonlocal) pseudopotentials is able to correctly reproduce the plasmon position of Ag clusters [187]. This becomes, of course, enormously expensive and hinders calculations of larger Ag clusters. A simplification is to treat the d-electrons merely by their localized dielectric response. This reduces the expense to one electron per ion and also cooperates nicely with the jellium model [59]. This latter approach, however, is confined to the linear regime. Violent excitations will very likely delocalize the d-states and produce a substantial charge mobility. These processes then require dealing with all 11 electrons per ion.

5.2. Trends

We have seen in the previous subsection that the dipole strength distribution of metal clusters is dominated by the Mie plasmon collective resonance [24,6,8,9]. Resonance position and width thus smoothly depend on the global system parameters such as size or deformation. It is worthwhile to

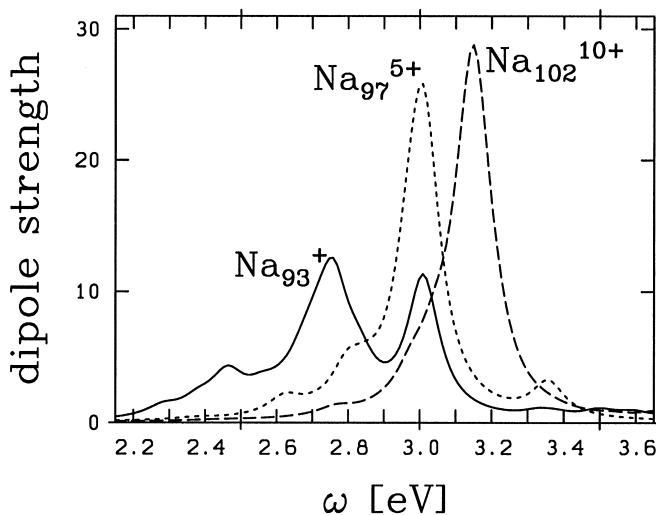


Fig. 9. Dipole strength distributions for a sequence of clusters with $N_{e1} = 92$ and different net charges as indicated. The ionic background was described in the soft jellium model.

know these trends because this allows a quick first estimate of the dynamical response for a given system. We sketch here briefly a few of the important trends. An extensive analysis of trends and spectral relations can be found in [107].

5.2.1. Role of the cluster charge

In the course of violent excitations clusters may lose a sizable fraction of the electron cloud and thus become highly ionized. However, one has to bear in mind that ionic motion is very slow on the electronic time scales. Thus, even if the ultimate fate of the cluster is to explode, electronic response will occur in the (metastable) highly charged system, and may even interfere with the (ionic) explosion patterns (see Section 7.7). It is thus of interest to study the effect of net charge on the plasmon response. Fig. 9 shows the dipole strengths for a Na cluster with fixed magic number of electrons $N_{e1} = 92$, but systematically varied background charge. The calculations used the soft jellium model and a linearized TDLDA with techniques as outlined in [107]. Two dominant features set the trend: the average resonance position moves to higher frequencies with increasing net charge, while the fragmentation width shrinks. Both effects can be understood from the changes in the Kohn–Sham potential. The larger net charge provides deeper binding. This confines the plasmon oscillations to a smaller area which, in turn, enhances its frequency. It turns out that the deeper potential also comes closer to the shape of an harmonic oscillator and one thus approaches the situation of Kohn’s theorem [194,195]. The latter states that a many-electron system in a purely harmonic external potential may sustain one unique plasmon mode which entirely exhausts the dipole sum rule. This explains the steady reduction of the fragmentation width.

5.2.2. Dependence on cluster size

Probably most important are the trends with system size. Fig. 10 shows the average resonance position (upper panel) and fragmentation width (lower panel) for a series of Na clusters in a wide

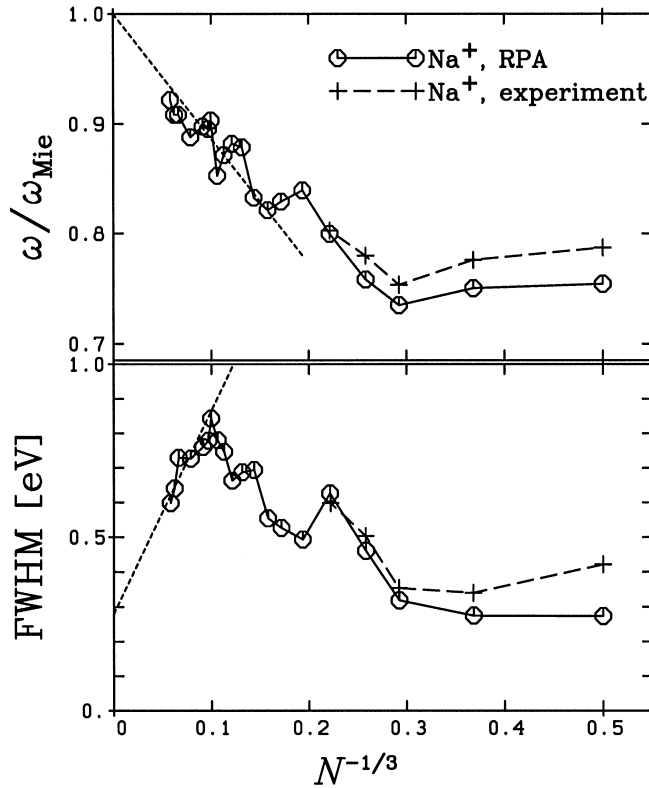


Fig. 10. Key spectral features deduced from dipole strength distributions $\mathcal{S}_D(\omega)$. Upper part: plasmon peak positions in units of $\omega_{\text{Mie}} = 3.45 \text{ eV}$ versus $N^{-1/3}$ for the experimental peaks and the peaks evaluated from separable RPA for charged clusters (soft jellium model). The dotted lines show the slope fitted to the finite surface calculations. Lower part: full-width at half-maximum (FWHM) versus $N^{-1/3}$ for the two cases as above, evaluated at the flanks of the strength distribution. The dotted lines show the asymptotic linear trends as fitted through the results for large samples in case of charged clusters (soft jellium model). From [196].

range of electron numbers N . The spherical jellium model with soft surface profile was used for the ionic background. The spectra have been computed in a separable approach to linearized TDLDA, which allows one to proceed to these huge system sizes [196] (comparable studies for large Na clusters can also be found in [197,37]). The average resonance frequency and fragmentation width have been obtained by smoothing the detailed spectral pattern and taking the emerging unique resonance peak and its full-width at half-maximum (FWHM). In the upper part of Fig. 10 the actual resonance frequency is compared with the Mie frequency $\omega_{\text{Mie}} = 3.4 \text{ eV}$ which characterizes the classical dipole surface excitation of a large metal sphere [24]. Finite clusters should have a smaller frequency $\propto \omega_{\text{Mie}}(1 - cN^{-1/3})$. An analytical expression for the slope c can be derived from the wall formula [75]. This global trend is indicated by the straight dotted line in Fig. 10 (upper panel). One sees that the larger clusters, from about $N = 500$ on, line up nicely around this asymptote, oscillating a bit around it, due to shell effects. But the frequency levels off for small clusters due to quantum effects. There is a minimal quantum gap of 1ph excitation which grows towards small clusters as $N^{-1/3}$. This sets a lower level of excitation energy to which the repulsive

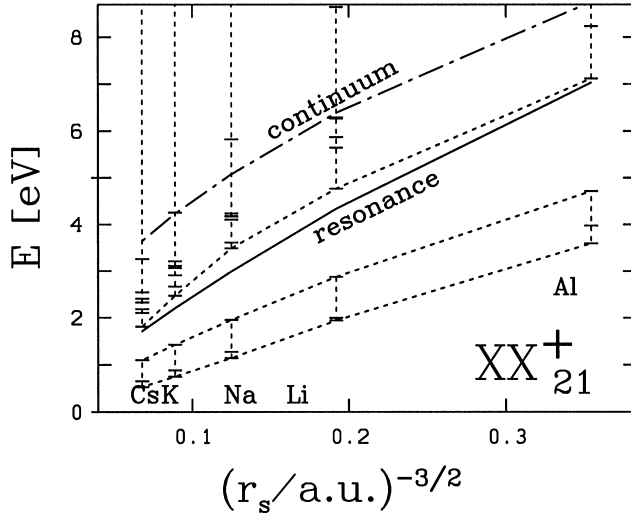


Fig. 11. Trend of key spectral features with Wigner–Seitz radius r_s for a fictitious cluster with $N = 20$ and $N_{\text{ion}} = 21$ using the soft jellium model for the ionic background [107]. The heavy line shows the average position of the Mie plasmon resonance, the dash–dotted line the diabatic ionization energy (i.e. the “continuum” threshold), the horizontal bars indicate 1ph states, and the faint dotted lines serve to mark the bands of 1ph states. The chemical symbols at the bottom indicate several simple metals associated with the corresponding r_s .

Coulomb residual interaction adds another substantial portion. Both effects together lead to the leveling off for the plasmon energy at small cluster sizes (and even some increase for very small clusters).

The lower panel of Fig. 10 shows the corresponding fragmentation width. Again the analytical estimate $\propto a + bN^{-1/3}$ from [75] is indicated as a dotted line. The offset of about 0.3 eV (large $N^{-1/3}$) comes from the smoothing of the spectra which was tuned in such a way that it resembles the thermal broadening at about $T = 400$ K. The asymptotic trend of the width is established only for large systems with $N_{\text{el}} \geq 1000$. The width then grows with $N^{-1/3}$, because smaller systems produce more collisions with the surface, which induces an increased coupling of the resonance to the 1ph states. For even smaller values of N the width turns over and decreases with growing $N^{-1/3}$. This is again due to quantum shell effects taking over, which reduces the density of 1ph states near the resonance frequency. For both observables (average peak position and width), we thus find that the asymptotic trend ($N \rightarrow \infty$) settles only for very large clusters and that smaller systems (below about 1000 particles) still explore all finite size and quantum effects. This coincides with similar findings about the semiclassical limit in nuclear physics [198]. The measurements, when available, nicely follow the trends of the microscopic calculations. But they go by no means far enough to truly explore the regime of the asymptotic trends $\propto N^{-1/3}$. Here still exists unexplored territory for studies in the linear regime.

5.2.3. Changing material

The key parameter in the jellium model is the Wigner–Seitz radius r_s . Fig. 11 shows the basic spectral properties (position of Mie resonance, bands of 1ph states, continuum threshold) for

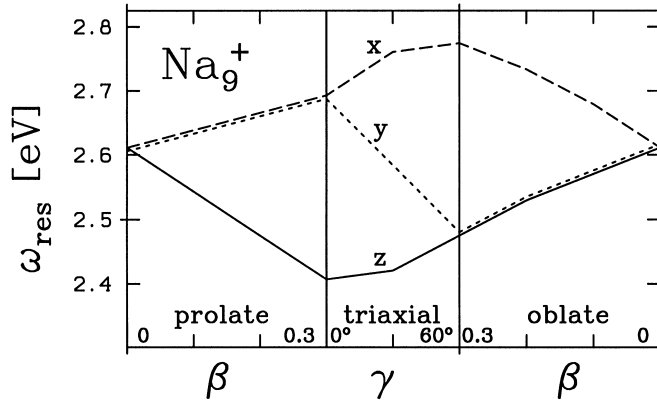


Fig. 12. Trends of the Mie plasmon resonance in x-, y-, and z-direction with deformation computed in a triaxial soft jellium model [199]. The first block shows the evolution with increasing deformation for an axially symmetric prolate system. The second block shows the trends when the triaxiality angle γ is cranked through 0–60° at fixed overall deformation $\beta = 0.3$. And the third block shows again an axially symmetric, but now oblate, system for a deformation which decreases from 0.3 back to 0.

a positively charged cluster with $N_{\text{el}} = 20$ and jellium background as a function of r_s . This is a compact way to compare various materials, as indicated in the figure. Note that in a dynamical context, increasing r_s also corresponds to the jellium picture of the explosion of a highly charged cluster (see Section 7.7). One sees that all the plotted properties follow approximately the same trend, so that the relations among them are almost independent of the material at the level of the jellium model. This behavior may be called jellium scaling [107]. It is interesting to note that in the small clusters considered here (21 ions) the more realistic picture is that the Mie resonance comes already close to the upper 1ph band so that the dipole spectra will show a small fragmentation of the resonance strength. Drawing such spectral relations versus system size shows that the resonance crosses the boundary of the upper 1ph band with further increasing electron number, shortly before $N = 40$ [107]. From then on sizeable Landau fragmentation can be seen already for spherical clusters (see also the lower panel of Fig. 10, where the width rises steeply starting from $N_{\text{el}} = 40$, i.e. $N^{-1/3} = 0.28$).

5.2.4. Deformation effects

The example of Na_8 on a NaCl substrate in Section 5.1.2 has indicated that there is a close relation between the splitting of the collective resonance modes and the underlying quadrupole deformation of the cluster. Fig. 12 shows the resonance positions of the x-, y- and z-mode as a function of deformation for Na_9^+ in the soft jellium model [199]. The labeling is done again in terms of the Hill–Wheeler coordinates for quadrupole deformations [181,199]. The deformation path starts along axially symmetric, prolate shapes. It then moves at fixed global deformation β through all triaxiality angles γ until an axially symmetric oblate shape is reached. From there on one goes with decreasing deformation back to the spherical starting point. One clearly sees that the prolate deformation induces a splitting into two peaks whose separation grows linearly with deformation β . The higher frequency corresponds to the shorter axis where two modes are

degenerate due to axial symmetry. The situation is similar for oblate shapes, but here the lower frequency is doubly degenerate. Finally, the fully triaxial shapes lift all degeneracies and produce a splitting into three distinct peaks. The trends are all very close to linear, and one can parametrize them simply as

$$\begin{aligned}\omega_x &= \omega_0[1 - 0.15\beta \cos \gamma] , \\ \omega_y &= \omega_0[1 + 0.15\beta(\cos \gamma - \sqrt{3} \sin \gamma)] , \\ \omega_z &= \omega_0[1 - 0.15\beta(\cos \gamma + \sqrt{3} \sin \gamma)] .\end{aligned}\tag{70}$$

This trend has been used as a crucial input in an estimate of the resonance width due to thermal shape fluctuations [183–185,200]. The splitting is a key signal from which the underlying cluster deformation can be inferred. This technique has been well established in the field [172,5,6,201,202].

6. Energetic ion collisions

6.1. The excitation process as such

We now proceed into the regime of nonlinear excitations, and as a first case we consider collision with fast and highly charged projectiles. An example of a collision between a proton of energy 10 keV (velocity $v_1 = 26a_0/\text{fs}$) and a Na_9^+ cluster is presented in Fig. 13. The calculation has been performed at Vlasov level, and the figure shows snapshots of the electron density at different instants of the collision. Note how fast the excitation proceeds and how the electron cloud is deformed and partly dragged along (at least temporarily) by the proton.

More generally speaking, for velocities in the Fermi velocity range ($v_1 \sim v_F$) the ionic projectile delivers to the cluster a quasi-instantaneous electromagnetic pulse, as discussed earlier in Section 4.1. The response of the cluster directly reflects the excitation mechanism. Of course, the early response is primarily of purely electronic nature, in view of the involved time scales. The electron cloud experiences a strong dipole excitation, which soon relaxes towards a steady collective oscillation of Mie plasmon type, hand in hand with almost instantaneous electron emission.

The origin of the electron emission deserves some comments. In the (usual) case of a positively charged projectile, two effects act together to ionize the cluster: the strongly shaken electron cloud relaxes a sizable fraction of its energy by emitting energetic electrons, and the positive ion itself tries to bind electrons. At smaller ionic velocities [91], direct charge transfer to the ion indeed plays a role. But at higher velocities, we find that the transferred electrons do not very well attach to the ion [156], probably due to lack of time for proper arrangement. At least they do not fall into low-lying states of the projectile. It is possible, though, that they attach as loosely bound states (even Rydberg states), but this is hard to ascertain with a high degree of confidence from the present TDLDA formalism. It is to be noted, however, that not all calculations agree on this conclusion [72]. But the results concerning capture depend on the details of the parameterization of the ionic potential and when similar definitions of trapping are used, similar results are obtained. Differences hence mainly lie at the level of interpretation of how one defines trapping. There is a general agreement that electron trapping by the ionic potential plays an important role, as can be verified

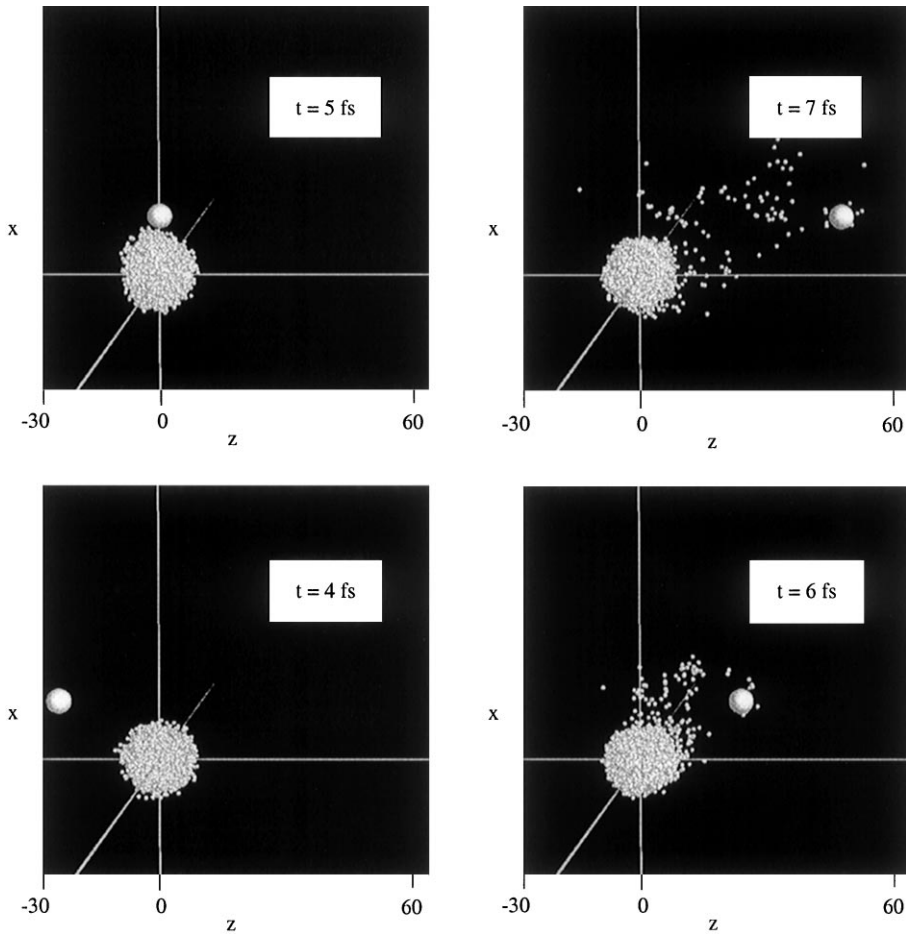


Fig. 13. Snapshots (in the x - z plane with a parallel perspective along y , all lengths measured in a_0) of a proton- Na_9^+ collision. The initial kinetic energy of the proton is $E_p = 10 \text{ keV}$ and its impact parameter is $b = 15a_0$. White spheres denote the centroids of the Gaussians on which the Wigner distribution is projected. The actual distribution is smoothed by the Gaussian form factor of the numerical test particles. The proton is represented by a larger sphere. The instant of closest approach corresponds to $t = 5 \text{ fs}$. After data from [21].

by considering the case of a negatively charged projectile, for which ionization is indeed strongly suppressed [19]. This pending question warrants yet deeper investigation. In any case, the state of the cluster at the “end” of the pulse is relatively well defined. The cluster is (possibly strongly) ionized and sustains a collective oscillation of the electron cloud. Furthermore, those electrons which do not acquire enough energy to leave the cluster actually store a sizable excitation energy (beside the relatively small collective component associated with the Mie plasmon).

6.2. Basic properties of collisional excitation

The following brief description of the reaction mechanism emphasizes the key variables to be considered for describing the physical situation: dipole moment, ionization and deposited energy.

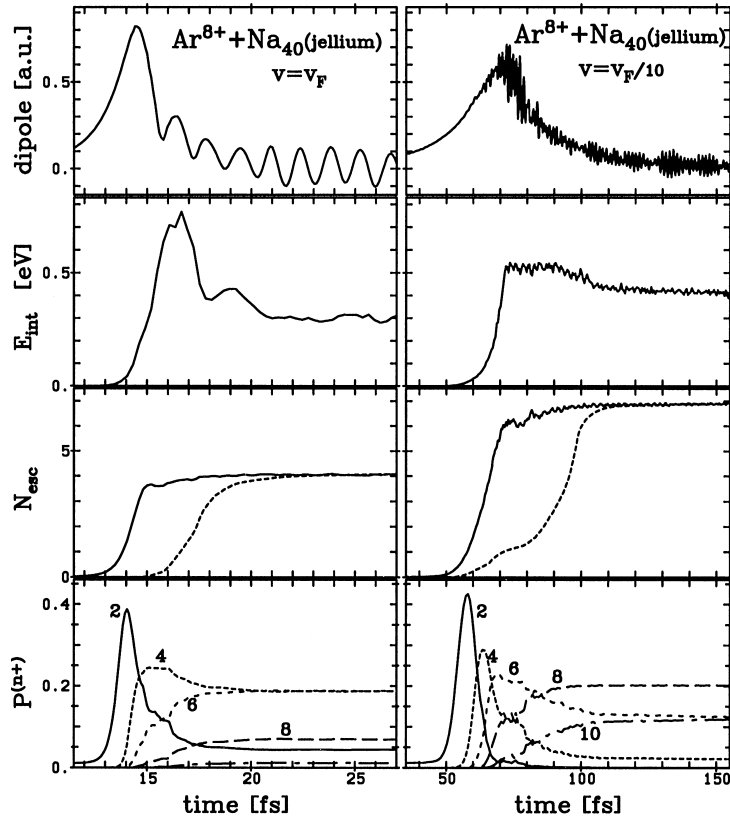


Fig. 14. Time evolution of basic observables for a collision of Ar^{8+} with a Na_{40} cluster described in the soft jellium model. The left part shows a fast collision at ionic velocity $v = v_F$ and the right part a slower case at $v = 0.1v_F$. The impact parameter is $b = 26a_0$ in both cases. The uppermost panel shows the dipole signal, the second panel from the top the intrinsic energy E_{int} , the third panel the number of escaped electrons (full line: escape from the analyzing box (volume \mathcal{V}), dotted line: escape from the whole numerical box), and the lowest panel shows probabilities for a few selected ionization states as indicated.

This is illustrated in Fig. 14 where these quantities are plotted as a function of time for a collision $\text{Na}_{40} + \text{Ar}^{8+}$ at a velocity $v_1 = v_F$. The impact parameter has been chosen as $b = 26a_0$, which is about twice the cluster radius. The excitation is then a truly external process, as previously discussed. One recovers in Fig. 14 the various trends qualitatively discussed above. The dipole moment exhibits an almost instantaneous large amplitude deformation at the instant of closest approach. This strong excitation of the dipole then quickly relaxes towards much more gentle oscillations that last for a long time. Correlated with the damping of dipole oscillation one can observe a sizable ionization (here about four electrons stripped, on the average). Furthermore, we complement the information provided by the total ionization yield with the more detailed picture given by ionization probabilities (Section 4.2.2), showing only even probabilities for clarity. The latter quantities evolve in time with a pace comparable to the total yield. Note also the “dispersion” in the attained charge states, showing various charge states with sizable probabilities each. Finally, the intrinsic excitation energy (67) is also displayed as a function of time. It is evaluated on the entire

grid and needs to be compared with the dashed line in the panel N_{esc} which stands for the number of finally absorbed electrons N_{abs} . The peak in E_{int} is obviously related to the regime of the strongest slope in N_{abs} . The asymptotic value is established as soon as emission comes to an end.

It is interesting to compare the collision with an ionic velocity equal to the Fermi velocity to a much slower case. The right part of Fig. 14 displays the results of a collision of the same system at the same impact parameter but with an ionic velocity $v_{\text{I}} = 0.1v_{\text{F}}$. We see that the reaction mechanism in the low-velocity case is significantly different from the high-energy case, not just quantitatively, but also to some extent qualitatively. For example, the dipole oscillations of the high-energy case are here replaced by an adiabatic polarization of the electron cloud. This indicates that there is no matching anymore between the time scales of the excitation process (several tens of fs at low energy) and the plasmon period. As a consequence, the Mie plasmon is not excited. We have thus gone over from a diabatic excitation at high energy to an adiabatic one at low energy, which, after all, is not so surprising. Still, it is interesting to quantify the effect and to note that the transition seems to occur in a relatively small projectile velocity window (0.1 – $1v_{\text{F}}$). Differences in ionization are in turn less pronounced, at least qualitatively. The ionization curves exhibit similar patterns, although time scales are different, but the relation between ionization rate and excitation time remains similar. Asymptotic ionization values are by contrast extremely different (almost a factor 2 for this impact parameter). Similarly, the populated ionization channels are quite different and more diverse at low velocity. Finally, it is worth noting that the deposited energies are very similar. In the low-energy case, the peak of E_{int} has essentially disappeared, but the asymptotic values are comparable. The relative intrinsic energies $E_{\text{int}}/N_{\text{esc}}$ are 0.075 eV for $v = v_{\text{F}}$ and 0.057 eV for $v = v_{\text{F}}/10$. The slower case thus tends to leave behind less perturbation in the remaining cluster after the ionization process.

The results displayed in Fig. 14 have been calculated with standard quantum TDLDA in cylindrical symmetry [18,156], while the cartoon-like Fig. 13 has been generated in a Vlasov calculation. Both quantum and Vlasov calculations have been extensively performed for collision processes. Before proceeding, it is therefore important to compare the results obtained with these different techniques. In the following, we consider three types of approaches for ion-cluster collisions: 3D quantum TDLDA calculations [17], 2D Vlasov [72,21], and our 2D quantum TDLDA scheme. Such a comparison has already been performed between the 3D TDLDA and Grenoble calculations [72] with the outcome that the results were quite similar, in particular in terms of cluster ionization. We hence extend this comparison here and add our own results to the previous ones. Fig. 15 gathers the results in terms of ionization for $\text{Na}_{40} + \text{Ar}^{8+}$ collisions at a projectile energy of 80 keV, which corresponds to about $v_{\text{I}} \simeq 0.6v_{\text{F}}$, for various impact parameters b . Altogether we see a remarkable agreement between the various calculations for a global observable such as the average ionization. This proves the validity of our 2D approximation for the projectile potential as well as the validity of a Vlasov approach for that case. Slight differences can be spotted for small impact parameters. But this is harmless because only peripheral collisions are properly described anyway in such a formalism with frozen cluster ions [156,72,203].

6.3. Trends with collision parameters

The discussions of the previous sections have shown that the key parameters which govern the dynamics of the collision between a charged ion and a cluster are the projectile velocity v_{I}

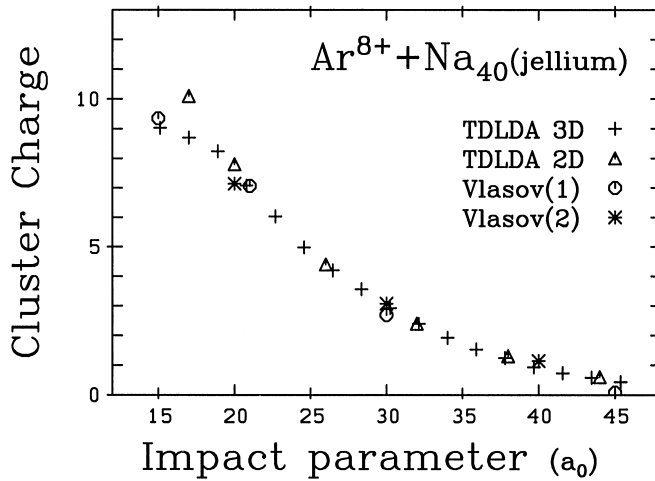


Fig. 15. Cluster charge as a function of the impact parameter of Ar^{8+} hitting a Na_{40} cluster with velocity $v_1 \simeq 0.6v_F$. Various calculations done with various formalisms and codes are compared: 3D TDLDA of [17], 2D TDLDA of [156] (present work) Vlasov of [72] (1) and Vlasov of [21,22] ((2), present work); assignment of symbols as indicated. In order to comply with the calculations of [17,72] the (outdated) steep jellium background has been used here to describe ionic background.

(or energy), charge Q and impact parameter b . In this section we discuss the influence of these various parameters. We restrict the range of variation to the kinematic conditions discussed above, that is, values which actually correspond to experimental conditions [12].

Let us now discuss our calculations performed in close relation to ongoing experiments. We first consider the influence of projectile charge on cluster ionization. Calculations have been performed at the Vlasov level for a Na_{196} cluster bombarded with projectiles of various charges (Q between 8 and 40) and velocity $v_1 = 0.83v_F$. As emphasized in Section 4.1, one of the original motivations for using highly charged projectiles was to attain high charge states without depositing too much excitation energy in the system. It is thus interesting to first consider this aspect. Intuitively, one expects that the more violent the perturbation, the larger the ionization (all kinematic parameters being equal). This is indeed what Vlasov calculations show, as can be seen from Fig. 16. In this figure we plot the deposited excitation energy as a function of final cluster charge (or total ionization) and as function of projectile charge (hence as a function of the violence of the perturbation). As expected, ionization increases with projectile charge, at a given deposited excitation energy. Conversely, for a given ionization state, a higher projectile charge leads to a lowering of the deposited excitation energy, which means that the system is less heated up. These trends appear to be extremely regular (at least on the double logarithmic scales used in the figure). Altogether, it thus seems that the original goal of producing cold ionized clusters is indeed within reach by means of highly charged ionic projectiles. It is, nevertheless, interesting to compare these results to what one can attain with present-day fs lasers. A first hint can be drawn from Fig. 21 later on. There one finds a thermal energy of 0.07 eV per cluster ion for 1.4 emitted electrons. This is close to what we see here for ionic collisions. Lasers may therefore be able to compete with ionic collisions in terms of cold ionization, but this point has yet to be thoroughly investigated.

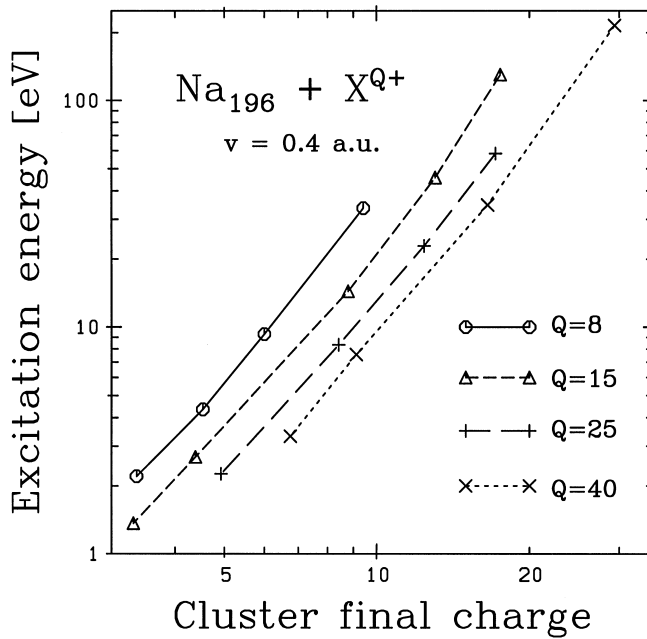


Fig. 16. Deposited excitation energy as a function of projectile charge in a Na_{196} cluster (steep jellium) hit by ions of various charges, as indicated. The projectile velocity is $0.83v_F$. The excitation energy is defined in Eq. (12) of [72]. Data points from courtesy of [72].

The results presented in Fig. 16 were obtained for a projectile velocity of $v_1 = 0.83v_F$, close to the conditions of ongoing experiments. Let us now see what happens if the kinematic parameters are modified, in particular the projectile velocity. In Fig. 17 we study $\text{Na}_{40} + \text{Ar}^{8+}$ collisions at projectile velocities $v_1 = 0.1$ and $1v_F$. Calculations have been performed here at the TDLDA level (2D calculation [156]). Again, the trend is very regular and shows that for a smaller projectile velocity one attains a larger ionization state for the same deposited excitation energy. A “slow” projectile thus favors a cool ionization (smaller excitation energy per bound electron, see also Fig. 14). Both Figs. 16 and 17 thus converge towards a simple conclusion which can be stated in the following way: collision of clusters with highly charged ions at low velocities allow one to reach high cluster ionization with minimal excitation energy in the remaining cluster. The effect becomes more pronounced the higher the projectile charge and when using moderate impact velocities ($v_1 \lesssim v_F$). It would be interesting to extend these investigations in a more systematic way to determine the optimal conditions to achieve a maximum cold ionization. It is also quite telling to compare these results to the ones obtained within exciting the cluster by a fs laser pulse. This comparison is done in Fig. 17 where we have also indicated the results attained with a laser of frequency $\omega_{\text{laser}} = 2.7 \text{ eV}$, pulse length 50 fs. The intensity is varied in a broad range to cover the various N_{esc} drawn in the figure. We see from this comparison that in the low ionization regime ions indeed deposit less excitation energy than the laser. But this is not anymore the case when high ionization states are considered. In this case the laser clearly ionizes while depositing much less excitation energy than ions (mind the logarithmic scales in Fig. 17). This effect is not specific of the

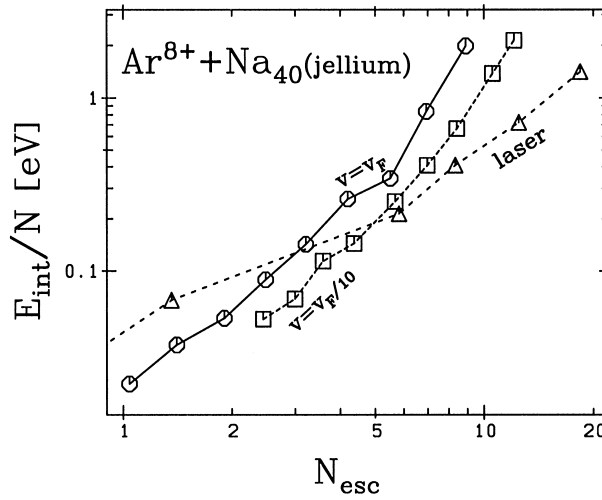


Fig. 17. Intrinsic excitation energy versus number of escaped electrons for a collision of Ar^{8+} with a Na_{40} cluster described in the soft jellium model and for two ionic velocities, as indicated. Additionally, a result from laser excitation (see next Section 7) is shown, using a \cos^2 pulse with FWHM of 50 fs and frequency $\omega_{\text{laser}} = 2.7 \text{ eV}$.

laser parameters considered here. Recent systematic comparisons have confirmed this trend for several sets of laser parameters and ionic projectiles [204].

Finally, we study the dependence on the impact parameter b , discussing this aspect again for the case of collisions of Ar^{8+} with a Na_{40} cluster. In Fig. 18, we plot deposited energy and ionization versus b . As expected, both quantities decrease with increasing impact parameter. This simply illustrates the fact that the larger the impact parameter, the more gentle the collision. More interesting is the comparison between collisions at two different velocities ($v_{\text{I}} = v_{\text{F}}$ and $v_{\text{I}} = 0.1v_{\text{F}}$). Although the two velocities lead to qualitatively similar results, there are differences in quantitative details. In particular, one observes (middle panel of Fig. 18) that the low-velocity case leads to significantly more ionization, at a given impact parameter, than the high-velocity case. This trend is in agreement with the findings of Fig. 17. The effect is pronounced at any impact parameter, although for large ones the difference shrinks. This latter aspect reflects the fact that for very large impact parameters ionization will disappear, whatever the projectile velocity. The behavior of the deposited excitation energy is also quite interesting. We observe that lower velocities produce much more ionization while E_{int} grows only by a moderate amount. This renders the whole process colder, in accordance with the direct comparison seen in Fig. 16.

The lower panel of Fig. 18 finally displays some of the ionization probabilities for the high-velocity case ($v_{\text{I}} = v_{\text{F}}$), providing a more complete picture in addition to the total ionization given by N_{esc} (middle panel of Fig. 18). As expected, one observes the rise and fall of each ionization state as a function of impact parameter. It is interesting to note how each curve is, to a large extent, separated from the other ones. In other words, the maximum of each ionization state singles out a definite impact parameter range. This could suggest to use ionization to determine the actual impact parameter, a quantity which is usually difficult to access experimentally. Similar ideas have been used successfully in nuclear physics to deduce the impact parameter for a heavy ion collision from neutron multiplicities [205].

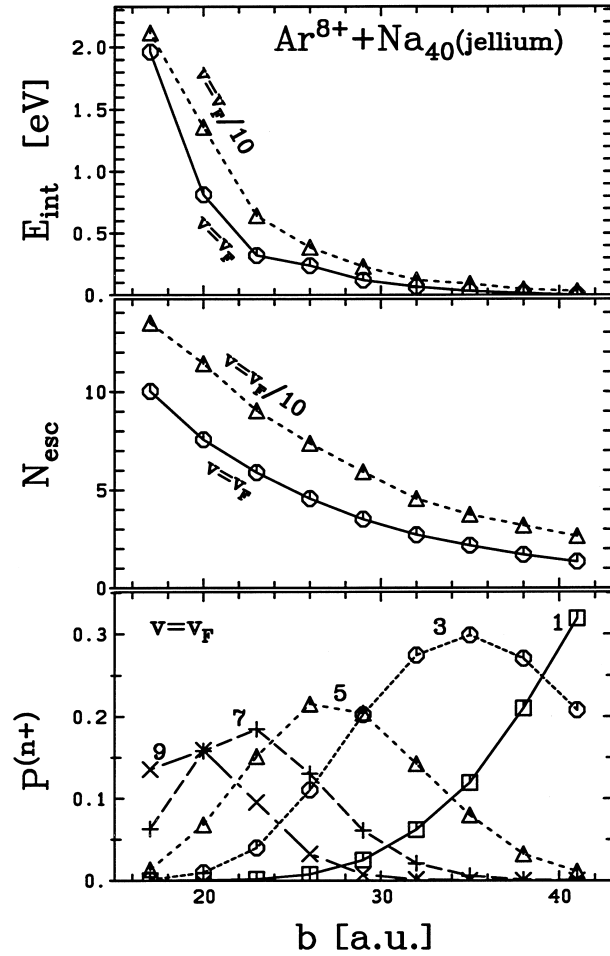


Fig. 18. Trends with impact parameter for the asymptotic values of the basic observables for a collision of Ar^{8+} with a Na_{40} cluster described in the soft jellium model. Two cases of ionic velocity are considered, $v = v_F$ and $0.1v_F$, as indicated. The uppermost panel shows the intrinsic excitation energy E_{int} , the middle panel the number of escaped electrons, and the lowest panel shows a few selected ionization states for the case $v = v_F$, as indicated.

Ionization probabilities furthermore provide the input for evaluating ionization cross sections, which are more readily accessible from experiment. For a given charge state, the corresponding cross section is obtained by integrating over all impact parameters. For fundamental and technical reasons, the integration is limited to impact parameters larger than the cluster radius. Thus, only those charge states can be safely estimated that are peaked well inside the range of impact parameters in our computations. This can be visually estimated from Fig. 18 in the high-velocity case, and similarly by plotting ionization probabilities for the low-velocity case. In the collisions we consider here, the properly accessible charge states are thus found to be $3+$ to $8+$ for $v_i = v_F$ and $5+$ to $10+$ for $v_i = 0.1v_F$. The corresponding cross sections are plotted in Fig. 19. We see that lower projectile velocities are again more efficient in generating large total ionization cross sections.

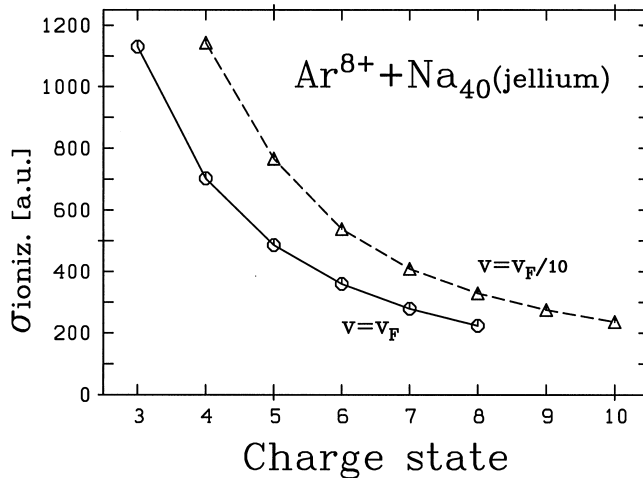


Fig. 19. Ionization cross sections (in a_0^2) for Na_{40} hit by an Ar^{8+} ion at two velocities $v_l = 0.1v_F$ and v_F .

But we also see that higher charge states (above $10+$) are not so easy to reach with good statistics. One probably needs even more highly charged projectiles to reach that goal. An alternative could be fs lasers which can be tuned to any desirable ionization and which are also very efficient in reaching high final charge states [204], see Fig. 17.

6.4. Effects of electronic two-body collisions

Only very recently, first investigations of the effects of electronic two-body collisions on the dynamics of clusters have started [23]. Realistic simulations in the case of cluster-ion collisions or laser irradiations are still in progress [109], and we thus only give a short preliminary account.

We focus here on a relatively gentle collision between a 10 keV proton ($v_l \simeq v_F$) and a Na_9^+ cluster. In the following, we compare the electronic dynamics as described at mean field level (Vlasov) and beyond (VUU), see Section 2.6. As usual, the electronic response is characterized by a dipole excitation, immediate ionization and energy deposit. In the case of such a high-velocity projectile, the perturbation is so sudden that Pauli blocking should effectively cancel out two-body electronic collisions, at least during the excitation phase itself. This is indeed what is observed. Both dipole signal and ionization are essentially insensitive to two-body collisions. Consequently, VUU and Vlasov give similar results for the first time steps of excitation. This means that during the first phase of the reaction, including the excitation itself and the early relaxation (dipole damping and quasi-instantaneous ionization), a mean field description is well adapted to the situation. However, the violent perturbation inflicted to the cluster has deposited substantial excitation energy and thus widely opened phase space, and electron–electron collisions can be expected to start playing a role with time progressing. Of course, at least in this case, both dipole signal and ionization have already “converged” towards their asymptotic value, so that no effect is visible on these observables.

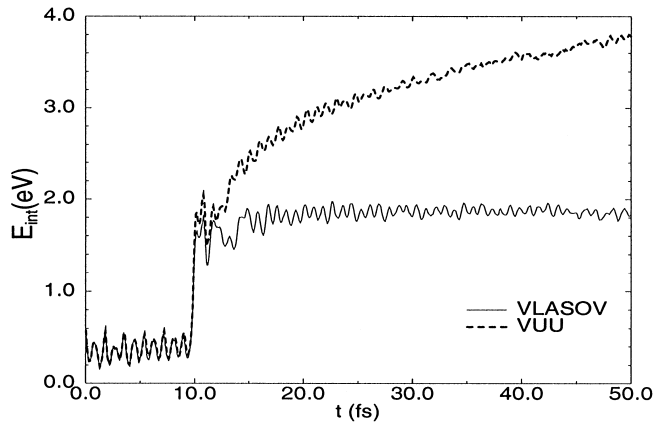


Fig. 20. Electron intrinsic energy E_{int} as a function of time during a proton- Na_9^+ collision, as obtained from Vlasov (full line) or VUU (dashed line) computations. The Na_9^+ was described within the soft jellium model. From [109].

The opening of phase space can be illustrated in terms of the deposited excitation energy, as shown in an impressive manner in Fig. 20. The time evolution of the excitation energy clearly exhibits two regimes corresponding to the two of the dynamics identified above. During the first phase, which lasts here up to about 15 fs (the instant of closest approach is set here at $t_0 = 10$ fs) and includes excitation and early relaxation, both Vlasov and VUU calculations perform exactly the same. But beyond about 15 fs one observes a gradual building up of excitation energy in the VUU case, totally absent from the Vlasov results. This exactly reflects the opening of phase space, due to the fact that mean field (alone) has already allowed a sizable energy deposit (about 2 eV at 12 fs), enough to significantly soften Pauli blocking and thus activate two-body collisions. This opening of phase space hence allows a piling up of two-body collisions, progressively heating up the electron cloud. At 50 fs the total excitation energy starts to gradually level off in the VUU calculation but has already reached about twice the Vlasov value.

The example described above, in which two-body collisions start to play a role in the late phase of the reaction, is quite generic for high-energy ionic collisions. Pauli blocking inhibits two-body collisions up to a time at which the mean field has brought enough excitation energy into the system to open up phase space. One might expect some deviations at lower ionic velocities for which characteristic time scales are different, but it turns out that the differences are not so large. The authors of [109] have, for example, investigated the case of a low-velocity collision (Ar^{8+} on Na_9^+ at $v_1 = 0.1v_F$) and found that, in this adiabatic case, Vlasov and VUU again behave in a way similar to the high-energy case, although for different reasons. Indeed, at such low velocity (see Section 6.3) the dipole response is essentially an adiabatic polarization of the electron cloud, and, precisely for this reason, it stays essentially unaffected by two-body collisions. Ionization behaves in comparable ways. But again, energy deposit is sizably different in Vlasov and VUU calculations. VUU leads to a much larger energy deposit than Vlasov, because two-body collisions have the time to develop and progressively store excitation energy in the system. The associated time scales are similar in both cases of rapid or slow projectile. This is because there is roughly a 10 fs delay

before the electron–electron collisions become active. But the interaction time with most of the considered projectiles is shorter than that.

All in all, we thus see that the two-body effects essentially do not interfere with the excitation process in the course of ionic collisions. They of course play a crucial role to determine the subsequent energy storage in the electron cloud, but this second phase of the process seems to be rather independent from the details of the first phase. We shall see in the next section that the flexibility of laser irradiations gives access to more spectacular effects in this respect.

7. Irradiation with intense laser beams

7.1. Basic mechanisms: a detailed case study

The discussions of Section 6 have shown the richness of the various phenomena at work during the collisions between a highly charged ion and metal clusters. We now want to explore the complementing (and even richer) field of laser excitations, made possible by numerous experimental developments due to the rapidly improving technological capabilities of present-day lasers.

The key parameter of a laser is its frequency ω_{laser} . Indeed, even far into the high-intensity short-pulse regime, the spectrum of the electromagnetic pulse hitting the cluster is very narrowly centered around the laser frequency. In other words, the laser excitation is frequency selective. This is at variance with a perturbation due to an ionic projectile, which provides a spectrally “white” signal covering a broad band of frequencies. Not surprisingly, the electronic dynamical response, with its plasmon-dominated behavior, turns out to depend critically on the relation between ω_{laser} and the resonance frequencies of the system. This has been exemplified for the test case Na_9^+ in [206].

In order to show the generic nature of these results, we consider here the larger cluster Na_{41}^+ . Fig. 21 shows dipole signal, number of escaped electrons N_{esc} , and intrinsic thermal excitation energy as a function of time for two different laser conditions, off-resonant (left panels) and close to Mie plasmon resonance (right panels). Pulse profile (\cos^2) and length T_{pulse} are the same in both cases. However, the intensities need to be dramatically different in order to arrive at a comparable response. To be more precise, we have tuned I to provide approximately the same intrinsic excitation energy E_{int} in both cases. The off-resonant case, of course, needs a much larger intensity (by two orders of magnitude) than the on-resonant one. The associated dipole signal closely follows the laser profile (the dashed line indicates the response of a classical oscillator). It reaches an appreciable amplitude but fades away as soon as the laser excitation disappears. Direct electron emission is directly related to the dipole amplitude: the steepest slope in N_{esc} coincides with the largest dipole moment. This suggests a scenario where ionization is caused by a “spilling out” of the fastest electrons – just like water spills out of a glass that is shaken back and forth. Ionization (N_{esc}) eventually levels off as soon as the dipole signal goes down to zero. It is noteworthy that the intrinsic excitation energy E_{int} follows the same pattern, which suggests that it is closely related to N_{esc} . In fact, we will see later that the electronic emission proceeds very differently for each individual occupied state, see Fig. 22. This leads to different flow patterns in each single-particle state that may turn into turbulences, thus contributing to intrinsic excitation (as opposed to collective flow). Finally, Fig. 21 demonstrates that the total energy absorbed from the laser field by

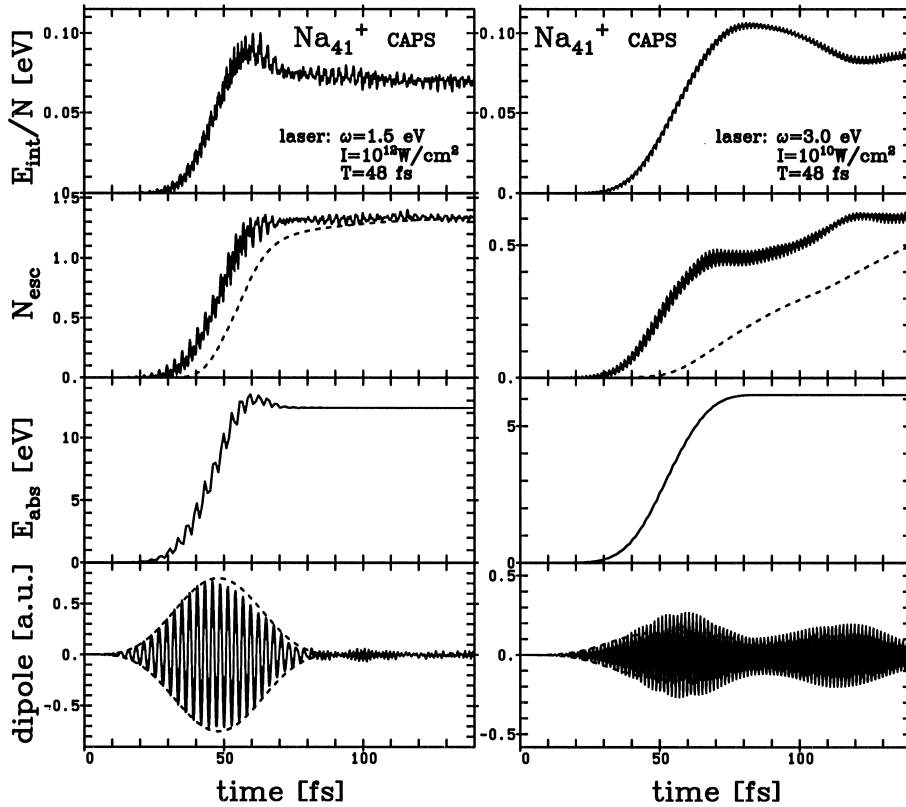


Fig. 21. Time evolution of basic observables for laser excitation of a Na_{41}^+ cluster with ionic background in CAPS. The laser parameters are indicated in the plots. The left part stems from a laser off resonance ($\omega = 1.5$ eV) and the right part from a laser slightly above resonance ($\omega = 3.0$ eV). The uppermost panel shows the intrinsic excitation energy E_{int} , the second panel the number of escaped electrons (full line: escape from the analyzing box, dotted line: escape from the whole numerical box), the third panel the amount of energy absorbed from the laser field, and the lowest panel the dipole signal.

the cluster exhibits the same pattern as N_{esc} . This suggests that direct electron emission is a process that converts part of the absorbed energy immediately to free electrons and stores the rest as intrinsic thermal excitation energy.

The behavior of the case with ω_{laser} close to resonance is quite different from the off-resonant case (Fig. 21, right panels). The dipole signal has no resemblance whatsoever with the pulse profile. In fact, with the intensity being a factor 100 lower, the classical pulse profile is a tiny fraction of the observed dipole signal. We are thus dealing with a case of strong field amplification due to resonant conditions (see also the discussion in connection with Fig. 24). The dipole oscillations seem to acquire a life of their own and persist long after the laser has been switched off. Electron emission and associated intrinsic excitation, however, are again taking place in immediate reaction to energy transfer from the laser field, see the third panel from above showing the energy absorbed from the laser field, Eq. (68). Moreover, it is interesting to note that for the resonant case less electrons are emitted asymptotically for about the same intrinsic excitation energy E_{int} as in the off-resonant case. Reading it the reverse way: the resonant excitation produces more intrinsic heat in the

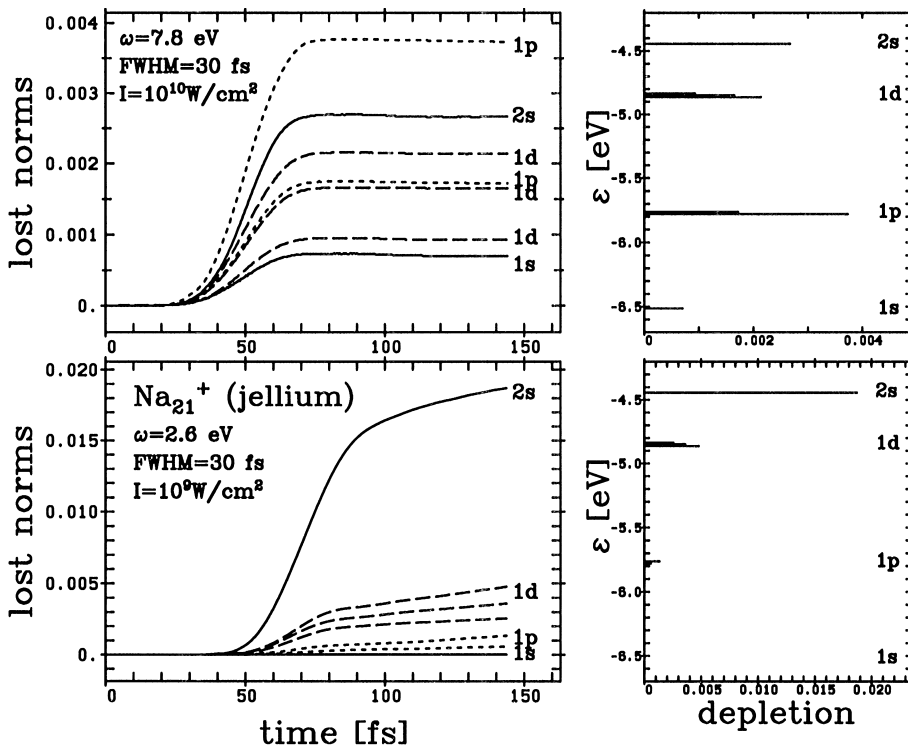


Fig. 22. Time evolution of absorbed norm from the various single-electron states of Na_{21}^+ with soft jellium background. The left part shows results for two different laser frequencies, one close to resonance (lower part) and one safely above ionization threshold (upper part). The right panel shows the stationary single-electron spectrum with the amount of depletion of each state. The single-particle states are indicated in each plot by their standard spectroscopic assignment.

residual cluster, for a given number of emitted electrons, than the off-resonant one. The off-resonant case, on the other hand, produces far less electron per invested intensity. This is to be kept in mind if we aim just at a large production rate. In any case, the example shows how a desired result can be obtained with appropriate choice of the laser parameters. Finally, let us have one more look at the absorbed energy E_{abs} as displayed in the third panel of Fig. 21. As already mentioned, the regions of strong increase go hand in hand with large dipole response, and the other observables are rapidly changing, too. The total absorbed energy is directed into two channels of the reaction: part of it is converted into intrinsic energy (25% for the off-resonant and 60% for the resonant case), and the rest is used for direct electron emission. The asymptotic collective energy is very small in both cases. Thus the remaining energy is used up for direct electron emission.

The intrinsic excitation energy E_{int} is that part of the total excitation energy which cannot be expressed in terms of the collective flow, see Section 4.2.3. It arises because the various single-electron states develop a slightly different dynamics, each one having their own current $\mathbf{j}_i(\mathbf{r}, t)$ which deviates a bit from the mean current flow. Fig. 21 already suggests that thermalization and emission are closely related. This can be investigated in more microscopic detail. Each single electron state has a different threshold and will thus react differently to emission. This brings the

j_i out of phase and gives rise to E_{int} . Fig. 22 visualizes the different emission patterns in terms of the relative number of emitted electrons per separate state (left panels). It is obvious that the various states emit very different amounts, although the temporal profile is the same amongst all states for a given case. These qualitative features are common to both test cases, but the details differ significantly. For high frequency (above emission threshold, upper panels) the electrons are emitted at the peak time of the external field, whereas in the resonant case (lower panels) emission extends to later times. The same behavior is seen for the total N_{esc} in the previous Fig. 21 and discussed there. One also sees a huge difference in the ordering of states according to their yield. The resonant case emits most electrons from the least bound 2s state and less and less from the more strongly bound states. By contrast, the high-frequency case shows a much different (and less expected) ordering.

As we have seen that the temporal profile of particle emission is the same for all states, it suffices to compare the final values of the occupation numbers. This is done in the right part of Fig. 22. For the resonant case, emission seems to follow the ordering of the binding energies. That is understandable because the threshold is larger than the laser frequency. Thus, emission is induced by multi-photon processes and becomes less likely the higher the actual threshold. But energy is not the only criterion. One sees (left panels) that degenerate states with different values of m (three 1d states and two 1p states) emit quite differently. This is related to the transition matrix elements for the excitation operator \hat{D}_z which favor the $m = 0$ states. The situation is different for the high-frequency laser. Here the depletion seems to override energetic considerations completely. The reason for this is that the laser frequency is high enough so that all states can emit directly (i.e. with a one-photon process) into the continuum. Then the transition matrix elements take the leading role and determine the ordering in which the levels are depleted. In both cases (below and above ionization threshold), we see that the final distribution of occupation numbers (the complement of the depletion) is far from being thermal. The emission thus produces intrinsic excitation as side effect, but not of truly thermal nature. This last step of thermalization requires electron–electron collisions which allow for equilibration of single-particle occupation numbers. This, however, goes beyond TDLDA. We will discuss the handling of such collisions and some consequences in Section 7.5.

Without showing explicit results, we mention that excitation by a collision (or by an instantaneous mechanism) produces a distribution which is very similar to the resonant laser discussed above. It respects the energetic ordering of single-particle states, but the different m values in a set of degenerate levels behave quite differently.

7.2. Trends with laser parameters

The detailed time evolution of the excitation processes discussed in Section 7.1 cannot be resolved with current experimental techniques. Instead, realistic experiments only measure the final outcome of the reactions, a long time after the laser excitation itself. This means that theoretical predictions are required for the asymptotic values of the observables depending on the various laser parameters. We will discuss here different cuts through the landscape of parameters.

7.2.1. Tuning the laser frequency: resonant ionization

We begin by quantifying the previously identified impact of laser frequency on global ionization. Fig. 23 shows electron emission N_{esc} versus laser frequency ω_{laser} for the test case Na_9^+ and for three

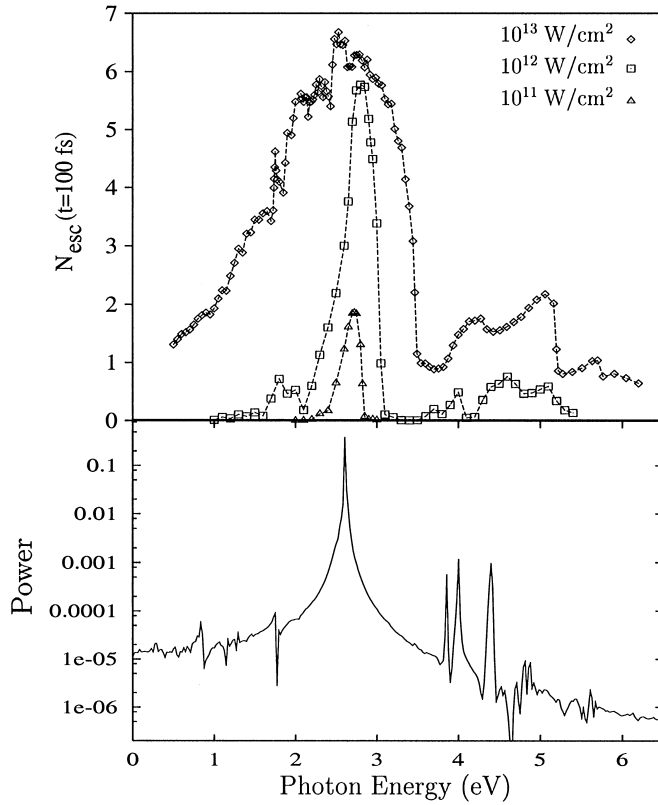


Fig. 23. Number of emitted electrons N_{esc} (upper panel) versus laser frequency ω_{laser} for a laser irradiating a Na_9^+ cluster (with soft jellium background) at various intensities, as indicated. The pulse profile was a Gaussian with FWHM of 25 fs. For completeness the power spectrum of Na_9^+ (in the linear regime) is also indicated. From [206].

different intensities. It also provides the spectral distribution of the dipole moment for comparison (lower panel) [206]. We see that $N_{\text{esc}}(\omega_{\text{laser}})$ follows the same pattern as the dipole power spectrum. This is not surprising: when approaching resonance, the dipole amplitude gets boosted by field amplification (Section 7.2.2). The amplitude, in turn, determines the emission.

At second glance, we see that the N_{esc} signal becomes broader with larger intensity. This can be understood from the fact that large emission modifies the system dramatically and thus changes the resonance conditions (see also Fig. 9) during the excitation process. A more quantitative explanation can be drawn from the study of field amplification (see below). The enhancement factor is largest for small yield and shrinks if emission reaches a critical value. The broadening in Fig. 23 can thus also be understood from the fact that the peak values are suppressed by reduced amplification which gives the wings of the peak the chance to keep up.

7.2.2. More on the microscopic behavior: field amplification effects

We had seen hints of field amplification near resonances in the dipole signal in Fig. 21 and in the trends of $N_{\text{esc}}(\omega_{\text{laser}})$ in Fig. 23. We will now discuss this mechanism, following the lines of [207].

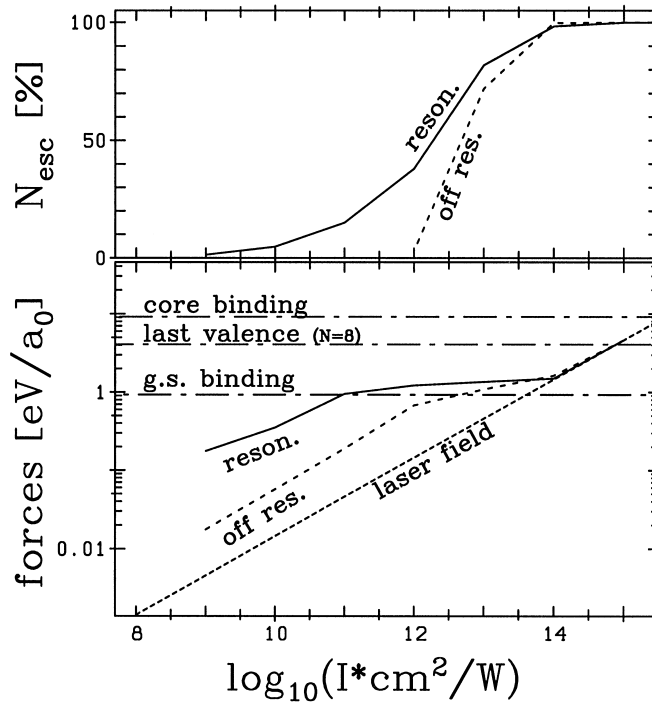


Fig. 24. Lower panel: schematic view of the various forces on the electrons as a function of laser intensity I . The force from the laser field (dotted) grows $\propto \sqrt{I}$. The actual force on the valence electrons is amplified by electronic response and shown for two typical cases, on (full) and off (short dashed) the Mie resonance. The limits for binding in the ground state of Na_9^+ (soft jellium) and for full ionization (“last valence”) are indicated as well as the binding force of the nearest core electrons (all dash-dotted). Upper panel: number of escaped electrons N_{esc} as a function of laser intensity I , for the two cases on and off resonance. Adapted from [207].

The quantity that is amplified is the time-dependent net force on the electrons, compared to the bare external force $eE_0 \cos(\omega_{\text{laser}} t)$ exerted by the laser. Although this enhancement takes place globally, it is convenient to quantify it through its maximum local value, which is determined in two steps. First, one evaluates at a given time t the maximum force from the total Kohn–Sham potential Eq. (8), $F(t) = \max_r(|\nabla v(\mathbf{r}, t)|)$. The value of $F(t)$ at the initial time $t = 0$ is given by the maximum of the binding force which keeps the electrons in the cluster and is peaked at the surface region. The laser then induces large oscillations of $F(t)$. We take the upper and lower envelopes $F_{\text{up/low}}$ of the maximum force signal $F(t)$ and finally determine the maximum net force as $F_{\text{max}} = \max_t(F_{\text{up}}(t) - F_{\text{low}}(t))$. This is then to be compared with the external force and thus quantifies field (or rather, force) amplification, for details see [207].

The lower panel of Fig. 24 shows the net peak force thus determined for the test case Na_9^+ and for different laser intensities. The full line is the result for a laser whose frequency is in resonance with the Mie plasmon ($\omega_{\text{laser}} = 2.58 \text{ eV}$). The dashed line shows an off-resonant case ($\omega_{\text{laser}} = 2.04 \text{ eV}$). The force from the external laser field is shown for comparison as dotted line. Both cases (on and off resonance) show significant amplification for low intensities, the resonant case, of course, much more. At larger intensities, however, the amplification levels off and disappears completely for

$I > 10^{14} \text{ W/cm}^2$. This trend can be understood from looking at a few other typical forces in the system. These are indicated with dash-dotted horizontal lines: the binding force of the last electron in the ground state, the binding force of the last valence electron before complete stripping, and the binding force of the core electrons in Na. It is obvious that the ground-state binding force is limiting the maximum force that can be achieved by amplification. There is, nevertheless, a transient regime where some amplification persists. But it stops long before all electrons are stripped (see the line “last valence”). This makes sense because a sufficient number of valence electrons are needed to build a collective plasmon oscillation. Because amplification is larger, the resonant case reaches the limiting field earlier and takes a longer transient regime. In fact, it is interesting to note that amplification stops for all cases at about the same intensity. This trend is corroborated by looking at the corresponding ionization (N_{esc}), see the upper panel of Fig. 24. Significant values for N_{esc} are correlated with the transient regime of reduced amplification, and the transition is obviously much broader for the resonant case.

The lower panel of Fig. 24 also shows the binding force of a core electron (“core binding”). It stays well above any other forces and comes into play only for very intense lasers with $I > 10^{16} \text{ W/cm}^2$. This is a particularly convenient feature of the simple metal Na which guarantees an optimal decoupling of valence and core electrons. The situation is more involved in other materials, as e.g. noble metals, where the outermost core electrons are much closer to the valence electrons and may interfere more easily with the valence shell in dynamical processes [208]. We thus expect that the pattern for other metals, as e.g. Ag, Au or Pt, look essentially the same in the regime of low intensities where field amplification is nourished by the plasmon resonance. But differences will appear around and above the critical point where ground state binding is reached. The dynamical excitation of the valence cloud may shake the outer core electrons so much that they become delocalized. This effectively increases the number of valence electrons per ion which, in turn, changes all relations (e.g. plasmon frequency) dramatically. One may speculate that a new onset of field amplification could occur at larger intensities, taking advantage of the now larger density of mobile charges. There may thus be a wealth of new and exciting phenomena waiting to be explored.

The two above cases on and off resonance have shown very different degrees of amplification. In Fig. 25 we plot the maximum forces for fixed intensity and systematically varied frequency. For comparison, the upper panel gives information about the dipole strength function of the corresponding cluster. We see indeed a peak of the force just where the plasmon resonance sits (see also Fig. 23). Force amplification then decreases again with growing distance from the resonance. Note the asymmetric shape of the force versus frequency: the system still experiences a sizable amplification far below resonance, whereas the force decreases much more quickly above. The reason is that larger frequencies make electron emission more likely (because ω_{laser} is then closer to the threshold) and this accelerates the limiting process. Fig. 25 also shows the result for the larger cluster Na_{93}^+ which has a broader resonance region due to Landau fragmentation (see the discussion in Section 5.2). Correspondingly, the peak in field amplification is much broader than in case of Na_3^+ , although similarly asymmetric around the resonance region.

7.2.3. Scaling law of ionization with intensity

Figs. 23 and 24 have indicated that N_{esc} can rise steeply with intensity I . In fact, one can deduce from multi-photon perturbation theory that ionization (N_{esc}) scales with laser intensity I as

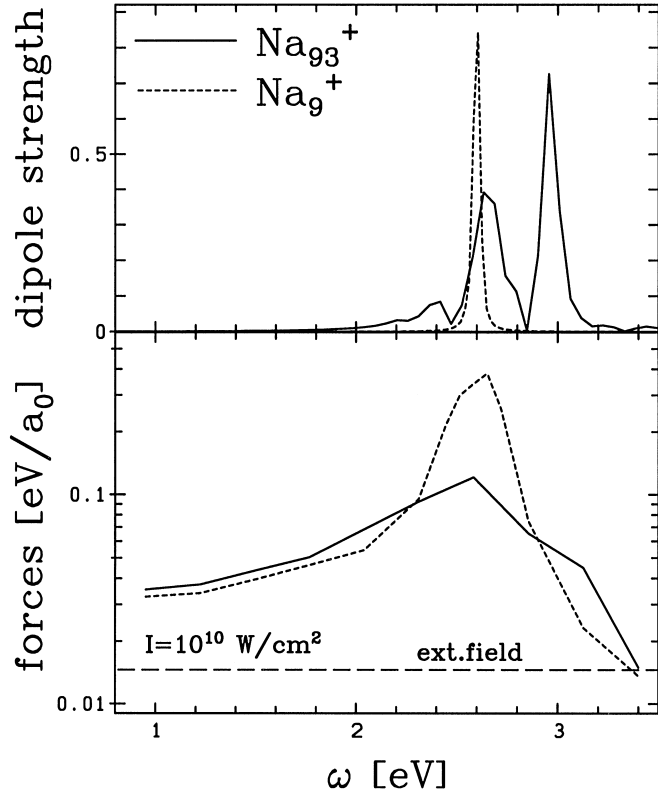


Fig. 25. Lower panel: trends of maximum field strength versus frequency for the clusters Na_9^+ (dotted line) and Na_{93}^+ (full line) irradiated with a laser beam of intensity $I = 10^{10} \text{ W/cm}^2$. Both clusters are described with the soft jellium model. For comparison we also provide the maximum field strength of the external laser field. Upper panel: the dipole power spectrum for the two clusters as indicated. From [207].

$N_{\text{esc}} \propto I^\nu$, in the perturbative regime of low electron yield [158]. Fig. 26 shows N_{esc} versus intensity I for the test case Na_9^+ and for several laser frequencies. The I^ν law is characterized by straight lines in this doubly logarithmic plot, and we see that it is nicely fulfilled in the regime of low perturbation or intensity (i.e. low N_{esc}), off as well as on resonance. Deviations from the linear behavior arise for larger intensities. Note that the relative positions of the curves are mainly determined by the relation of laser frequency to plasmon resonance: the farther the laser frequency from the plasmon resonance, the higher the intensity needed to initiate ionization (at least as long as ω_{laser} remains well below ionization threshold). Ionization with $\omega_{\text{laser}} = 2.7 \text{ eV}$ thus starts out at the smallest intensities. One also sees in Fig. 26 that the slope increases with decreasing laser frequency. That confirms the expectation of the perturbative estimate, which predicts the slope to be

$$\nu = \text{int}^+(E_{\text{thresh}}/\omega_{\text{las}}), \quad (71)$$

where “ int^+ ” means the next higher integer. Fig. 27 shows a summary of the slopes for the various frequencies (circles connected by a full line to guide the eye) and compares them with estimate (71).

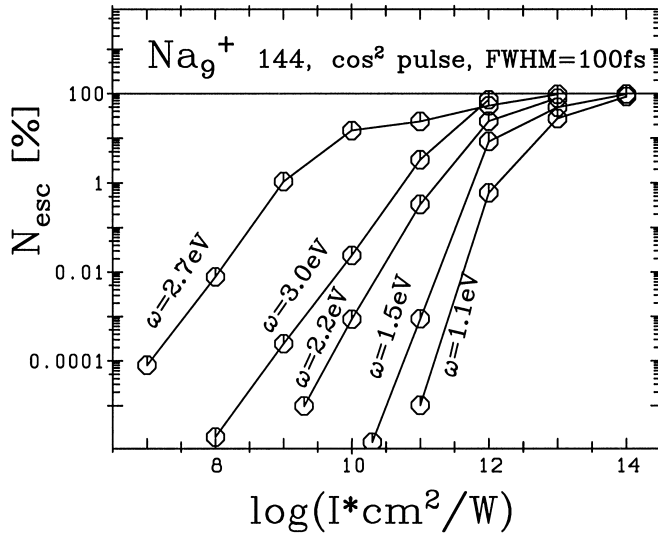


Fig. 26. Fraction of emitted electrons N_{esc} in % versus laser intensity for various frequencies $\omega = \omega_{\text{laser}}$, as indicated. The pulse profile was a \cos^2 with FWHM of 100 fs. Calculations have been done with a CAPS 144 ionic ground state.

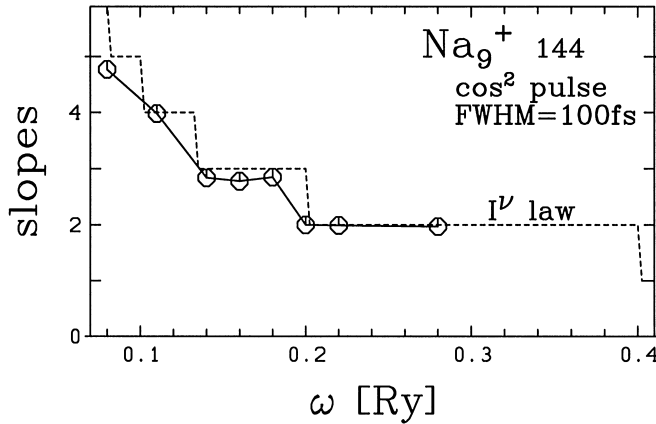


Fig. 27. Slopes of $N_{\text{esc}}(\log(I))$ as function of laser frequency $\omega = \omega_{\text{laser}}$. The dashed line shows the perturbative estimate I^ν , $\nu = \text{int}^+(E_{\text{threshold}}/\omega_{\text{laser}})$. The pulse profile was a \cos^2 with FWHM of 100 fs. The ionic background is the CAPS 144 configuration of Na_9^+ .

As we are in the perturbative regime at low intensities, the single-particle energy of the last occupied electron has been used here as the value for the threshold energy E_{thresh} entering the I^ν law. The result perfectly agrees with the perturbative estimate.

It is to be noted that previous work [206] gave results which were slightly at variance with estimate (71). It turns out that this is due to the fact that very short 25 fs Gaussian pulses were used [206]. This particular pulse shape has a small but finite value when switched on and off during the

calculation. This, together with the fact that the pulses are extremely short, induces some spectral noise which, in turn, admixed always a tiny bit of the plasmon resonance. Not surprisingly then, we found a significant resonant enhancement of electron emission. The 100 fs \cos^2 pulses used here, on the other hand, have a much better spectral selectivity which avoids unwanted resonance coupling and nicely recovers the analytical result. This little exercise demonstrates that one should take care to have spectrally clean laser signals when going for such subtle effects. It also shows, on the other hand, that a fine tuning of the pulse shape may be a useful instrument for probing interesting details of the ionization mechanism.

We have seen that the pure I^ν law is recovered only in the extreme perturbative limit. But this perturbative regime ends at much lower intensities in case of excitation close to resonance, see the extraordinary shift towards lower I of the curve for 2.7 eV in Fig. 26. Finally, we ought to mention that one needs SIC to obtain the correct ionization thresholds from the single-particle energies, see the next Section 7.3. The present TDLDA results are thus not meant for a quantitative comparison with experiment. The goal was merely to study the validity of the I^ν law for metal clusters, in spite of the presence of a strong plasmon resonance.

7.3. Self-interaction effects

Considerations have reached a stage where one should be concerned about the validity of TDLDA. The I^ν law was recovered in Fig. 27 by using the last bound single-electron energy as threshold, which corresponds to 6.0 eV in the case of Na_9^+ (with ionic structure). That is, in fact, not the correct value. The true ionization threshold, obtained as the difference of Na_9^+ and Na_9^{2+} in two separate LDA calculations, comes out as 7.4 eV. TDLDA thus violates Koopmans' theorem grossly. The latter states that in Hartree–Fock theory the last bound single-particle energy coincides with the (unrelaxed) ionization energy [209]. A similar statement holds in DFT [35,31]. This deficit of the LDA is largely due to the fact that it contains a self-interaction error which is absent in a full Hartree–Fock theory. The latter, however, is computationally too involved. Thus, one prefers to resort to a local scheme in which one somehow tries to cure the self-interaction error. This is the method of SIC as introduced in [35]. The formal details had been expounded in Section 2.3.2. We will sketch here briefly the practical implications while employing the OEP approach to SIC [90].

Fig. 28 compares TDLDA and SIC dipole spectra (upper panel) and electron emission (lower panel). The global patterns of TDSIC are well reproduced by TDLDA, but differences show up in detail. There is a small shift of the resonance as a whole (about 3%) and a change in the fragmentation structure. The TDSIC resonance peak has a little sidepeak which comes from interference with one particular 1ph state closeby. This state seems not to be present in TDLDA. We thus have to conclude that going from TDLDA to TDSIC strongly affects the 1ph structure. This can also be seen from the low energy peaks in the dipole strength which show that several 1ph states get appreciably displaced by the SIC. This is not surprising because SIC is by construction especially sensitive to properties of single-electron states. Little change is however seen at first glance for N_{esc} (lower panel). On closer inspection, however, one spots that the SIC makes a difference in detail, again in the typical shifts of the secondary peaks. The example, nevertheless, shows that TDLDA gives a pertinent picture of the global features and thus remains the method of choice for exploratory studies. This has also been pointed out in [210] where excitation energies for

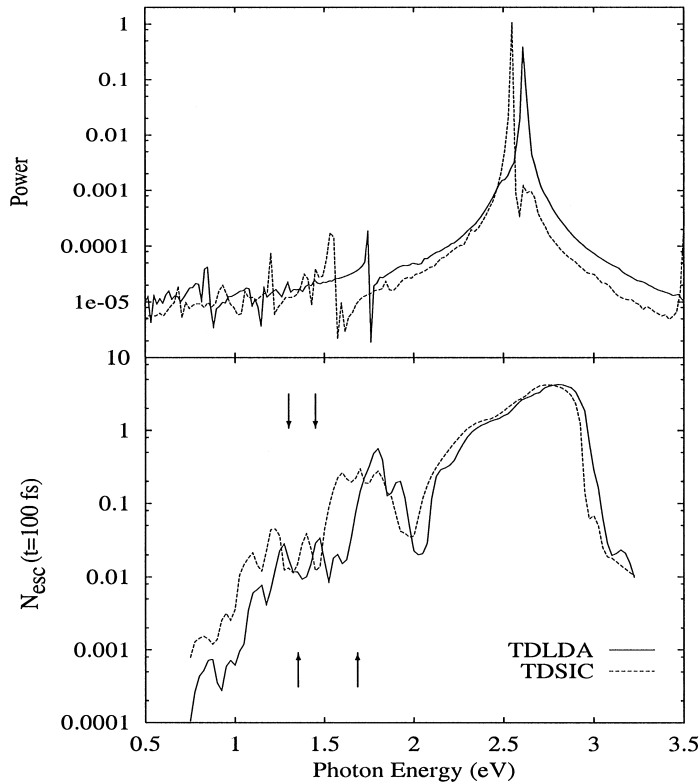


Fig. 28. Number of emitted electrons N_{esc} versus laser frequency ω_{laser} for a laser with peak intensity $I = 5 \times 10^{11} \text{ W/cm}^2$ and FWHM of 25 fs. The figure compares results from LDA (full line) and SIC (dotted line). The arrows indicate the positions of the $1p \rightarrow 1d$ and $1p \rightarrow 2s$ transitions. The upper arrows stand for TDSIC and the lower ones for TDLDA. Test case was Na_0^+ with soft jellium background. From [90].

atoms and clusters were calculated within linear response. However, one should consider moving to SIC if one aims at capturing finer details, particularly in secondary peaks.

Details of particle emission, as we will discuss below in Section 7.4, are an example where SIC is indispensable from the onset. This is related to the restoration of Koopmans' theorem. We find for the test case Na_0^+ in TDLDA a discrepancy of 1.3 eV as discussed above. Inclusion of SIC, even in the simplest globally averaged approximation [211,91], reduces the discrepancy to below 0.1 eV. This then provides a satisfying starting point for any studies where single-particle energies play a role.

7.4. Kinetic energy spectra of emitted electrons

We have discussed so far several aspects of electron emission in terms of the global number N_{esc} . It is possible to extract more information from experiment by recording in detail the kinetic energy spectra (KES) of the emitted electrons. This has been done for one-photon processes in negatively charged clusters in [169,5] and with multi-photon processes for positively charged Na clusters

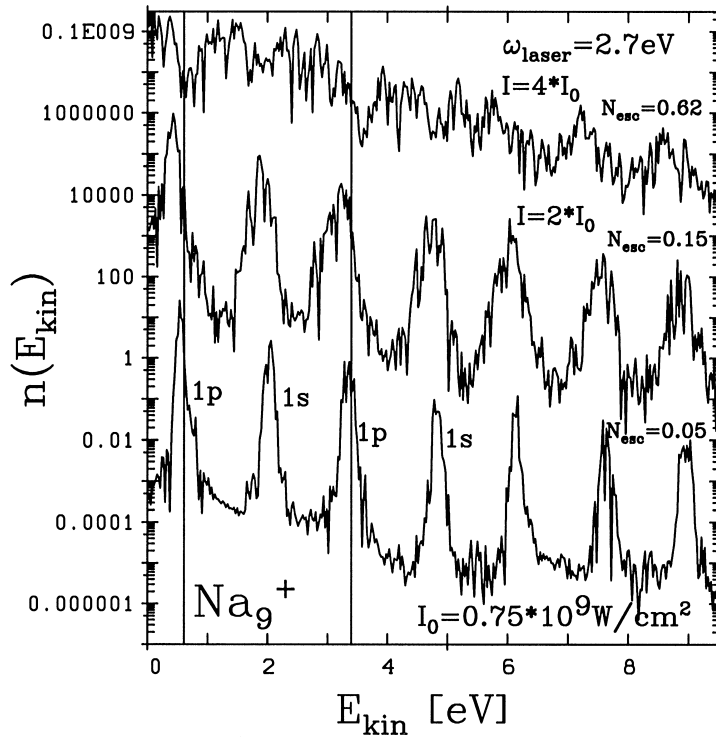


Fig. 29. Kinetic energy spectrum of emitted electrons for Na_9^+ in CAPS 144 configuration irradiated with a laser of frequency $\omega_{\text{laser}} = 2.7 \text{ eV}$ and varying intensity as indicated. The laser used a \cos^2 pulse with FWHM = 50 fs. The single-particle levels (1p or 1s) from which the electron are emitted are indicated for some of the peaks. The calculations have been done with TDLDA-SIC in the GAM approximation, Eq. (16).

[170] as well as Ag clusters on a substrate [171]. Theoretical investigations of the multi-photon case have just started [211]. The KES critically depend on the correct ionization energies. One thus has to employ an extended TDLDA with SIC (see Section 7.3). It suffices to do that in a globally averaged approximation [211,91]. Fig. 29 shows a typical result for the test case Na_9^+ and for three different intensities I . The lowest intensity nicely displays a series of well separated peaks. The laser frequency is indicated in the plot and we see that the structure is repeated in distances of ω_{laser} . There are two peaks within each such interval. These can be associated with emission from the 1p state and from the 1s state as indicated. The energetic separation of these two peaks precisely matches the difference of the single-electron energies. The emission threshold lies at 7.4 eV. A minimum of three photons with ω_{laser} are thus required to release an electron, which leads to a first peak at $E_{\text{kin}} = \nu\omega_{\text{laser}} - E_{\text{thr}} = 3 \times 2.7 \text{ eV} - 7.4 \text{ eV} = 0.7 \text{ eV}$, as can be seen from Fig. 29. The next interval is filled by four-photon processes, and so on. The peak height shrinks very quickly with the photon order ν , which is another way to look at the I^ν law. Altogether, these clear spectral relations suggest that KES could be used as a tool to explore single-electron energies in clusters.

However, this clean picture gets rapidly blurred with increasing intensity I . A factor of two in intensity already smears out the peaks to the edge of detectability. One more factor of two wipes

out any structure and leaves the pattern of exponential decrease as if one were seeing thermalized electrons with $T \sim 1$ eV. The reason can be deduced from the N_{esc} indicated at each curve. The clean case at lowest intensity has very small emission. This leaves the system almost unperturbed and allows access to the ground state spectra. But N_{esc} grows dramatically with intensity according to the I^ν law (here with $\nu = 3$). The highest intensity case indeed emits almost one electron. This leaves the residual cluster with that much additional charge, and this extra charge changes the Kohn–Sham field of the cluster far beyond the perturbative level. For example, the total binding is increased by about $N_{\text{esc}}e^2/R$, where R is the cluster radius. As the perturbation builds up in the course of time, the emission threshold gradually sinks by that amount. This stretches the peaks over a broad energy band and finally wipes out any structures. These considerations show that KES are plagued by conflicting requirements. To keep the perturbation small, one needs to work at sufficiently low intensity, which means low N_{esc} . But to gather enough statistics requires to produce enough electrons and thus not too low N_{esc} . An appropriate working point has to be found as a compromise.

Additional perturbation comes into play if finite temperatures are considered. Thermal motion of the ionic background is another source for smearing the spectra. It has been worked out in [211] that the step from 0 to 100 K temperature already causes large thermal broadening, and only little more is added when proceeding to, e.g., 400 K. This adds another condition on the experimental setup. Clusters should be kept very cold (safely below 100 K) if one wants to achieve sufficient resolution.

The experimental findings are puzzling. The study of KES with free Na_{93}^+ clusters in [170] did not discover any structures, whereas the results from [171] obtained from large Ag cluster deposited on a surface display nicely the band heads. It is argued in [170] that the lack of structures comes from a fast and almost complete thermalization of the electron cloud, which is conceivable because Na_{93}^+ is near the maximum of Landau damping, see Section 5.2.2. This needs yet to be investigated more systematically. Nonetheless, the present preliminary TDLDA calculations give already a hint on the desirable conditions for observing single-particle structures in KES from multiphoton processes. The temperature should stay safely below 100 K to avoid thermal perturbation. The average electron yield should be kept small, at about 0.01 electron per cluster, to maintain the spectral resolution. And one should preferably use a small cluster where damping is much suppressed by quantal effects and where the single-particle spectrum is less dense such that it can be more easily resolved. Finally, one can take advantage of directional information. Direct emission sends electrons preferably along laser polarization, whereas the competing thermal evaporation produces isotropic flow. Although this is a long list of quite demanding requirements, the expected output of nicely resolved single-particle energies will certainly justify investing this experimental effort.

7.5. VUU

As already discussed at several places in this paper, TDLDA is a mean field theory which needs to be complemented by electron–electron collisions in highly dissipative cases. We have seen in Section 6.4 that during collisions with highly charged, rapid ions, electron–electron correlations play only a minor role in the entrance channel of the reaction. They become active only after electron emission and Landau damping have opened phase space for the collision, a process which

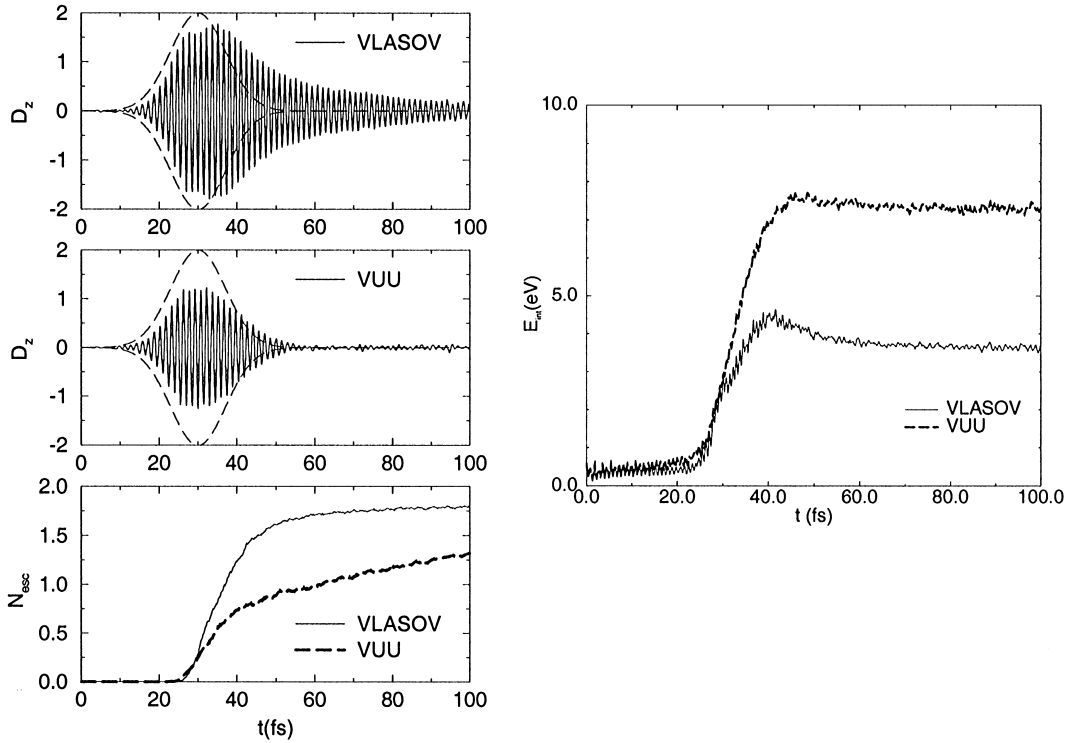


Fig. 30. Left part: Dipole signal along the direction of laser polarization (D_z , upper (Vlasov) and middle (VUU) panels) and number of emitted electrons (N_{esc} , lower part) as a function of time during the interaction of a femtosecond laser pulse with Na_9^+ (soft jellium). Right part: corresponding intrinsic energy E_{int} . The laser frequency and intensity are $\omega_{\text{laser}} = 2.75 \text{ eV}$ and $I = 6 \times 10^{11} \text{ W/cm}^2$, and the pulse envelope is indicated as a dashed line. Both Vlasov and VUU results are plotted for comparison. From [109].

is completed far beyond the reaction time with fast projectiles. The situation is much different in case of laser excitations. The laser pulses are usually longer (sometimes considerably) than the pulses delivered by rapid projectiles. And yet, the laser excitation is violent enough to drive the system beyond the adiabatic regime, because it delivers a continuous perturbation of the system. The relation of the time scales of electron–electron collisions to the times scales of the external excitation mechanism is thus quite different from the case of ionic collisions. We will explore this in the following.

We have seen above (Section 7.1) that the plasmon resonance plays a key role in the dynamics under laser irradiation. The closer the laser frequency to the Mie resonance, the larger the excitation. The impact of two-body collisions in the case of an off-resonance excitation has been explored in [109]. Only short pulses have been considered in these exploratory calculations and the dipole signal then dies out quickly after the pulse is over. It was found that electron–electron collisions leave direct ionization little affected. Differences build up only on longer times. We shall thus focus here on the case of an on-resonant excitation.

We consider in Fig. 30 a laser pulse (polarized along the z -axis), with a frequency matching the plasmon resonance in Na_9^+ ($\hbar\omega_{\text{laser}} \simeq 2.75 \text{ eV}$), and with intensity $I = 6 \times 10^{11} \text{ W/cm}^2$. The

resulting dipole $D_z(t)$ and ionization $N_{\text{esc}}(t)$ are shown in Fig. 30. During the first tens of femtoseconds ($t \lesssim 25$ fs) Vlasov and VUU perform the same; this is due to the fact that phase space for electron–electron collisions has not yet opened up. In both cases, the resonant response leads to a fast growth of plasmon oscillations. Patterns change beyond about 25 fs. While in the Vlasov calculations the amplitude continues to increase, it already decreases in VUU. The opening of phase space with growing dipole amplitude during the early phase of the irradiation has allowed electron–electron collisions to become active, and this causes the damping of the collective oscillation beyond 25 fs. This is confirmed by the intrinsic excitation energy, shown in the right part of Fig. 30. One clearly sees in this figure the extra intrinsic energy (with respect to Vlasov) generated by electron–electron collisions beyond $t > 25$ fs. In the VUU case, the energy provided by the laser is instantaneously thermalized by electron–electron collisions. Beyond $t = 40$ fs both Vlasov and VUU predict a damping of plasmon oscillations, although it is, not surprisingly, much faster in VUU, leaving no dipole signal after the end of the laser pulse. The effect is particularly large because of the high excitation energy (8 eV) and correspondingly high electronic temperature ($T \sim 1.3$ eV) stored in the system. This leads to a strong collisional damping because the collisional relaxation time in VUU scales with T^{-2} , see Eq. (1) and [23].

The time evolution of ionization also brings valuable complementing information, as can be seen from the lower panel of Fig. 30. The reduced amplitude of the dipole oscillation produces a reduced ionization. At $t = 60$ fs, i.e. at the end of the pulse, there is almost a factor 2 between Vlasov and VUU ionizations. However, for times beyond about 60 fs, thermal emission takes the lead in the VUU case. Emission stops in the Vlasov case because it has no mechanism for true thermalization, whereas the well thermalized and hot electron cloud of VUU nourishes a steadily continued thermal emission, eventually bringing the VUU result close to the Vlasov one (at least on the time scale investigated here). The effect of two-body collisions thus produces a “retarded” electron emission. The thermal energy is first accumulated during the irradiation itself, and later on released as electron evaporation. The difference has observable consequences on the angular distribution of emitted electrons. Direct electron emission is strongly peaked in the direction of laser polarization, whereas thermal evaporation produces isotropic output. Measuring the angular distribution would thus help to discriminate between these both processes. Further consequences will show up in the subsequent ionic motion and fragmentation of the cluster. This requires, however, to pursue the dynamical evolution much beyond the 100 fs scanned here. Systematic explorations of such effects have yet to come.

The conclusions on the role of electron–electron collisions in the above discussed example have been corroborated by a few more calculations performed with varying laser parameters. Electron–electron collisions accelerate the decay of plasmon oscillations and reduce direct electron emission during laser irradiation, postponing part of the ionization to later thermal evaporation. The effect is the more pronounced the closer the laser frequency comes to the Mie resonance. This once again emphasizes the key role played by this resonance in the physics of laser irradiation of metal clusters.

7.6. The search for anharmonic effects

By its very nature, a laser excitation carries a well-defined frequency which probes the spectral properties of a system at the same frequency. In the linear regime of excitations, the dipole

response $D(t)$ of the cluster is harmonic and proportional to the laser field E_0 . The proportionality constant is just the coefficient of linear (dynamical) polarizability α_1 , i.e. $D(t) = \Re\{\alpha_1(\omega_{\text{laser}})E_0 \exp(-i\omega_{\text{laser}}t)\} \mathbf{u}$. But nonlinear effects couple to sidebands of multiple frequencies and thus higher harmonics $\propto \exp(-in\omega_{\text{laser}}t)$ appear in the dipole signal. The first sideband to be considered lies at double frequency and is known as second harmonic generation (SHG). SHG is a standard tool used for frequency doubling of laser beams with particularly suited crystals. But SHG also offers a direct clue to the amount of nonlinearity exhibited by the response of the irradiated system (and higher harmonics explore even higher nonlinearities). It has actually been studied along this line, for large metal clusters attached to a surface [212]. We shall consider here as a tractable example the case of a small metal cluster attached to an insulating surface. Such deformed clusters (see Section 5.1.2) exhibit the necessary amount of symmetry breaking for an efficient excitation of SHG. Indeed, it is a well-known theoretical fact, confirmed by exploratory calculations, that a broken reflection symmetry is a key ingredient to ensure generation of even harmonics [165,213].

In the case of metal clusters, an arbitrary laser frequency will not necessarily lead to a pronounced SHG. Not surprisingly, the plasmon resonance ω_{pl} again plays a key role here. Analytical estimates show that sizable SHG is attained when ω_{pl} enters the excitation process at some end of the process, either by shining at the cluster with $\omega_{\text{laser}} = \omega_{\text{pl}}$ (SHG “out of the resonance”), or by placing the second harmonics at $2\omega_{\text{laser}} = \omega_{\text{pl}}$ (SHG “into resonance”). Both options have been tested on selected examples in [165,213], showing that indeed a strong SHG signal is produced in both cases, with differences in the details. The “into resonance” option turns out to be preferable because of a better suppression of background noise. We shall thus focus on this case here.

We consider the simple example of a Na_8 cluster deposited on a NaCl surface. As already discussed in Section 5.1.2, this cluster has a flat 2D ground state, and a close 3D isomer. Both exhibit clear SHG signals because of their sufficiently large symmetry breaking in direction orthogonal to the interface. Here, we apply on the 3D isomer a laser pulse of 50 fs duration, switched by a ramp of 5 fs at the beginning and the end. The laser frequency is 1.36 eV, which corresponds to exactly half the plasmon frequency along the polarization axis of the laser (chosen here perpendicular to the surface). The case of an irradiation with a laser polarized along the principal axes of the surface has also been investigated in [214]. From all cases considered, the general trend emerges that the polarization perpendicular to the surface is preferable in terms of efficiency for producing clean SHG signals. This is particularly noteworthy for the 2D ground state of Na_8 on NaCl, for which the influence of the surface is obviously large. In the case of the 3D isomer, which has kept a memory of the sphericity of the free Na_8 cluster, the effect is less pronounced, but still present.

As usual, we perform a standard spectral analysis based on the Fourier transform of the dipole response (see Section 4). The obtained power spectra for three laser intensities are displayed in Fig. 31 in the case of the deposited 3D isomer. The plotted power spectra are the ones along the axis perpendicular to the surface, i.e. along laser polarization. There is of course some cross talk into the other directions (parallel to the surface), and SHG is also observed along these axes. But the absolute intensity of these signals is much smaller than along the polarization axis and we thus restrict our analysis to this direction. Calculations have been performed at three different laser intensities, as indicated in the figure. For all three intensities several harmonics can be clearly identified. Of course, the higher the harmonics, the smaller the signal. Still, four secondary peaks

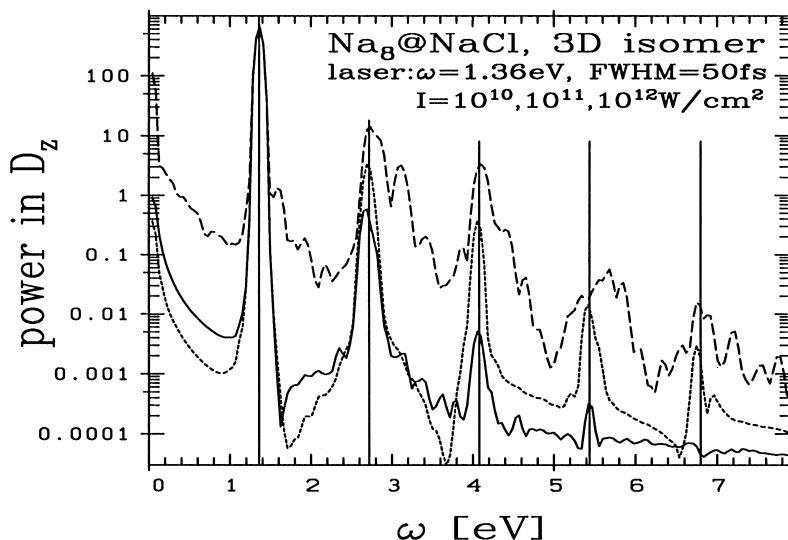


Fig. 31. SHG response of a Na_8 deposited on an insulating NaCl surface (3D isomer, Section 5.1.2). The laser frequency and pulse length are indicated in the figure, as well as the various intensities used. The laser is polarized along a direction perpendicular to the surface and the response is measured along the same direction. From [214].

are clearly visible in the most favorable case. It should be noted that the SHG signal obviously strongly depends on the laser intensity. The low-intensity case ($I = 10^{10}\text{ W/cm}^2$) leads to rather clear signals but with small peaks over the background as compared to the intermediate intensity case ($I = 10^{11}\text{ W/cm}^2$). In turn, at even higher intensity ($I = 10^{12}\text{ W/cm}^2$), the signal is obviously very noisy. The laser perturbs the system too much in that case and the associated ionization smears out the SHG signal.

Our TDLDA approach thus allows us to analyze SHG as produced from simple deposited clusters, a situation not so different from ongoing experiments [212]. We have seen that the choice of laser parameters is crucial for the production of clean SHG signals. More investigations of SHG are underway and are expected to shed more light on these conditions.

7.7. Coupling to ionic motion

The long time scales associated with ionic motion make ionic dynamics play a secondary role in most of the above discussions. For example, in the case of excitations by fast ionic projectiles (Section 6), there is no coupling between the excitation process and ionic degrees of freedom. Of course electronic excitation will, long after the excitation process itself, couple to ionic degrees of freedom. But by that time, the system would have forgotten about the details of the excitation process. The situation is quite different in the case of lasers, for which even high-intensity pulses can last for more than 100fs. As we shall see in detail below, there is actually an explicit coupling between laser and ions for pulses beyond a few hundreds of fs, and this coupling turns out to play a crucial role, even at the level of the electronic response. Before attacking this question, we would first like to consider the case of a short pulse and examine the impact of laser frequency on ionic motion.

7.7.1. Impact of laser frequency on ionic explosion

As a first illustration of the interplay between lasers and ionic motion, we focus on the case of an indirect coupling mediated via the electrons. We consider here the case of the Coulomb explosion of a Na_{12} cluster. The initially neutral cluster is excited by a short Gaussian laser pulse of 50 fs FWHM. The laser intensity and frequency are tuned so that about three electrons are directly emitted (recall that TDLDA does not quantize the number of emitted electrons). This leads to an electronically excited Na_{12}^{3+} cluster which then undergoes Coulomb fragmentation. We compare two different excitations, varying laser intensity and frequency, but leading to the same ionized cluster. The first test case corresponds to an off-resonant excitation at intensity $I = 4.9 \times 10^{12} \text{ W/cm}^2$ and with a frequency $\omega_{\text{laser}} = 6.58 \text{ eV}$. This is about twice the plasmon frequency and corresponds to an energy above the electron emission threshold. As a consequence, direct electron emission is easy, and proceeds without a large storage of excitation energy in the system. The frequency $\omega_{\text{laser}} = 3.06 \text{ eV}$ of the second case is, in turn, close to the plasmon frequency. Consequently, one needs much less intensity, $I = 4.3 \times 10^{11} \text{ W/cm}^2$, to attain the same charge state (Section 7.1).

At the end of the laser excitation we are thus left with an excited Na_{12}^{3+} cluster. Note that all symmetries of the electron cloud have been broken at this stage, as we have polarized the laser along the main diagonal of the principal cluster axis. It should also be noted here that the excitation process is truly nonadiabatic in this case. Indeed, an evaluation of the electronic excitation energy shows that a sizable amount has been stored in the system, in both cases. This means that a Born–Oppenheimer treatment would be inappropriate. One may argue that the electronic excitation could relax quickly enough to validate again a Born–Oppenheimer picture at some (hopefully not too late) instant. However, our calculations show that is not the case [68] and that it is not possible to match a Born–Oppenheimer dynamics at any later stage. The motion hence remains truly nonadiabatic over the investigated time.

Fig. 32 displays snapshots of the ionic and electronic density for both test cases at $t = 457 \text{ fs}$ and already shows how different both time evolutions are. The on-resonant excitation (upper part) starts with higher intrinsic excitation and continues with faster explosion as compared to the off-resonant excitation (lower part). The nature of the explosion itself is different. In the on-resonant case the Coulomb explosion seems to favor monomer emission. The situation is different in the off-resonant case (see Fig. 32), in which naked ions are preferentially produced.

During the first phase ($t \lesssim 100 \text{ fs}$), which basically fixes the electronic initial conditions, ions have not yet moved. However, beyond about 100 fs, one observes a rapid switching on of the ionic degrees of freedom. This coupling takes place at a time at which the electronic excitation is far from having subsided, and this is the reason why a matching with a Born–Oppenheimer surface is impossible. The switching-on of the ionic degrees of freedom in fact reflects the combined effects of (i) the onset of Coulomb “explosion” resulting from the high charge state of the system; (ii) the transfer of part of the available electronic excitation energy to ionic motion. The next stage of the evolution thus starts after about 100 fs. Although the two cases evolve somewhat similarly for some time, a dramatic difference enters around 500 fs (see Fig. 32). These differences in the ionic deexcitation are to be attributed to the differences between the two excitation mechanisms, in particular the way the excitation has been preferentially deposited, in bulk or in surface.

The comparison of these two cases, although exploratory (keep in mind that quantitative conclusions on fragmentation patterns could only be reached with statistical ensembles of

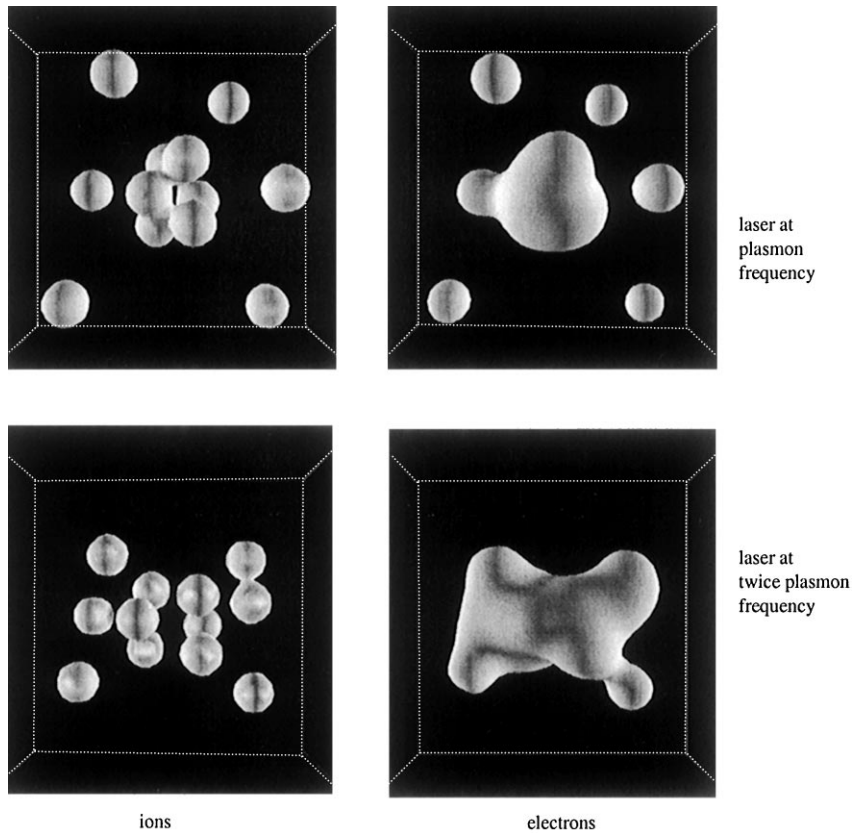


Fig. 32. Electronic isodensity surfaces (on the right panels), for a density of $1.44 \times 10^{-3} a_0^{-3}$, obtained in the simulations of irradiation of Na_{12} by two lasers (see text) at time $t = 457$ fs. Corresponding isosurfaces for the ionic pseudodensities (i.e. the densities one can associate to the pseudopotential through the Poisson equation) are shown on the left panel. The top part of the figure corresponds to the case where the laser pulse used has a frequency $\omega_{\text{laser}} = 3.05$ eV close to the plasmon frequency of the cluster; the lower part corresponds to a case where the laser pulse has a frequency $\omega_{\text{laser}} = 6.58$ eV.

fragmenting events), has demonstrated that very different dynamical scenarios can be reached by tuning the (electronic) excitation process. We have also seen that the coupling between the electronic degrees of freedom (in which the excitation has been primarily deposited) and the ionic degrees of freedom takes place on a surprisingly short time scale, at a time at which the electron cloud remains far from being relaxed on the Born–Oppenheimer surface. This emphasizes, once more, the crucial importance of nonadiabatic effects in the physical situations we consider here.

7.7.2. Direct coupling between ionic motion and laser

In Section 7.7.1 we have considered a case in which the influence of the laser on ionic dynamics was mediated by electrons. This is typical for a situation corresponding to a short laser pulse, during which ions have no time to move. In such cases, it is the net charge acquired by the cluster during the pulse, together with the excitation energy deposited in the electron cloud, which are responsible for ionic explosion on a time beyond about 100 fs. But in the case of a high cluster

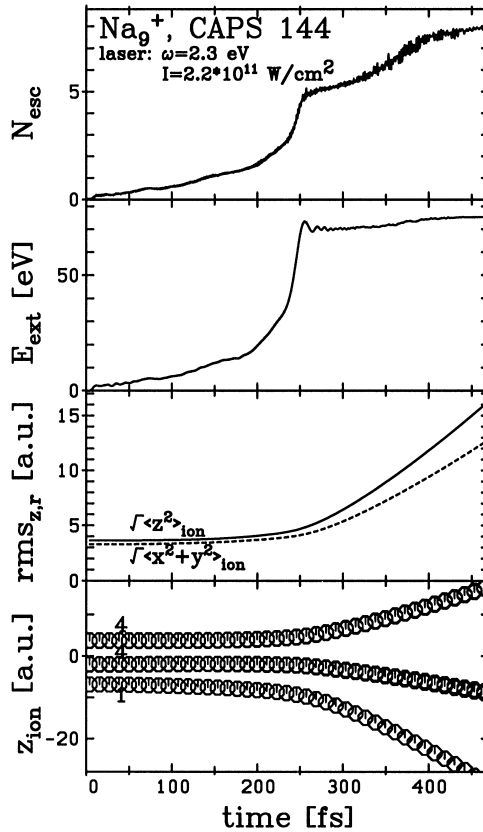


Fig. 33. Time evolution of basic observables for Na_9^+ irradiated with a laser with frequency $\omega = 2.3 \text{ eV}$, intensity $I = 2.2 \times 10^{11} \text{ W/cm}^2$ and a ramp pulse of length 500 fs with 50 fs switching time at both ends. The cluster was initialized in the CAPS ground state. Coupled ionic and electronic dynamics were propagated. The uppermost panel shows the number of emitted electrons. The second panel shows the energy absorbed by the cluster from the laser beam. The third panel shows the mean-square extension of the ionic distribution along the z -axis (along laser polarization axis) and in radial direction. The lowest panel displays the ionic positions along the z -axis.

ionization, it is possible to observe a direct interference of ionic motion and the laser pulse. In this section, we explore this aspect taking an example in which ionic expansion drives the system into electronic resonance, which enhances ionization and boosts the ionic explosion. The test case is modeled after the experiments with Pt clusters [71], here using Na because it is simpler to handle theoretically. The results point out the importance of ionic effects in ionization for the case of long pulses. They could also provide a clue to the experimental puzzle of explaining the high ionization states attained in clusters irradiated by intense lasers [13] and the role of pulse duration in this ionic process [71]. Indeed, ionic motion changes the resonance conditions (see also Fig. 9) which, in turn, has a large impact on the dynamical evolution of both electrons and ions.

We take the example of a low-frequency laser irradiating Na_9^+ . The laser field is chosen to have a frequency of $\omega_{\text{laser}} = 2.3 \text{ eV}$, well below the plasmon resonance for this cluster, an intensity $I = 2.2 \times 10^{11} \text{ W/cm}^2$ and a ramp pulse of length 500 fs. Results are displayed in Fig. 33 for

characteristic observables of both electronic and ionic degrees of freedom. Initially, very little happens, which is expected for such an off-resonant case at moderate intensity. One detects a slow growth of ionization (upper panel) together with a slow absorption of external energy E_{ext} from the beam (second upper panel), but both effects remain moderate. Nevertheless, this continuous ionization is crucial. In fact it has two competing effects, one on ions, the other on electrons. As can be seen from Fig. 9, ionization leads to a blue shift of the plasmon resonance at fixed ionic configuration, which is a typical electronic effect. But ionization also leads to a slow expansion and elongation of the ionic configuration due to Coulomb pressure (see the lower two panels of Fig. 33) which, in turn, lowers the plasmon peak (note that expansion and elongation amounts to increasing the Wigner–Seitz radius of the cluster, which implies a decrease of the plasmon resonance, see Fig. 11). Finally, at about 250 fs the electron cloud comes into resonance with the laser beam, which produces a dramatic effect (Section 7.2.1). One observes a sudden increase in absorbed energy (second panel from above), from which a large portion is converted into direct electron emission. This enhances ionization and drives Coulomb explosion further. It is interesting to note how quick all this happens (typically within less than 10 fs). The further evolution of the system is less surprising: energy absorption dies down, while some delayed electron emission remains (probably thermal evaporation from the very hot cluster), and the ions separate at a rather fast time scale because of the huge accumulated charge of the cluster. Of course, this example proceeds in a particularly dramatic fashion, because of the particular set of laser parameters chosen, and other cases might evolve in a more gentle way. It is nevertheless striking to see the role played by the ionic degrees of freedom in this case, driving the system towards electronic resonance with the laser and thus boosting the Coulomb explosion.

This example is only one of the many dynamical evolutions which can be arranged by appropriate tuning of the laser parameters. Other scenarios are conceivable where the cluster is going through resonant conditions several times [215]. The rich landscape of laser parameters opens up here a world of different scenarios yet to be explored.

8. Conclusions and perspectives

This review was aimed to provide a summary of recent studies on the dynamics of metal clusters, accounting for electronic as well as ionic dynamics in all regimes from faint small amplitude oscillations up to the most violent processes amongst the valence electrons. The theoretical tools for this demanding task are still under development. But for the time being, the bulk of the investigations used the time-dependent local-density approximation (TDLDA) as a robust and efficient workhorse. This served very well to explore an abundance of dynamical scenarios triggered by highly charged ions passing by a cluster or by strong pulses from femtosecond lasers. One of the key results of these TDLDA explorations is that one can condense the many studies under varying conditions into a simple and general recipe for estimating the time scales of the different mechanisms appearing in violent cluster dynamics. One can sort out a hierarchy of mechanisms and times, starting with the shortest times for the plasmon oscillations (1.5 fs), followed by the still short times for direct electron emission and Landau damping (2–10 fs). The two latter processes open phase space for electron–electron collisions which lead to relaxation times between 5 and 100 fs (strongly depending on temperature). The slowest electronic process is then thermal electron

evaporation which resides usually in the far picosecond (ps) range, but can come down below 100 fs for very hot electron clouds. Ions start to play a role from 100 fs on. A full ionic cycle takes about 250 fs, Coulomb explosion about 500 fs to 1 ps, and ionic thermalization with subsequent fragmentation comes much later.

Former investigations mainly used the TDLDA in the linear regime to investigate the electronic spectra of metal clusters as they are observed in photo-absorption experiments with nanosecond lasers. This line of research is still actively pursued, but now heading for the more demanding situations such as detailed ionic structure effects in nonsimple metals (e.g. Ag) or other materials. And, of course, a careful analysis of the spectral properties of a given cluster remains always the first step before starting any large-scale exploration of nonlinear dynamics.

Just beyond the linear regime lies a transient regime of moderately nonlinear effects where one does still have the linear spectrum as (slightly perturbed) guideline and where one can sort the processes according to the number of photons or plasmons excited. This is the regime where, for example, second-harmonic generation (SHG) is studied. We have shown that TDLDA is well adapted to describe SHG or higher harmonics. It gives a pertinent picture of the typical processes, conditions and limits. The practical problem is here that SHG requires symmetry breaking and that experiments are done with huge clusters on a surface. It is thus still some way ahead before one can attack a detailed comparison of fully fledged TDLDA calculations with existing experiments. A process which does already exist in the linear regime is field amplification. But when aiming to produce ever larger local fields one quickly enters the nonlinear domain. TDLDA can nicely reproduce field amplification in all regimes and it demonstrates also very clearly that this process loses its strength with increasing violence of the excitation, because an intact plasmon response is required to supply amplification. Last not least, in the transient regime, a detailed study of the kinetic energy spectra of emitted electrons is possible in connection with above-threshold ionization. TDLDA (here necessarily with self-interaction corrections) disentangles nicely the multi-photon processes and single-particle states involved. This process offers the chance to measure indirectly the energies of the single-electron states in the clusters. The experimental situation is still ambiguous in that respect. Further development of theory (dissipation by electron collisions) and more detailed experiments are needed to make it more conclusive.

The fully fledged TDLDA is also the ideal tool to study the details of a given excitation process. In this review, we have concentrated on the two leading mechanisms, laser pulses and Coulomb excitation through a highly charged ion passing by. The latter process is fast as compared to any other time scale in the clusters. It thus serves to set a well-defined clock in the theoretical studies, and that is a decisive feature to disentangle the various time scales. The practical relevance of highly charged ions is that they can ionize a cluster to high charge states while leaving little internal excitation in the remaining cluster (as compared for example to nanosecond lasers). The TDLDA calculations confirm that feature. Time scales are more mixed up by femtosecond laser pulses. But they, in turn, provide access to a much richer world of possible scenarios. Frequency, intensity, pulse length and pulse shape all play a role for determining the actual dynamical evolution. This becomes particularly interesting when considering coupled ionic and electronic motion over long time spans (above 100 fs). We have found in several examples that the subsequent ionic evolution sensitively depends on the initial laser parameters. For example, we have shown in the example of Na_{12} that the final outcome of a Coulomb explosion can strongly depend on the laser frequency (on or off resonance). There can also be enhanced ionization triggered by ionic motion (if the laser

pulse lasts long enough to capture that effect). And last not least, we have observed that femtosecond lasers are also able to generate high ionization while leaving little residual excitation in the system. The trends are found to differ systematically from the ionization through highly charged ions. Here is a point where further TDLDA studies could help in experimental decisions on the best working point for either mechanism.

Quantum effects fade away in violent excitations. For then, one can invoke Vlasov-LDA as semi-classical approximation to TDLDA. In fact, many of the above quoted results on ionization and excitation mechanisms have been obtained or corroborated by Vlasov-LDA. The approach offers the additional chance to go beyond TDLDA and to include dynamical effects of electron–electron correlations by adding an Ühling–Uhlenbeck collision term. This leads to the VUU approach which serves as a unique tool to disentangle the various dissipation mechanisms in a cluster, direct electron emission, Landau damping, and collisional thermalization. The relaxation time for collisional thermalization was found to depend strongly on the internal excitation energy in accordance with the theory of Landau-liquids. The importance of thermalization thus depends very much on the actual dynamics, and one should, in principle, include a collision term in each large-scale dynamical calculation. This is, however, a very high demand. Simplifications need yet to be worked out which would allow one to run thermalization in a more routine manner.

Several paragraphs in this conclusion have naturally led to open ends where future developments have to continue. Let us briefly summarize them here. The rich world of scenarios in connection with femtosecond laser pulses needs further exploration. The goal would be to condense the huge amount of information into a handful of simple recipes for estimating an expected outcome. Measuring processes (e.g. kinetic energy spectra or SHG) need yet to be worked out in more detail. An extension to materials other than simple metals is also highly necessary. In particular, the interplay in the course of violent dynamical processes between truly delocalized valence electrons and (loosely bound) core electrons gives rise to a whole range of new effects (e.g. dynamical metallization). These goals can be reached with moderate extensions of existing TDLDA schemes. But TDLDA as such is a tool which deserves further critical inspection and development. We need manageable ways of going beyond TDLDA and there are several directions for it: self-interaction corrections, gradient corrections, dynamical correlations (Markovian collisions as well as non-Markovian effects). A far reaching goal, which comes up in connection with dissipation, is for example the handling of the associated fluctuations for which one needs to develop a stochastic theory for an ensemble of Kohn–Sham fields.

Acknowledgements

The authors are glad to acknowledge fruitful and inspiring discussions with Y. Abe, G.F. Bertsch, M. Brack, A. Doms, Ch. Ellert, C. Guet, H. Haberland, S. Kümmel, Ch. Kohl, M. Schmidt and F. Spiegelmann. The authors furthermore thank Institut Universitaire de France for financial support and invitation, as well as the French-German programs PROCOPE (numbers 95073 and 99072) which allowed a continued stream of exchanges between Toulouse and Erlangen. Finally, the French IDRIS and CNUSC computing centers are thanked for extensive use of their computational facilities.

References

- [1] W.D. Knight, K. Clemenger, W.A. de Heer, W.A. Saunders, M.Y. Chou, M.L. Cohen, *Phys. Rev. Lett.* 52 (1984) 2141.
- [2] W.D. Knight, K. Clemenger, W.A. de Heer, W.A. Saunders, *Phys. Rev. B* 31 (1985) 2539.
- [3] W. Ekardt, *Phys. Rev. Lett.* 52 (1984) 1925.
- [4] D.E. Beck, *Solid State Commun.* 49 (1984) 381.
- [5] W.A. de Heer, *Rev. Mod. Phys.* 65 (1993) 611.
- [6] M. Brack, *Rev. Mod. Phys.* 65 (1993) 677.
- [7] V.B. Koutecký, P. Fantucci, J. Koutecký, *Chem. Rev.* 91 (1991) 1035.
- [8] U. Kreibig, M. Vollmer, *Optical Properties of Metal Clusters*, Vol. 25, Springer Series in Materials Science, Springer, Berlin, 1993.
- [9] H. Haberland (Ed.), *Clusters of Atoms and Molecules 1 – Theory, Experiment, and Clusters of Atoms*, Vol. 52, Springer Series in Chemical Physics, Springer, Berlin, 1994.
- [10] C. Bréchnignac, P. Cahuzac, *Comments, At. Mol. Phys.* 31 (1995).
- [11] W. Ekardt (Ed.), *Metal Clusters*, Wiley, Chichester, UK, 1999.
- [12] F. Chandezon, C. Guet, B.A. Huber, D. Jalabert, M. Maurel, E. Monnard, C. Ristori, J.C. Rocco, *Phys. Rev. Lett.* 74 (1995) 3784.
- [13] T. Ditmire, J.W.G. Tisch, E. Springate, M.B. Mason, N. Hay, R.A. Smith, J. Marangos, M.H.R. Hutchinson, *Nature* 386 (1997) 54.
- [14] K. Ertel et al., preprint, 1999.
- [15] H. Hohmann, C. Callegari, S. Furrer, D. Grosenick, E.E.B. Campbell, I.V. Hertel, *Phys. Rev. Lett.* 73 (1994) 1919.
- [16] F. Calvayrac, P.-G. Reinhard, E. Suraud, *Phys. Rev. B* 52 (1995) R17056.
- [17] K. Yabana, G.F. Bertsch, *Phys. Rev. B* 54 (1996) 4484.
- [18] F. Calvayrac, P.-G. Reinhard, E. Suraud, *Ann. Phys. (NY)* 255 (1997) 125.
- [19] P.-G. Reinhard, E. Suraud, *J. Clust. Sci.* 10 (1999) 239.
- [20] M. Gross, C. Guet, *Z. Phys. D* 33 (1995) 289.
- [21] L. Feret, E. Suraud, F. Calvayrac, P.-G. Reinhard, *J. Phys. B* 29 (1996) 4477.
- [22] A. Doms, A.-S. Krepper, V. Savalli, P.-G. Reinhard, E. Suraud, *Ann. Phys. (Leipzig)* 6 (1997) 468.
- [23] A. Doms, P.-G. Reinhard, E. Suraud, *Phys. Rev. Lett.* 81 (1998) 5524.
- [24] G. Mie, *Ann. Phys. (Leipzig)* 25 (1908) 377.
- [25] E.M. Lifschitz, L.P. Pitajewski, *Physikalische Kinetik, Lehrbuch der Theoretischen Physik*, Vol. X, Mir, Moscow, 1988.
- [26] D. Pines, P. Nozières, *The Theory of Quantum Liquids*, Benjamin, New York, 1966.
- [27] V. Weisskopf, *Phys. Rev.* 52 (1937) 295.
- [28] J. Teilhaber, B.J. Alder, *Phys. Rev. A* 43 (1991) 4143.
- [29] D.M. Ceperley, B.J. Alder, *Phys. Rev. Lett.* 45 (1980) 566.
- [30] R.O. Jones, O. Gunnarsson, *Rev. Mod. Phys.* 61 (1989) 689.
- [31] R.M. Dreizler, E.K.U. Gross, *Density Functional Theory: An Approach to the Quantum Many-Body Problem*, Springer, Berlin, 1990.
- [32] D.C. Langreth, M.J. Mehl, *Phys. Rev. B* 28 (1983) 1809.
- [33] A.D. Becke, *Phys. Rev. A* 38 (1988) 3098.
- [34] J.P. Perdew, K. Burke, M. Ernzerhof, *Phys. Rev. Lett.* 77 (1996) 3865.
- [35] J.P. Perdew, A. Zunger, *Phys. Rev. B* 23 (1981) 5048.
- [36] K. Clemenger, *Phys. Rev. B* 32 (1985) 1359.
- [37] C. Yannouleas, U. Landman, *Phys. Rev. B* 51 (1995) 1902.
- [38] S.M. Reimann, S. Frauendorf, M. Brack, *Z. Phys. D* 34 (1995) 125.
- [39] S.M. Reimann, M. Koskinen, H. Haekinnen, P.E. Lindelof, M. Manninen, *Phys. Rev. B* 56 (1997) 12147.
- [40] F. Spiegelmann, R. Poteau, *Comments, At. Mol. Phys.* 31 (1995) 395.
- [41] S. Chelkowski, C. Foisy, A.D. Bandrauk, *Phys. Rev. A* 57 (1999) 1176.
- [42] L. Szasz, *Pseudopotential Theory of Atoms and Molecules*, Wiley, New York, 1985.

- [43] W.A. Harrison, *Pseudopotentials in the Theory of Metals*, Benjamin, New York, 1976.
- [44] I. Moullet, J.L. Martins, F. Reuse, J. Buttet, *Phys. Rev. Lett.* 65 (1990) 476.
- [45] U. Röthlisberger, W. Andreoni, *J. Chem. Phys.* 94 (1991) 8129.
- [46] H. Häkkinen, R.N. Barnett, U. Landman, *Europhys. Lett.* 28 (1994) 263.
- [47] J. Borstel, U. Lammers, A. Mananes, J.A. Alonso, *Lecture Notes in Physics*, Vol. 404, 1992, pp. 327.
- [48] S.A. Blundell, C. Guet, *Z. Phys. D* 28 (1993) 81.
- [49] B. Montag, P.-G. Reinhard, J. Meyer, *Z. Phys. D* 32 (1994) 125.
- [50] B. Montag, P.-G. Reinhard, *Phys. Lett. A* 193 (1994) 380.
- [51] B. Montag, P.-G. Reinhard, *Z. Phys. D* 33 (1995) 265.
- [52] J.P. Perdew, H.Q. Tran, E.D. Smith, *Phys. Rev. B* 42 (1990) 11 627.
- [53] M. Seidl, M. Brack, *Ann. Phys. (NY)* 245 (1996) 275.
- [54] F. Spiegelmann, R. Poteau, B. Montag, P.-G. Reinhard, *Phys. Lett. A* 242 (1998) 163.
- [55] R. Car, M. Parrinello, *Phys. Rev. Lett.* 55 (1985) 2471.
- [56] C. Kohl, P.-G. Reinhard, *Z. Phys. D* 39 (1997) 225.
- [57] F. Calvayrac, E. Suraud, P.-G. Reinhard, *J. Phys. B* 31 (1998) 1367.
- [58] S. Kümmel, M. Brack, P.G. Reinhard, *Euro. Phys. J. D* 9 (1999) 149.
- [59] L. Serra, A. Rubio, *Phys. Rev. Lett.* 78 (1997) 1428.
- [60] B. Montag, T. Hirschmann, J. Meyer, P.-G. Reinhard, M. Brack, *Phys. Rev. B* 52 (1995) 4775.
- [61] J. Parker, K.T. Taylor, C. Clark, S. Blodgett-Ford, *J. Phys. B* 29 (1996) L33.
- [62] E. Runge, E.K.U. Gross, *Phys. Rev. Lett.* 52 (1984) 997.
- [63] E.K.U. Gross, W. Kohn, *Adv. Quant. Chem.* 21 (1990) 255.
- [64] E.K.U. Gross, C.A. Ullrich, U.J. Gossmann, *Density Functional Theory*, NATO ASI Ser. B, Vol. 337, Plenum Press, New York, 1995, p. 149.
- [65] E.K.U. Gross, J.F. Dobson, M. Petersilka, *Top. Curr. Chem.* 181 (1996) 81.
- [66] U. Saalmann, R. Schmidt, *Z. Phys. D* 38 (1996) 153.
- [67] G. Vignale, C.A. Ullrich, S. Conti, *Phys. Rev. Lett.* 79 (1997) 4878.
- [68] F. Calvayrac, P.-G. Reinhard, E. Suraud, *J. Phys. B* 31 (1998) 5023.
- [69] R.N. Barnett, U. Landman, A. Nitzan, G. Rajagopal, *J. Chem. Phys.* 94 (1991) 608.
- [70] P. Blaise, S.A. Blundell, C. Guet, *Phys. Rev. B* 55 (1996) 15 856.
- [71] L. Köller, M. Schumacher, J. Köhn, S. Teuber, J. Tiggesbäumker, K.-H. Meiwes-Broer, *Phys. Rev. Lett.* 82 (1999) 3783.
- [72] L. Plagne, C. Guet, *Phys. Rev. A* 59 (1999) 4461.
- [73] A. Doms, P.-G. Reinhard, E. Suraud, *Phys. Rev. Lett.* 80 (1998) 5520.
- [74] C. Yannouleas, R.A. Broglia, *Phys. Rev. Lett.* 63 (1989) 255.
- [75] C. Yannouleas, R. Broglia, *Ann. Phys. (NY)* 217 (1992) 105.
- [76] P. Hohenberg, W. Kohn, *Phys. Rev.* 136 (1964) 864.
- [77] W. Kohn, L.J. Sham, *Phys. Rev.* 140 (1965) 1133.
- [78] O. Gunnarsson, B.I. Lundqvist, *Phys. Rev. B* 13 (1976) 4274.
- [79] J.P. Perdew, Y. Wang, *Phys. Rev. B* 45 (1992) 13 244.
- [80] H.G. Muller, M.V. Fedorov (Eds.), *Super-Intense Laser-Atom Physics IV*, Kluwer, Dordrecht, 1996.
- [81] C.A. Ullrich, E.K.U. Gross, *Comments, At. Mol. Phys.* 33 (1997) 211.
- [82] J.D. Talman, W.F. Shadwick, *Phys. Rev. A* 14 (1976) 36.
- [83] M.R. Norman, D.D. Koelling, *Phys. Rev. B* 30 (1984) 5530.
- [84] J.B. Krieger, Y. Li, G.J. Iafrate, *Phys. Rev. A* 45 (1992) 101.
- [85] T. Grabo, E.K.U. Gross, *Chem. Phys. Lett.* 240 (1995) 141.
- [86] T. Grabo, E.K.U. Gross, *Int. J. Quant. Chem.* 64 (1997) 95.
- [87] C.A. Ullrich, U.J. Gossmann, E.K.U. Gross, *Phys. Rev. Lett.* 74 (1995) 872.
- [88] J. Chen, J.B. Krieger, Y. Li, G.J. Iafrate, *pra* 54 (1996) 3939.
- [89] X.M. Tong, S.I. Chu, *Phys. Rev. A* 55 (1997) 3406.
- [90] C.A. Ullrich, P.-G. Reinhard, E. Suraud, *J. Phys. B* 31 (1998) 1871.
- [91] M.F. Politis, P.A. Hervieux, J. Hanssen, M.E. Madjet, F. Martin, *Phys. Rev. A* 58 (1998) 367.

- [92] C. Ullrich, P.-G. Reinhard, E. Suraud, preprint (2000).
- [93] S. Goedecker, M. Teter, J. Hutter, *Phys. Rev. B* 54 (1996) 1703.
- [94] C. Hartwigsen, S. Goedecker, J. Hutter, *Phys. Rev. B* 58 (1998) 3641.
- [95] K. Wohrer, M. Chabot, R. Fossé, D. Gardes, P.A. Hervieux, F. Calvayrac, P.-G. Reinhard, E. Suraud, *Nucl. Instr. and Meth. B* 146 (1998) 29.
- [96] C. Kohl, G.F. Bertsch, *Phys. Rev. B* 60 (1999) 4205.
- [97] N. Troullier, J.L. Martins, *Phys. Rev. B* 43 (1991) 1993.
- [98] K. Yabana, G.F. Bertsch, *Z. Phys. D* 42 (1997) 219.
- [99] S. Kuemmel, M. Brack, P.-G. Reinhard, *Phys. Rev. B* 58 (1998) R1774.
- [100] G.B. Bachelet, D.R. Hamann, M. Schlüter, *Phys. Rev. B* 26 (1982) 4199.
- [101] L. Verlet, *Phys. Rev.* 159 (1967) 98.
- [102] F. Calvayrac, P.-G. Reinhard, E. Suraud, *Euro. Phys. J. D* 9 (1999) 389.
- [103] N.W. Ashcroft, D.C. Langreth, *Phys. Rev.* 155 (1967) 682.
- [104] P.-G. Reinhard, S. Weisgerber, O. Genzken, M. Brack, *Lecture Notes in Physics*, Vol. 404, Springer, Berlin, 1992, pp. 254.
- [105] P.-G. Reinhard, S. Weisgerber, O. Genzken, M. Brack, *Z. Phys. A* 349 (1994) 219.
- [106] A. Rubio, L.C. Balbas, J.A. Alonso, *Z. Phys. D* 19 (1991) 93.
- [107] P.-G. Reinhard, O. Genzken, M. Brack, *Ann. Phys. (Leipzig)* 5 (1996) 1.
- [108] C.A. Ullrich, P.-G. Reinhard, E. Suraud, *Euro. Phys. J. D* 9 (1999) 407.
- [109] A. Doms, P.-G. Reinhard, E. Suraud, *Ann. Phys. (NY)* 280 (2000) 211.
- [110] A. Doms, P. L'Eplattenier, P.-G. Reinhard, E. Suraud, *Ann. Phys. (Leipzig)* 6 (1997) 455.
- [111] K. Takahashi, *Prog. Theor. Phys. Supp.* 98 (1989) 109.
- [112] P. L'Eplattenier, E. Suraud, P.-G. Reinhard, *Ann. Phys. (NY)* 224 (1995) 426.
- [113] P. L'Eplattenier, P.-G. Reinhard, E. Suraud, *J. Phys. A* 28 (1995) 787.
- [114] P.-G. Reinhard, E. Suraud, *Ann. Phys. (NY)* 239 (1995) 193, 216.
- [115] P.-G. Reinhard, E. Suraud, *Z. Phys. A* 355 (1996) 339.
- [116] A. Doms, P.-G. Reinhard, E. Suraud, *Ann. Phys. (NY)* 260 (1997) 171.
- [117] E. Giglio, P.-G. Reinhard, E. Suraud, *Comput. Mat. Sci.* (2000), to appear.
- [118] J. Clerouin, E.L. Pollock, G. Zerah, *Phys. Rev. A* 46 (1992) 5130.
- [119] A. Doms, E. Suraud, P.-G. Reinhard, *Eur. Phys. J.* 2 (1998) 191.
- [120] J.-P. Hansen, I.R. Mac Donald, *Theory of Simple Liquids*, Academic Press, London, 1976.
- [121] G.F. Bertsch, S. Das Gupta, *Phys. Rep.* 160 (1988) 190.
- [122] A. Bonasera, F. Gulminelli, J. Molitoris, *Phys. Rep.* 243 (1994) 1.
- [123] Y. Abe, S. Ayik, P.-G. Reinhard, E. Suraud, *Phys. Rep.* 275 (1996) 49.
- [124] K. Gütter, K. Wagner, P.-G. Reinhard, C. Toepffer, *Ann. Phys. (NY)* 225 (1993) 339.
- [125] S. Ichimaru, H. Iyetomi, S. Tanaka, *Phys. Rep.* 149 (1987) 91.
- [126] J.W. Serene, D. Rainer, *Phys. Rep.* 101 (1983) 221.
- [127] D. Pines, *Phys. Rev.* 92 (1953) 626.
- [128] M.J. Giannoni, D. Vautherin, M. Veneroni, D. Brink, *Phys. Lett. B* 63 (1976) 8.
- [129] M. Brewczyk, K. Rzazewski, C.W. Clark, *Phys. Rev. Lett.* 78 (1997) 191.
- [130] M. Brewczyk, C.W. Clark, M. Lewenstein, K. Rzazewski, *Phys. Rev. Lett.* 80 (1998) 1857.
- [131] M. Brewczyk, K. Rzazewski, *Phys. Rev. A* 60 (1999) 2285.
- [132] U. Saalmann, R. Schmidt, *Phys. Rev. Lett.* 80 (1998) 3213.
- [133] F. Calvayrac, *Ann. Phys. (Paris)* 23 (3) (1998) 1.
- [134] J.R. Chelikowsky, X. Jing, K. Wu, Y. Saad, *Phys. Rev. B* 53 (1996) 12071.
- [135] D. Bromley (Ed.), *Treatise of Heavy-Ion Science*, Vol. 3, Plenum Press, New York, 1985.
- [136] V. Blum, G. Lauritsch, J.A. Maruhn, P.-G. Reinhard, *J. Comput. Phys.* 100 (1992) 364.
- [137] G. Lauritsch, P.-G. Reinhard, *Int. J. Mod. Phys. C* 5 (1994) 65.
- [138] W.H. Press, S.A. Teukolsky, W.T. Vetterling, B.P. Flannery, *Numerical Recipes*, Cambridge University Press, Cambridge, 1992.
- [139] R.S. Varga, *Iterative Matrix Analysis*, Prentice-Hall, Englewood Cliffs, NJ, 1962.

- [140] M.D. Feit, J.A. Fleck, A. Steiger, *J. Comput. Phys.* 47 (1982) 412.
- [141] W.G. Hoover, *Computational Statistical Mechanics*, Elsevier, Amsterdam, 1991.
- [142] C.-A. Ullrich, Time-dependent density-functional approach to atoms in strong laser pulses, Ph.D. Thesis, J.-M. Universität Würzburg, 1995.
- [143] F. Calvayrac, Dynamique non-linéaire des électrons de valence dans les agrégats métalliques, Ph.D. Thesis, Université Paul Sabatier, Toulouse, 1997.
- [144] B. Montag, Ionische und elektronische Struktur der Cluster einfacher Metalle, Ph.D. Thesis, F.-A. Universität Erlangen-Nürnberg, 1995.
- [145] C. Kohl, Ph.D. Thesis, F.-A. Universität Erlangen-Nürnberg, 1997.
- [146] P.-G. Reinhard, E. Suraud, *Ann. Phys. (NY)* 239 (1995) 216.
- [147] G. Welke, R. Malfliet, C. Grégoire, M. Praksah, E. Suraud, *Phys. Rev. C* 40 (1989) 2611.
- [148] U. Näher, S. Björnholm, S. Frauendorf, F. Garcias, C. Guet, *Phys. Rep.* 285 (1997) 245.
- [149] U. Näher, H. Göhlich, T. Lange, T.P. Martin, *Phys. Rev. Lett.* 68 (1992) 3416.
- [150] C. Bréchignac, P. Cahuzac, F. Carlier, J. Leygnier, *Phys. Rev. Lett.* 63 (1989) 1368.
- [151] C. Bréchignac, P. Cahuzac, F. Carlier, M. de Frutos, *Phys. Rev. Lett.* 64 (1990) 2893.
- [152] C. Bréchignac, P. Cahuzac, F. Carlier, J. Leygnier, A. Sarfati, *Phys. Rev. B* 44 (1991) 11 386.
- [153] C. Bréchignac, P. Cahuzac, F. Carlier, M. de Frutos, *Phys. Rev. B* 49 (1994) 2825.
- [154] T. Lamy, G. Lamboley, D. Hitz, H.J. Andra, *Rev. Sci. Instr.* 61 (1990) 336.
- [155] M.L. Goldberger, K.M. Watson, *Collision Theory*, Wiley, New York, 1964.
- [156] P.-G. Reinhard, E. Suraud, C.A. Ullrich, *Euro. Phys. J. D* 1 (1998) 303.
- [157] J.H. Eisenberg, W. Greiner, *Excitation Mechanisms of the Nuclei*, Nuclear Theory, Vol. 2, North-Holland, Amsterdam, 1970.
- [158] M. Gavrilu (Ed.), *Atoms in Intense Laser Fields*, Academic, New York, 1992.
- [159] B. Piraux, A. L'Huillier, K. Rzazewski (Eds.), *Super-intense Laser-Atom Physics*, NATO ASI Ser. B, Vol. 316, Plenum, New York, 1993.
- [160] M. Protopaps, C.H. Keitel, P.I. Knight, *Rep. Prog. Phys.* 60 (1997) 389.
- [161] J.M. Eisenberg, W. Greiner, *Nuclear Theory*, Vol. 2, North-Holland, Amsterdam, 1970.
- [162] G.F. Bertsch, R.A. Broglia, *Oscillations in Finite Quantum Systems*, Cambridge University Press, Cambridge, 1994.
- [163] K. Yabana, G.F. Bertsch, *Int. J. Quant. Chem.* 75 (1999) 55.
- [164] C.A. Ullrich, P.-G. Reinhard, E. Suraud, *Phys. Rev. A* 57 (1998) 1938.
- [165] F. Calvayrac, A. Doms, P.-G. Reinhard, E. Suraud, *Euro. Phys. J. D* 4 (1998) 207.
- [166] D.G. Lappas, R. van Leeuwen, *J. Phys. B* 31 (1998) L249.
- [167] C.A. Ullrich, *J. Mol. Struct. THEOCHEM* (2000), Special Issue in honor of Rezso Gaspar, in press.
- [168] M. Horbatsch, *Z. Phys. D* 21 (1991) S63.
- [169] O. Cheshnovsky, K.J. Taylor, J. Conceicao, R.E. Smalley, *Phys. Rev. Lett.* 64 (1990) 1785.
- [170] R. Schlipper, Ph.D. Thesis, Universität Freiburg, 1999.
- [171] T. Voll et al., *Phys. Rev. Lett.* (2000), submitted for publication.
- [172] Z. Penzar, W. Ekardt, *Z. Phys. D* 17 (1990) 69.
- [173] T. Reiners, C. Ellert, M. Schmidt, H. Haberland, *Phys. Rev. Lett.* 74 (1997) 1558.
- [174] C. Kohl, S.M. El-Gammal, F. Calvayrac, E. Suraud, P.-G. Reinhard, *Euro. Phys. J. D* 5 (1999) 271.
- [175] L. Serra, R.A. Broglia, M. Barranco, J. Navarro, *Phys. Rev. A* 47 (1993) R1601.
- [176] C. Kohl, B. Montag, P.-G. Reinhard, *Z. Phys. D* 35 (1995) 57.
- [177] C. Kohl, B. Fischer, P.-G. Reinhard, *Phys. Rev. B* 56 (1997) 11 149.
- [178] A. Pinczuk, G. Abstreiter, in: M. Cardona, G. Güntherod (Ed.), *Light Scattering in Solids V*, Topics in Applied Physics, Vol. 66, Springer, Berlin, 1988.
- [179] L. Schweikhard, A. Herlert, S. Krückeberg, M. Vogel, C. Walther, *Phil. Mag. B* 79 (1999) 1343.
- [180] A. Herlert, S. Krückeberg, L. Schweikhard, M. Vogel, C. Walther, *Phys. Scr. T* 80 B (1999) 200.
- [181] D.L. Hill, J.A. Wheeler, *Phys. Rev.* 89 (1953) 1102.
- [182] C. Kohl, F. Calvayrac, P.-G. Reinhard, E. Suraud, *Surf. Sci.* 405 (1998) 74.
- [183] B. Montag, P.-G. Reinhard, *Phys. Rev. B* 51 (1995) 14 686.

- [184] G. F. Bertsch, D. Tomanek, *Phys. Rev. B* 40 (1989) 2749.
- [185] J.M. Pacheco, R.A. Broglia, B.R. Mottelson, *Z. Phys. D* 21 (1991) 289.
- [186] S.A. Blundell, C. Guet, *Z. Physik D* 33 (1995) 153.
- [187] K. Yabana, G.F. Bertsch, *Phys. Rev. A* 58 (1998) 2604.
- [188] K. Yabana, G.F. Bertsch, *Phys. Rev. A* 60 (1999) 3809.
- [189] C. Br  chignac, P. Cahuzac, J. Leygnier, A. Sarfati, *Phys. Rev. Lett.* 70 (1993) 2036.
- [190] F. Alasia, L. Serra, R.A. Broglia, N.V. Giai, E. Lipparini, H.E. Roman, *Phys. Rev. B* 52 (1995) 8488.
- [191] E.E. Koch, A. Otto, *Chem. Phys. Lett.* 12 (1972) 476.
- [192] G. Seifert, R. Schmidt, *New J. Chem.* 16 (1992) 1145.
- [193] R. Schmidt, G. Seifert, *Int. J. Mod. Phys. B* 6 (1992) 3845.
- [194] W. Kohn, *Phys. Rev. B* 123 (1961) 1242.
- [195] L. Brey, N.F. Johnson, B.I. Halperin, *Phys. Rev. B* 40 (1989) 647.
- [196] J. Babst, P.-G. Reinhard, *Z. Phys. D* 42 (1997) 209.
- [197] F. Catara, Ph. Chomaz, N. VanGiai, *Z. Physik D* 33 (1995) 219.
- [198] J. Treiner, H. Krivine, O. Bohigas, J. Martorell, *Nucl. Phys. A* 371 (1981) 253.
- [199] S. Kasperl, C. Kohl, P.-G. Reinhard, *Phys. Lett. A* 206 (1995) 81.
- [200] C. Yannouleas, J.M. Pacheco, R.A. Broglia, *Phys. Rev. B* 41 (1990) 41.
- [201] J. Borggreen, P. Chowdhury, N. Kebaili, L. Lundsberg-Nielsen, K. Luetzenkirchen, M.B. Nielsen, J. Pedersen, H.D. Rasmussen, *Phys. Rev. B* 48 (1993) 17 507.
- [202] T. Hirschmann, M. Brack, P.-G. Reinhard, *Z. Phys. D* 40 (1997) 254.
- [203] K. Yabana, T. Tazawa, Y. Abe, P. Bozek, *Phys. Rev. A* 57 (1998) R3165.
- [204] P.G. Reinhard, E. Suraud, *Phys. Rev. B* (2000), submitted for publication.
- [205] L. Phair, *Nucl. Phys. A* 548 (1992) 489.
- [206] C.A. Ullrich, P.-G. Reinhard, E. Suraud, *J. Phys. B* 30 (1997) 5043.
- [207] P.-G. Reinhard, E. Suraud, *Euro. Phys. J. D* 3 (1998) 175.
- [208] T.V. Shahbazyan, I.E. Perakis, J.Y. Bigot, *Phys. Rev. Lett.* 81 (1998) 3120.
- [209] M. Weissbluth, *Atoms and Molecules*, Academic Press, San Diego, 1978.
- [210] I. Vasiliev, S.   gut, J.R. Chelikowsky, *Phys. Rev. Lett.* 82 (1999) 1919.
- [211] A. Pohl, P.-G. Reinhard, E. Suraud, preprint 1999, *Phys. Rev. Lett.*, in press.
- [212] A. Assion, B. Lang, M. Simon, S. Voll, F. Traeger, G. Gerber, *Chem. Phys. Lett.* (1998), to appear.
- [213] M. Brack, F. Calvayrac, C. Kohl, S. K  mmel, P.-G. Reinhard, E. Suraud, C.A. Ullrich, *Euro. Phys. J. D* 9 (1999) 111.
- [214] C. Kohl, P.G. Reinhard, E. Suraud, *Euro. Phys. J. D* (2000), to appear.
- [215] E. Suraud, P.-G. Reinhard, *Phys. Rev. Lett.* (1999), submitted for publication.